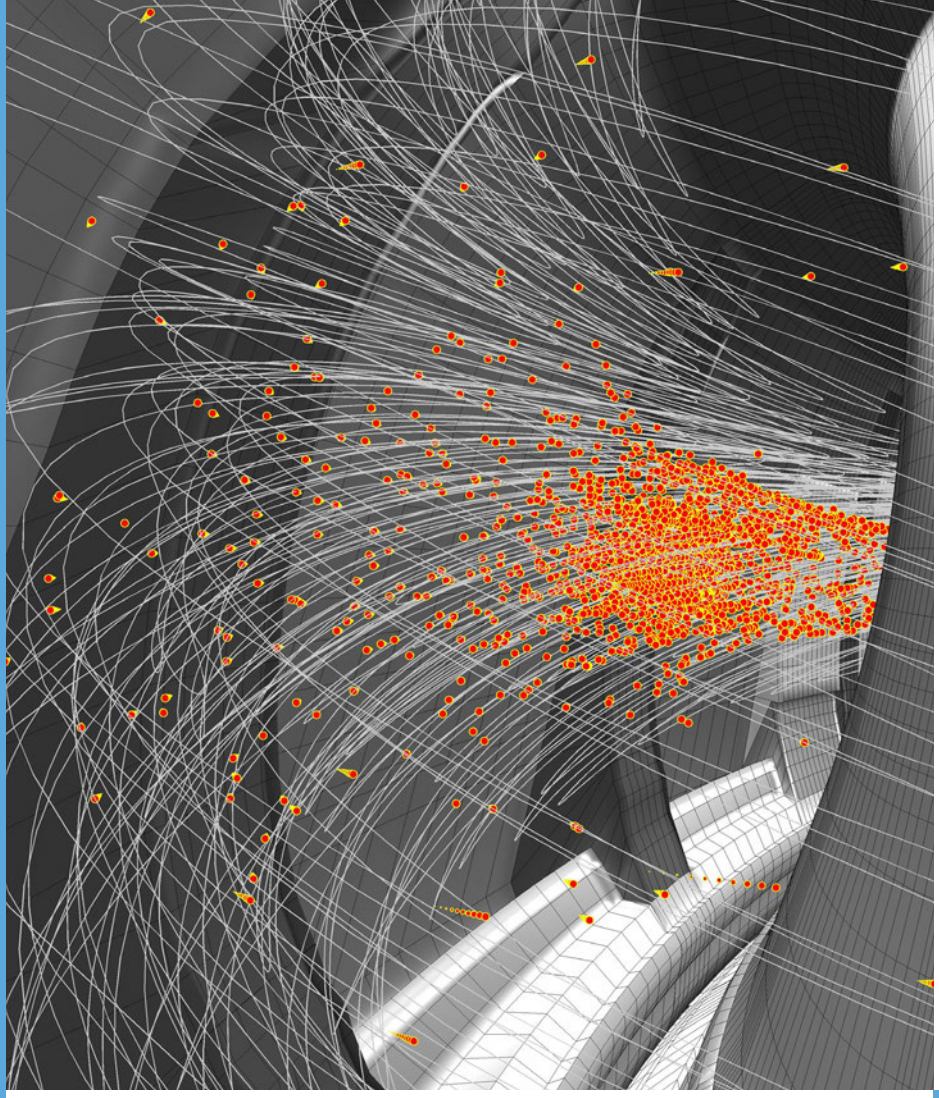

SCIENCE • TECHNOLOGY • RESEARCH HIGHLIGHTS • VISIONS •

Dissertation
10

Fast ions and momentum transport in JET tokamak plasmas

Antti Salmi

VTT SCIENCE 10

Fast ions and momentum transport in JET tokamak plasmas

Antti Salmi
VTT, Espoo

Thesis for the degree of Doctor of Science (Tech.) to be presented with due permission of the School of Science for public examination and criticism in Auditorium E, at the Aalto University School of Science (Espoo, Finland) on the 9th of November 2012 at 12 noon.

ISBN 978-951-38-7467-4 (soft back edition)
ISSN 2242-119X (soft back edition)

ISBN 978-951-38-7468-1 (http://www.vtt.fi/publications/index.jsp)
ISSN 2242-1203 (http://www.vtt.fi/publications/index.jsp)

JULKAISIJA - UTGIVARE - PUBLISHER

VTT
PL 1000 (Tekniikantie 4 A, Espoo)
02044 VTT
Puh. 020 722 111, faksi 020 722 7001

VTT
PB 1000 (Teknikvägen 4 A, Esbo)
FI-02044 VTT
Tfn. +358 20 722 111, telefax +358 20 722 7001

VTT Technical Research Centre of Finland
P.O. Box 1000 (Tekniikantie 4 A, Espoo)
FI-02044 VTT, Finland
Tel. +358 20 722 111, fax + 358 20 722 7001

Kopijyvä Oy, Kuopio 2012

Fast ions and momentum transport in JET tokamak plasmas

Antti Salmi. Espoo 2012. VTT Science 10. 71 p. + app. 75 p.

Abstract

Fast ions are an inseparable part of fusion plasmas. They can be generated using electromagnetic waves or injected into plasmas as neutrals to heat the bulk plasma and to drive toroidal rotation and current. In future power plants fusion born fast ions deliver the main heating into the plasma. Understanding and controlling the fast ions is of crucial importance for the operation of a power plant. Furthermore, fast ions provide ways to probe the properties of the thermal plasma and get insight of its confinement properties.

In this thesis, numerical code packages are used and developed to simulate JET experiments for a range of physics issues related to fast ions. Namely, the clamping fast ion distribution at high energies with RF heating, fast ion ripple torque generation and the toroidal momentum transport properties using NBI modulation technique are investigated.

Through a comparison of numerical simulations and the JET experimental data it is shown that the finite Larmor radius effects in ion cyclotron resonance heating are important and that they can prevent fast ion tail formation beyond certain energy. The identified mechanism could be used for tailoring the fast ion distribution in future experiments. Secondly, ASCOT simulations of NBI ions in a ripple field showed that most of the reduction of the toroidal rotation that has been observed in the JET enhanced ripple experiments could be attributed to fast ion ripple torque. Finally, fast ion torque calculations together with momentum transport analysis have led to the conclusion that momentum transport in not purely diffusive but that a convective component, which increases monotonically in radius, exists in a wide range of JET plasmas. Using parameter scans, the convective transport has been shown to be insensitive to collisionality and q-profile but to increase strongly against density gradient.

Keywords: JET, tokamak, fusion, energy, plasma, toroidal rotation, momentum transport, fast ions, neutral beam injection, NBI

Nopeat ionit ja liikemäärän kulkeutuminen JET-tokamakin plasmoissa

Antti Salmi. Espoo 2012. VTT Science 10. 71 s. + liitt. 75 s.

Tiivistelmä

Nopeat ionit ovat erottamaton osa fuusioplasmoja. Niitä voidaan tuottaa sähkömagneettisten aaltojen avulla tai suihkuttamalla ne plasmaan energisinä neutraaleina. Nopeita ioneja käytetään kuumentamaan ja pyörittämään plasmaa, virranajossa sekä plasman ominaisuuksien ja koossapidon tutkimiseen. Tulevaisuuden voimalaitoksissa fuusioreaktioissa syntyvät nopeat ionit toimivat plasman pääasiallisena lämmönlähteenä. Nopeiden ionien ilmiöiden ymmärtäminen ja niiden hallinta ovat tärkeitä fuusiovoimaloiden operoinnin kannalta.

Tässä väitöstyössä käytetään ja kehitetään numeerisia laskentaohjelmia selittämään nopeisiin ioneihin liittyviä koetuloksia Englannissa sijaitsevassa fuusiokoelaitoksessa (JET). Tutkimuksen kohteina ovat nopeiden ionien äkillinen väheneminen korkeilla energioilla radiotaajuuskuumennuksen yhteydessä, nopeiden ionien aiheuttama toroidaalinen vääntö magneettikentän ryppyisyyden vaikutuksesta ja liikemäärän kulkeutumisen ominaisuudet moduloituja neutraalisuihkuja käyttäen.

Työssä todennettiin simuloinneilla, että ionien äärellinen pyörimissäde selittää kokeellisesti havaitun nopeiden ionien pienen lukumäärän korkeilla energioilla käytettäessä radiotaajuuskuumennusta. JET:n magneettikentän rypytyskokeissa havaitut plasman pyörimisen muutokset voitiin hiukkassimulointien avulla päätellä johtuvan pääasiassa nopeiden ionien synnyttämän väännön takia. Lopulta analyysit liikemäärän kulkeutumisesta useissa erilaisissa plasmoissa osoittivat, että liikemäärän kulkeutuminen ei ole pelkästään diffuusia ja että merkittäväksi osoittautunut koossapitoa parantava ajautumisnopeus kasvaa plasman ulkoreunaa lähestyttäessä. Plasman tiheysgradientin kasvattamisen havaittiin nopeasti kasvattavan ajautumisnopeutta, kun taas törmäyksellisyyden tai q-profiilin muutosten vaikutukset olivat pieniä. Työn tuloksia voidaan hyödyntää ITERin ja tulevien laitosten suunnittelussa ja plasman pyörimisen ennustuksissa.

Keywords: JET, tokamak, fusion, energy, plasma, toroidal rotation, momentum transport, fast ions, neutral beam injection, NBI

Preface

The research summarized in this thesis has been carried out partially at the Aalto University, partially at the Joint European Torus (JET), Abingdon, UK and partially at the VTT Technical Research Centre of Finland. Several people have given important contributions to make this thesis possible and to whom I'm deeply grateful. First of all, I wish to thank Rainer Salomaa for granting me a PhD position in fusion and for his advise along the way. I'm also in debt to Seppo Karttunen for pulling the strings and for his encouragement when sending me for two long term secondments to JET.

Over the past years at the Aalto University, JET and VTT I've had the pleasure to work with many brilliant scientists from whom I've learned a great deal. My group leader at JET, Vassili Parail, always had new ideas for research and was continuously willing to help when I needed physics insights or got stuck on something. Mervi Mantsinen, Thomas Johnson and Tuomas Tala have all had important roles by sharing their vast knowledge on several areas of plasma physics and in teaching me the art of research.

The discussions during lunch and coffee breaks, and over pints, with Martin Laxåback, Marko Santala and Johnny Lönnroth have been an invaluable source of inspiration and deserve a special mention. I also thank Otto Asunta and Seppo Sipilä for their help with the ASCOT code.

Finally, the biggest thanks of all belongs to my parents and siblings, and to my family Anna, Eero and Emma for their love, support and understanding.

The financial support from Fortum Säätiö and Väisälän rahasto are gratefully acknowledged.

Espoo, October 17, 2012,

Antti Salmi

Academic dissertation

Supervisor	Professor Rainer Salomaa Department of Applied Physics Aalto University School of Science, Finland
Instructor	Dr Tuomas Tala Fusion and Plasma Technology VTT Technical Research Centre of Finland
Reviewers	Professor Torbjörn Hellsten Fusion Plasma Physics KTH Royal Institute of Technology, Sweden
	Dr Giovanni Tardini Institut für Plasmaphysik Max Planck Institut, Germany
Opponent	Dr Clarisse Bourdelle Institute of Magnetic Fusion Research CEA Cadarache, France

Contents

List of publications

This thesis consists of an overview and of the following publications which are referred to in the text by their Roman numerals.

I A. Salmi, M.J. Mantsinen, P. Beaumont, P.C. de Vries, L-G Eriksson, C. Gowers, P. Helander, M. Laxåback, J-M Noterdaeme, D. Testa and EFDA JET contributors. JET experiments to assess the clamping of the fast ion energy distribution during ICRF heating due to finite Larmor radius effects. *Plasma Physics and Controlled Fusion*, **48**, 717–726, 2006.

II A. Salmi, T. Johnson, V. Parail, J. Heikkinen, V. Hynönen, T.P. Kiviniemi, T. Kurki-Suonio and JET EFDA Contributors. ASCOT Modelling of Ripple Effects on Toroidal Torque. *Contributions to Plasma Physics*, **48**, 77–81, 2008.

III P.C. de Vries, A. Salmi, V. Parail, C. Giroud, Y. Andrew, T.M. Biewer, K.Crombé, I. Jenkins, T. Johnson, V. Kiptily, A. Loarte, J. Lönnroth, A. Meigs, N. Oyama, R. Sartori, G. Saibene, H. Urano, K.-D. Zastrow and JET EFDA Contributors. Effect of toroidal field ripple on plasma rotation in JET. *Nuclear Fusion*, **48**, 035007 (6pp), 2008.

IV P.C. de Vries, T.W. Versloot, A. Salmi, M-D Hua, D.H. Howell, C. Giroud, V. Parail, G. Saibene, T. Tala and JET EFDA Contributors. Momentum transport studies in JET H-mode discharges with an enhanced toroidal field ripple. *Plasma Physics and Controlled Fusion*, **52**, 065004 (11pp), 2010.

V A. Salmi, T. Tala, G. Corrigan, C. Giroud, J. Ferreira, J. Lönnroth, P. Mantica, V. Parail, M. Tsalas, T.W. Versloot, P.C. de Vries, K.-D. Zastrow and EFDA JET Contributors. NBI torque in the presence of magnetic field ripple: experiments and modelling for JET. *Plasma Physics and Controlled Fusion*, **53**, 085005 (20pp), 2011.

VI T. Tala, A. Salmi, C. Angioni, F.J. Casson, G. Corrigan, J. Ferreira, C. Giroud, P. Mantica, V. Naulin, A.G. Peeters, W. Solomon, D. Strintzi, M. Tsalas, T.W. Versloot, P.C. de Vries, K.-D. Zastrow and JET EFDA Contributors. Parametric dependences of momentum pinch and Prandtl number in JET. *Nuclear Fusion*, **51**, 123002 (11pp), 2011.

Author's contribution

Publication I: "JET experiments to assess the clamping of the fast ion energy distribution during ICRF heating due to finite Larmor radius effects"

The author used the combination of Fokker-Planck code PION and bounce averaged Monte Carlo code FIDO for calculating the fast hydrogen distribution during 2^{nd} harmonic ICRF heating. The agreement with experimental NPA measurements confirmed that FLR effects are important and responsible for the lack of multi-MeV ions during the 2^{nd} harmonic heating. The author wrote the full paper.

Publication II: "ASCOT Modelling of Ripple Effects on Toroidal Torque"

The author improved ASCOT code in order to record and calculate the total torque from the JET NBI system. The author made all the simulations which showed that ripple reduces the torque from JET NBI much more effectively than what it does for power losses. The author wrote the full paper.

Publication III: "Effect of toroidal field ripple on plasma rotation in JET"

The functionality developed in Publication II was utilised in this work to analyse a series of JET discharges with varying level of ripple. The author made all the NBI torque calculations and related data analysis and contributed to understanding the results. Figures 4 and 5 include ASCOT data and show the importance of the

fast ion ripple torque in explaining the observed toroidal rotation. The author also contributed in the parts of the text with ASCOT data and description.

Publication IV: "Momentum transport studies in JET H-mode discharges with an enhanced toroidal field ripple"

ASCOT calculations of NBI torque were used here to gain insight on the momentum transport properties of the JET plasmas. By taking into account the reduction in the NBI torque due to ripple it was possible to isolate the effect of transport and sources and deduce the average level diffusive and convective transport over a number of NBI heated JET discharges. The author contributed to this analysis by making NBI torque calculations (Figures 1 and 2) and in writing ASCOT related parts of the manuscript.

Publication V: "NBI torque in the presence of magnetic field ripple: experiments and modelling for JET"

The author extended ASCOT code functionality for time dependent operation and utilised it to obtain realistic time dependent NBI torque to analyse the experimental data. Furthermore, the author developed an optimisation framework around JETTO transport code to iteratively deduce the momentum transport properties of the discharges. These enabled the first experimental benchmark of calculated NBI torque in the presence of toroidal magnetic field ripple. The author wrote the full paper.

Publication VI: "Parametric dependences of momentum pinch and Prandtl number in JET"

In this work NBI is used as a tool to study the toroidal momentum transport properties of a number of plasmas to establish how it varies with q, collisionality and density gradient scale length. The author contributed through ASCOT torque analysis and transport analysis leveraging on techniques established in Publication V. These data are the basis for the results shown in sections 3 and 4.

1. Introduction

1.1 Fusion for energy

The ever increasing consumption of energy [1, 2] in the world together with environmental constraints demand the development of clean and sustainable forms of energy production. In the long term thermonuclear *fusion* could play a significant role in meeting these requirements. The fusion reaction providing the simplest route for fusion power production on Earth is between hydrogen isotopes deuterium and tritium

$$ {}^{2}_{1}\mathrm{D} + {}^{3}_{1}\mathrm{T} \rightarrow {}^{4}_{2}\mathrm{He}\ (3.52\ \mathrm{MeV}) + {}^{1}_{0}\mathrm{n}\ (14.1\ \mathrm{MeV}) \tag{1.1} $$

Deuterium can be extracted from water ($\sim$150 ppm) and tritium can be processed from lithium using neutrons from the fusion reactions within the fusion power plant itself

$$ {}^{6}_{3}\mathrm{Li} + {}^{1}_{0}\mathrm{n} \rightarrow {}^{4}_{2}\mathrm{He}\ (2.05\ \mathrm{MeV}) + {}^{3}_{1}\mathrm{T}\ (2.73\ \mathrm{MeV}) \tag{1.2} $$

The deuterium reserves last millions of years and the known lithium reserves for tens of thousands of years at the current level of consumption. The fuel for fusion is found all around the world making it geopolitically stable, fusion does not produce greenhouse gases or long lived radioactive waste and it has minimal impact on land use. Fusion power plants are ideally suited for large scale electricity production to provide a steady base load all year round.

In Europe the fusion research program is coordinated within the framework of the European Fusion Development Agreement (EFDA) which is funded by the European Commission. The current EFDA budget is roughly 100 million euros half

of which goes towards operating the largest tokamak to-date, the Joint European Torus (JET) in Abingdon, UK.

1.2 Tokamaks

Currently the most advanced concept for a fusion power plant in terms of fusion power is a *tokamak* which encloses the plasma inside a doughnut shaped chamber using strong toroidal magnetic field. The word *tokamak* is an acronym from the Russian words ***to****roidal'naya* ***kam****era s* ***ak****sial'nym magnitnym polem*, i.e. toroidal chamber with axial magnetic field. A simplified illustration of a tokamak, where the plasma is confined by a strong toroidal field in a doughnut shaped vessel with the plasma itself acting as the secondary winding, is shown in Fig. 1.1. The major benefit of this device the lack of ends in the tokamak 'bottle', made it significantly more efficient in confining the plasma while the primary transformer circuit allowed poloidal field generation and Ohmic heating via induction.

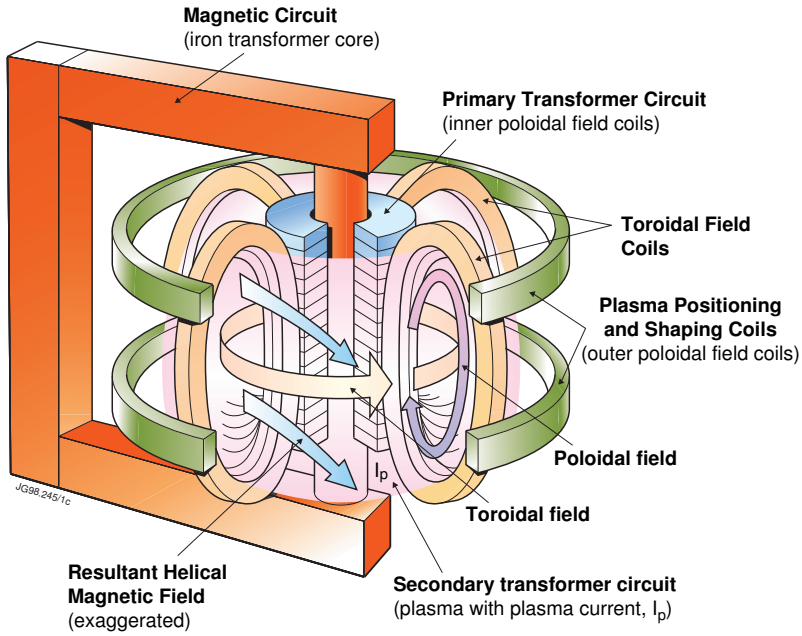

Figure 1.1. Tokamak principle. Ohmic heating and current drive is induced by the transformer where the plasma itself acts as the secondary winding. The iron core is optional when the primary winding is located along the toroidal axis inside the torus (central solenoid). *Courtesy of EFDA-JET.*

The tokamak was invented and first built during the cold war in the 1950s in Soviet Union [3]. It proved to be a superior concept outperforming the earlier devices (z-pinch, θ-pinch, etc.) in fusion power by orders of magnitude. Even though the first H-bombs were tested in 1952 in the USA and the cold war was still escalating between the super-powers, the magnetically confined fusion research was quickly declassified and researchers were encouraged to collaborate and find ways to harness the practically endless energy source for peaceful power production. The breakthrough raised hopes for a quick realisation of commercial power production. Indeed the following decades saw fusion power increase at a rate surpassing the famous Moore's Law in semiconductors.

As the tokamaks grew larger and more reactor relevant many new challenges were identified (instabilities, turbulence, materials) which together with increasing cost of building larger and larger devices and reduced funding due to the low cost of fossil fuels pushed the dream of commercial fusion power into the future. Presently the largest tokamak in the world, JET (Joint European Torus, see Fig. 1.2) in Oxfordshire, UK, has demonstrated 16 MW of peak fusion power and 4 MW in steady state conditions [4].

The next step experimental device being built in France, ITER [5–7], is a 15 billion euro international project involving over half of the world population (EU, US, Japan, Russia, China, India and Korea) and it is designed to be able to produce 500 MW of fusion power whilst using only 50 MW of external power to heat the plasma. If, and hopefully when, ITER proves to be a success the next step could be to build a demonstration power plant, DEMO, which would integrate all the technologies tested in ITER and those from the parallel materials research program into one plant for testing the power production. With successful integration of technologies and advances in fusion relevant materials, the era of fusion power could well begin on the second half of this century.

1.3 Heating and stabilising the plasma

In order to bring the plasma temperature up to the required 150 million degrees (10–20 keV) powerful plasma heating methods are needed. The Ohmic heating alone, generated by the induction, is not sufficient. It cannot heat up fusion plasmas beyond 4 keV due to the reduced resistivity of the plasma at high tempera-

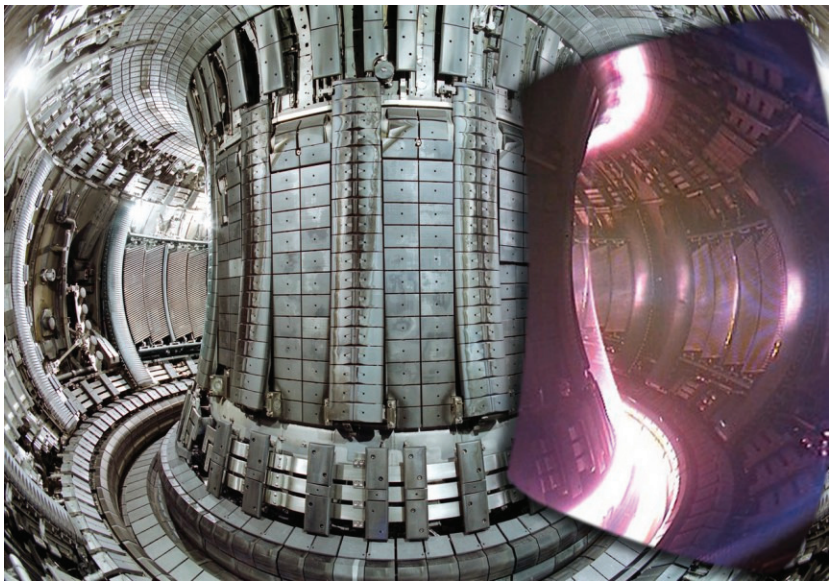

Figure 1.2. Wide angle view from inside the JET tokamak. On right, plasma discharge is overlaid. The white light during the plasma discharge indicates the high heat flux regions, the electromagnetic emissions from the central plasma are largely outside the visible spectrum. *Courtesy of EFDA-JET.*

tures, i.e. $\nu \propto T_e^{-3/2}$. Furthermore, Ohmic heating is intrinsically pulsed in nature which is not attractive from engineering point of view. In power plants the Ohmic heating would mainly be used for the start-up phase after which non-inductive means of heating and current drive would be used to control and stabilise the burning plasma.

Due to the strong magnetic field used in tokamaks external energy can only be injected into the system either as energetic neutral particles (neutral beam injection, NBI) or by launching electromagnetic waves whose the energy is transferred to the plasma typically via a resonance interaction. Depending on the frequency and wavelength power can be absorbed either on ions (Ion Cyclotron Resonance Frequency, $\sim$50 MHz) or on electrons (Electron Cyclotron Resonance Frequency, $\sim$100 GHz) or used to drive current (Lower Hybrid Current Drive, $\sim$4 GHz).

1.4 Toroidal coordinates

A convenient coordinate system for treating tokamak plasmas is illustrated in Fig. 1.3. The toroidal angle ϕ increases counter-clockwise when viewed from

above, z points upward and R outwards forming a right handed (R, ϕ, z) system. Flux coordinates (r, θ) describe the nested flux surfaces.

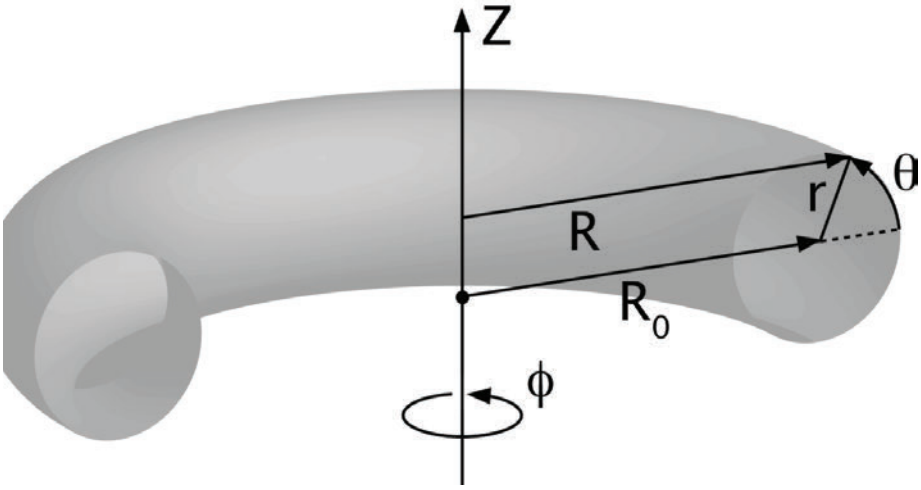

Figure 1.3. Simple toroidal coordinate system with circular flux surfaces.[1]

In most tokamaks flux surfaces are not circular and concentric as in this simplified picture but are elongated and radially shifted as given by the Grad-Shafranov equation [8] (see also Fig. 2.3). In these cases the geometrical coordinate r is not a convenient label any more and ρ_{tor} and ρ_{pol} are often used and appear in many of the figures plotted in this thesis and in Publications I–IV. Here ρ_{tor} is the normalised square root of the toroidal flux ψ_{tor} enclosed by the flux surface and ρ_{pol} is the correspondingly normalised label for the poloidal flux ψ_{pol} [8]. An important property of a flux surface is that by following a magnetic field line that starts from a certain flux surface always stays on that same surface. Since charged particles are tied to the field lines by Lorentz force (Sec. 2.1) they are also tied to the same flux surface and therefore, to a good approximation, plasma temperature and density are constant on a given flux surface. Ions and electrons can move freely along the field lines but only slowly across. This means that plasma confinement properties including heat and toroidal momentum transport can often be studied in radial direction only.

[1] http://www-fusion.ciemat.es/fusionwiki/index.php/Toroidal_coordinates

1.5 Outline of this thesis

This thesis in an introduction to and gives an overview of the main results obtained in the Publications I–VI. In Chapter 2 several relevant aspects of fast ion physics are briefly reviewed. First, motion of fast ions and their generation through ICRH (Publication I) and NBI (Publications II–VI) in the tokamak plasmas are described. Then the toroidal field ripple and its effect on fast ions is briefly reviewed together with a description of fast ion torque transfer to the background plasma. The last part of Chapter 2 gives an introduction to the toroidal momentum transport and NBI modulation technique which are used and studied in Publications V–VI. In Chapter 3 the simulation tools and methods are discussed together with a description of related modifications to them. Chapter 4 gives a short overview of the results obtained in Publications I–VI highlighting the most important findings. Finally the thesis is summarised.

2. Fast ion physics and transport

The definition of *fast* ion naturally depends on the context. In fusion plasmas fast ions are usually considered to be those whose kinetic energy exceeds the thermal energy of the bulk plasma by roughly a factor of 10. In today's medium to large sized tokamak devices the plasma temperature is typically in the range of 1-10 keV ($\sim$15 keV in future power plants) and therefore the lower energy limit for fast ions is somewhere around 10-100 keV, depending on a tokamak and a scenario. While in principle there is no upper limit for the fast ion energy in practice the size of the plasma and the strength of the magnetic field set constraints on the achievable fast ion energy. Namely, at high energies the orbits of the ions become so large that they are no longer confined in the plasma but collide with the torus walls. In JET, ions with energies up to 10 MeV have been observed. However, even the most energetic ions in fusion plasmas are far from the relativistic limit and their behaviour can be understood with classical treatment.

There are numerous reasons why fast ions are of interest to fusion plasmas. One of the most important one is their ability to transfer heat and momentum to the plasma. Fast ions interact with the ions and electrons of the main plasma via Coulomb collisions through which they transfer their energy and kinetic momentum. Toroidally asymmetric fast ion velocity distribution can drive current and induce toroidal plasma rotation. Fast ions can stabilise or destabilise some internal plasma instabilities such as sawteeth and enhance the fusion yield. On the other hand, fast ions can also have detrimental effects both on the plasma and the device. Namely, since the fast ions have large orbits and even a relatively small number of them can carry a significant fraction of the total plasma stored energy, their loss can damage the first wall, reduce the heating efficiency and modify the plasma rotation [9–12]. The free energy in the fast ions can in some

circumstances create instabilities (e.g. alfven eigenmodes) that reduce the plasma confinement. Understanding the creation and behaviour of the fast ion population in fusion plasmas is necessary to maximise their benefits and minimise their adverse effects.

2.1 Motion of charged particles

Compared to thermal ions, fast ion orbits are much wider and their distributions are often asymmetric and non-Maxwellian which means that their treatment is not usually realistic with fluid approach as often used for thermal plasma but that kinetic simulations are needed.

The motion of charged particles in an electromagnetic field is controlled by the Lorentz force

$$m\frac{d\mathbf{v}}{dt} = q(\mathbf{E} + \mathbf{v} \times \mathbf{B}) \tag{2.1}$$

Here, $\mathbf{E}$ and $\mathbf{B}$ are the electric and magnetic field vectors whereas m, q and $\mathbf{v}$ are the particle mass, charge and velocity, respectively. In absence of other interactions (e.g. collisions) particles can only gain energy through electric field which is parallel to the particle velocity (this is easily confirmed after taking the dot product of Eq. (2.1) with $\mathbf{v}$).

Due to the strong magnetic field used in tokamaks the gyro radius (or Larmor radius) $\rho = v_\perp/\omega_{ci}$ of a particle, where $v_\perp$ is the velocity perpendicular to the magnetic field and $\Omega_{ci} = qB/m$ is the gyro (or cyclotron) frequency, is often small compared to the typical scale lengths in the plasma. Furthermore, the time scales of interest are often much longer than the gyration period. In this case it is useful to average out the gyration and follow the guiding centre motion of the particle rather than its actual position. The averaging results in an equation for guiding centre motion [13]

$$\mathbf{v}_g = v_\parallel \hat{\mathbf{e}}_\parallel + \frac{\mathbf{F} \times \mathbf{B}}{qB^2} \tag{2.2}$$

$$\dot{v}_g = F_\parallel/m. \tag{2.3}$$

Here $\mathbf{F}$ is any force acting on the guiding centre such as electric field or non-uniformities in magnetic field. Figure 2.1 illustrates a typical orbit for an energetic, poloidally trapped, ion in a tokamak magnetic field. Just by glancing at

the trajectory it is easy to be convinced that in a realistic geometry where the magnetic field itself cannot be represented by simple equation the guiding centre equations are not analytically integrable and numerical codes are needed to trace the particles.

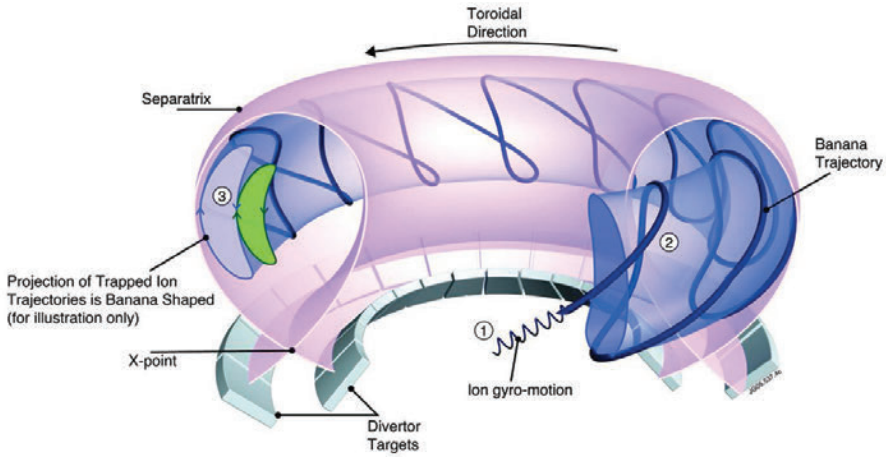

Figure 2.1. Trajectory of an energetic trapped ion in a tokamak equilibrium. (1) the gyration of the ion around the field line is shown with a thin line. (2) The thick line shows the guiding centre (gyro-averaged) motion of the ion. At (3) the poloidal cross section of the 3D trajectory is depicted. The smaller "banana" next to (3) illustrates the orbit of another ion that was launched, from the location where the two bananas are joined, in the opposite direction to the ion forming the larger banana. *Courtesy of EFDA-JET*

2.1.1 Constants of motion and adiabatic invariants

With stationary or slowly varying electromagnetic fields with toroidal symmetry charged particles have three invariants. Without collisions or other interactions they remain practically constant along the particle trajectory. These invariants can be chosen as the total energy E_{tot}, magnetic moment μ and the canonical toroidal angular momentum p_ϕ

$$E_{tot} = mv^2/2 + Ze\Phi \tag{2.4}$$

$$\mu = mv_\perp^2/2B \tag{2.5}$$

$$p_\phi = Ze\psi - mRv_\phi \tag{2.6}$$

where $\psi = \int_0^r RB_\theta dr'$ is the poloidal flux, Φ is the electrostatic potential, $v_\perp$ is the velocity perpendicular to the magnetic field, v_ϕ is the toroidal velocity, Z is the charge number and e is the elementary charge. Without toroidal symmetry the canonical toroidal angular momentum p_ϕ is no longer conserved. In non-axisymmetric magnetic field the radial transport of the charged particles is enhanced reducing the confinement and acts as a source for counter current torque (see Secs. 2.3 and 2.4).

2.2 Generation of fast ions

There are several ways to generate fast ions. Firstly, they are produced within the plasma in a number of different fusion reactions the most significant of which is the D-T fusion yielding a neutron and a 3.5 MeV alpha particle. In ITER, alphas will provide most of the plasma heating and are by far the most important fast ion species in the plasma. Of the current tokamaks only JET can operate D-T plasmas, and when it does it is a special event (tritium is expensive and difficult to handle due to its activity). Most of the time either deuterium or hydrogen plasmas are used and the fusion yields are too small to be of significance, apart from diagnostics purposes [14–16]. Therefore, the main source of fast ions in current devices comes either from neutral beam injection or through ion cyclotron resonance heating. In burning plasmas where alphas dominate the NBI and/or ICRH generated ions will still have an important role in driving current and rotation and in controlling the plasma

2.2.1 Neutral beam injection

Neutral beam injection (NBI) is a widely used method to non-inductively heat and drive current and rotation in the tokamak plasmas. NBI is a robust heating scheme which in current experiments can be used for nearly all plasmas without coupling issues or upper density limits. NBI also provides the most efficient way for inducing plasma rotation in current tokamaks. This is an important property of NBI since the plasma rotation and the rotation shear are known, experimentally and in theory, to improve plasma performance by clamping down the turbulence and the associated radial transport of heat, particles and momentum [17–19]. The reduced level of turbulence allows higher plasma temperature and

density thus improving the fusion yield and therefore potentially reducing the cost of the energy. Toroidal rotation is also known to stabilize magneto-hydodynamic (MHD) instabilities such as resistive wall modes (RWM) [20]. NBI generated torque and its usage to study rotation and momentum transport are discussed in more detail in Chapter 4.

The NBI system at JET [21] can deliver more than 20 MW of heating power and more than 20 Nm of torque routinely into the plasma. It consists of two beam boxes located toroidally 180 degrees apart, one in octant 4 and one in octant 8 (see Fig. 2.2). Both beam boxes consist of 8 positive ion neutral injectors (PINIs) of which 4 are in the so called tangential orientation and 4 in perpendicular orientation with respect to the toroidal magnetic field. In normal JET operation the plasma current is in the clockwise direction as indicated in the figure and the torque provided by the NBI is in co-current direction.

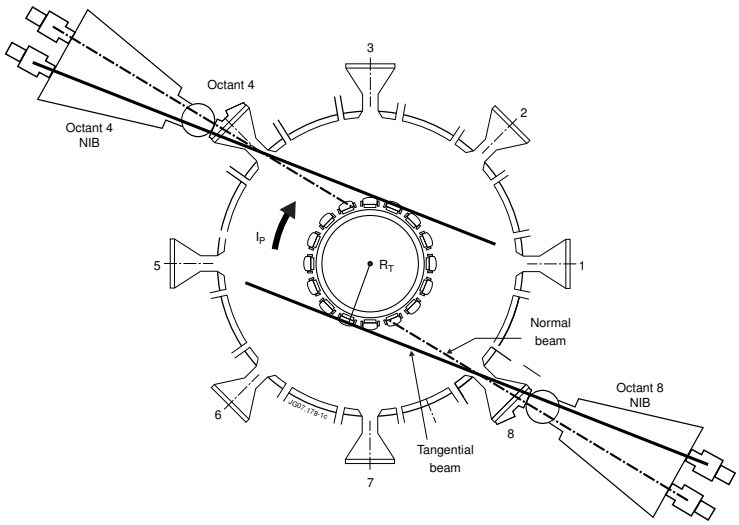

Figure 2.2. JET NBI system view from above (from Publication V).

The geometrical properties of the NBI system are fixed and the alignment cannot be changed during operation. Therefore the beams always point in the same direction in each experimental campaign. Figure 2.3 shows the poloidal alignment of each PINI in octant 8 NBI (octant 4 alignment is nearly identical). Reasonable flexibility to control the NBI heating and torque input is still retained as the PINI mixture, acceleration voltage of the PINIs and the power waveforms can be adjusted. The neutral beam modulation capability is in fact utilised in Publications

V-VI to validate the beam torque calculation and to study the momentum transport properties of the plasmas.

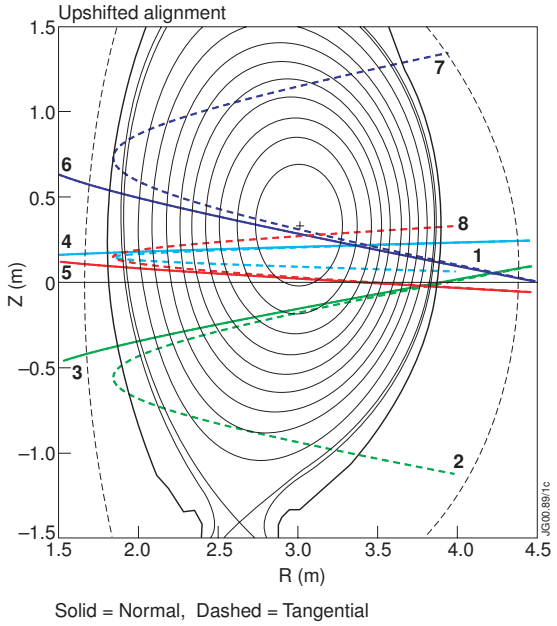

Figure 2.3. Poloidal view JET NBI alignment in the upshifted configuration. All beams enter the plasma near the midplane. The curvature of the trajectories results from 3D to 2D mapping. *Courtesy of EFDA-JET.*

The power from the neutral beams is absorbed in the plasma through Coulomb collisions. The heating rate (or the rate at which the beam loses energy) is given by

$$\frac{dE}{dt} = -(\nu_e + \sum_i \nu_i)E \tag{2.7}$$

where the summation loops over all ion species i in the plasma, E is the energy of the beam ion and ν_i, ν_e are the beam ion collision frequencies against the plasma ions and electrons, respectively. Substituting the collision frequencies this can be written as [13]

$$\frac{dE}{dt} = -\frac{Z^2 e^4 \ln\Lambda n_e}{4\pi\epsilon_0 m_e}\left[\frac{m_e}{n_e E^{3/2}}\sum_i \frac{n_i Z_i^2}{m_i} + \frac{4}{3\sqrt{\pi}}\left(\frac{m_e}{m k_B T_e}\right)^{3/2}\right]E \tag{2.8}$$

where in the usual circumstances the first term on the right hand side describes the heat deposition on the bulk ions and the second term the heat deposition on electrons. Here $\ln\Lambda \approx 17$ is the Coulomb logarithm, ϵ_0 is the permittivity of free

space, k_B is the Boltzmann constant, e is the elementary charge and m, Z, v are the mass, charge number and velocity respectively. Variables without subscripts refer to the beam ions. The collision frequency of the beam ions against electrons is independent of the beam ion energy ($\nu_e \sim n_e T_e^{-3/2}$) whereas against ions it becomes higher at low energy ($\nu_i \sim E^{-3/2}$). Therefore, at high energies the energetic ions interact mainly with electrons and at low with ions. The critical energy at which the ion and electron heating rates are equal is

$$E_{cr} = 14.8 k_B T_e A \left(\frac{1}{n_e} \sum_i \frac{n_i Z_i^2}{A_i} \right)^{2/3} \tag{2.9}$$

where A is the beam ion mass number and the summation loops over the background species. The quantity within the brackets varies slowly leaving the electron temperature and the beam ion mass as the only significant parameters that determine whether bulk ions or electrons are heated. In JET plasmas the critical energy is relatively high compared to the beam injection energy and the NBI is dominantly heating the ions. In ITER, however, beam injection energy of approximately 1 MeV is needed for deep enough penetration and therefore the NBI there will mainly heat the electrons.

2.2.2 Ion Cyclotron Resonance Heating

Ion Cyclotron Resonance Heating (ICRH) is the only heating method available for ITER that can dominantly heat ions [22]. The other common means of electromagnetically transmitting energy into the plasma, lower hybrid (LH) and electron cyclotron (EC) waves, are directly absorbed by the electrons. Furthermore, the collisional power transfer from both the alphas and the NBI ions result in dominant electron heating due to their high incident energy [23]. ICRH, however, can be optimised for ion heating by making sure that the average energy of the resonant ion population remains at reasonably low level. In ITER, the minority ^{3}He heating scheme is aimed for this and is expected to have an important role in setting the plasma conditions favourable for fusion reactions.

With ICRH scheme, radio frequency (RF) waves are launched with an antenna into the plasma where the power is absorbed by the resonating ions through wave-particle interaction (see Figs. 2.4 and 2.5).

Fusion plasmas can support a large number of electromagnetic waves with var-

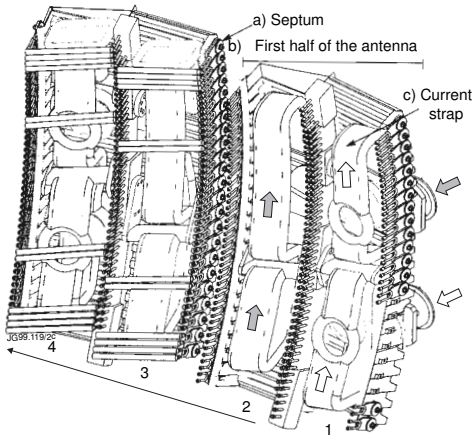

Figure 2.4. One of the four JET A2 antennas showing the first half of the antenna completely without the Faraday screens leaving the current straps visible. Thick arrows indicate that the AC current can be phased independently between the straps. Three A2 antennas, covered with Faraday screens, can be seen in Fig. 1.2. *Courtesy of EFDA-JET.*

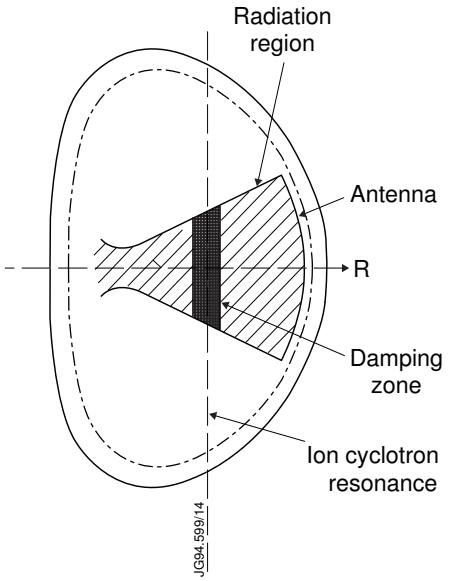

Figure 2.5. Schematic view of ICRF heating, wave propagation and damping in tokamak plasma. *Courtesy of EFDA-JET.*

ious frequencies and wave lengths. In ion cyclotron range of frequencies (20–80 MHz in fusion plasmas) the important branch in the plasma dispersion relation is the *fast wave* (or compressional hydromagnetic mode) [8, 24]. Fast wave does not exist in vacuum making it necessary to place the ICRH antenna relatively close to the plasma to avoid power being reflected back to the antenna. With close proximity to hot plasma, high heat fluxes must be tolerated and therefore the antennas are protected with heat bearing limiters.

Once the power reaches the plasma it can be absorbed. Provided that the frequency of the wave and the heating scheme are suitably selected most of the power will be absorbed by ions whose gyro-frequency or its harmonic equals the Doppler shifted wave frequency ($\nu = 0$)

$$\nu \equiv \omega - n\Omega_c - v_{\|}k_{\|} \tag{2.10}$$

where n is an integer, Ω_c is the gyro (or cyclotron) frequency of the ions, $v_{\|}$ is the ion velocity along the magnetic field line and $k_{\|}$ is the parallel wave number of the wave. In tokamaks the magnetic field is roughly proportional to 1/R which means that the gyro-frequency varies along the particle trajectories and that ions are resonant only for a short period when they cross the nearly vertical resonance layer. At the resonance position the ions see a constant electric field which can either accelerate or decelerate the ions depending on the relative phase between the wave and their gyration. When the relative phase between the successive RF interactions is random the quasi-linear theory states that this process is equal to diffusion in velocity space. In fusion relevant conditions the net effect is energy transfer from the waves to the particles.

Quasi-linear theory

According to quasi-linear theory [24, 25] the RF operator $Q(f)$ for a single wave can be written as a diffusion operator

$$Q(f) = \frac{1}{\partial v_{\perp}} \left(v_{\perp} D_{RF} \frac{\partial f}{\partial v_{\perp}} \right) \tag{2.11}$$

where the RF diffusion coefficient is proportional to

$$D_{RF} \sim \left| \tau_{RF} Ze(E_{+} J_{n-1}\left(k_{\perp}\rho\right) + E_{-} J_{n+1}(k_{\perp}\rho)) \right|^2 \tag{2.12}$$

where $E_{\pm}$ are the amplitudes of the left and right-hand polarized electric field components, $k_{\perp}$ is the local perpendicular wave number, J_m are the Bessel functions of the first kind and $\tau_{RF} = \int \exp(i \int \nu(t')dt')dt$ is the RF interaction time and n in an integer to indicate the resonance harmonic.

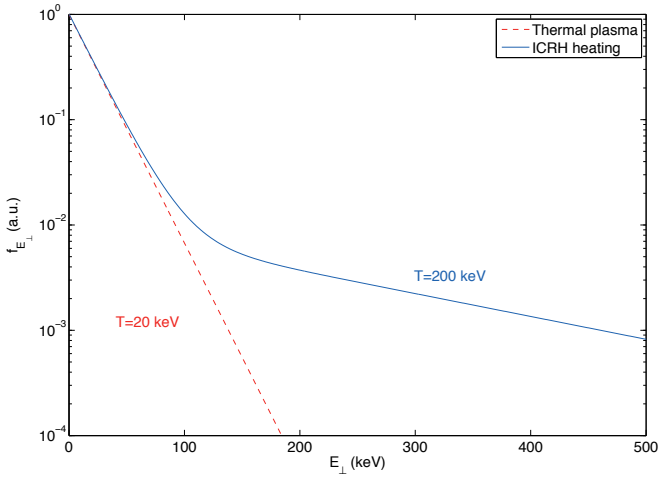

Figure 2.6. Schematic illustration of fast ion tail with strongly applied ICRF heating.

ICRH increases the perpendicular velocity of the resonating ions pulling a tail in the energy distribution as illustrated in the Fig. 2.6. The length of the tail and the effective temperature depend on the absorbed power per particle, fast ion collisionality (slowing down process) as well as other effects such as losses and instabilities [26]. The shape of the tail is usually more complex than in the idealised picture shown here. Realistic calculations of the fast ion distribution functions require the use of sophisticated codes such as PION and FIDO (see Chapter 3). In Publication I these tools are used to analyse JET experiments at the second harmonic ($n = 2$) ICRF heating that show the clamping of fast ion tail around the energy E^* where the first minimum of D_{RF} is located.

It is worth pointing out that while NBI is the most efficient method for driving toroidal rotation in current experiments also ICRH can modify the rotation profile somewhat either through momentum injection, fast ion losses or through transport modification [27–29]. A particular scheme where large rotation changes have been observed on Alcator-Cmod and JET involves mode conversion but is not yet fully understood [30, 31].

2.3 Toroidal field ripple

Toroidal magnetic field ripple (TF ripple) is the non-axisymmetric part of the magnetic field which arises due to the finite number of toroidal field coils. The ripple magnitude δ is defined as

$$\delta(R,z) = \frac{B_{\max}(R,z) - B_{\min}(R,z)}{B_{\max}(R,z) + B_{\min}(R,z)}, \tag{2.13}$$

i.e. it is the relative amplitude by which the magnetic field ripples (oscillates) when moving in toroidal direction (see Fig. 2.7).

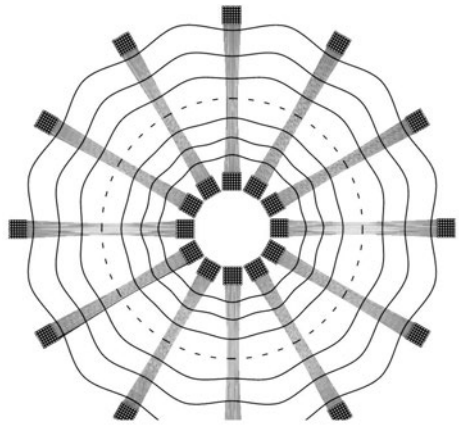

Figure 2.7. Toroidal field coils viewed from above. The toroidal field ripple arises due to the finite number of toroidal field coils. *Courtesy of EFDA-JET.*

TF ripple is an intrinsic property of all physical tokamaks. The magnitude of the ripple depends on the geometry and on the number of the coils and it is unique for each tokamak. Large levels of ripple have adverse effects on plasma confinement, especially on fast particle confinement [32, 33] and must be avoided. The ripple magnitude can be reduced by increasing the number of the coils and by making the coils larger. The downside of going this way is that the coils, especially if they are super-conducting, are typically the most expensive part of the device which together with the access requirements for maintenance, for diagnostics line-of-sights and for auxiliary heating systems means that some non-negligible level of ripple must always be tolerated.

Figure 2.8 shows the total magnetic field strength along a field line traced for one poloidal turn at $\rho_{pol} = 0.95$ for a JET discharge #77090. The large scale variation in the magnetic field is due to the $1/R$ dependence of the vacuum toroidal

field. The full line shows the total field with the exaggerated ripple included. The poloidal angle increases counter-clockwise and is zero at the outboard mid-plane. One can observe that ripple magnitude is largest at the LFS where it forms toroidally localised wells. In this region ripple effect is strongest and particles can get toroidally trapped due to the mirror force $F = -\mu\nabla_{\|}B$ [32].

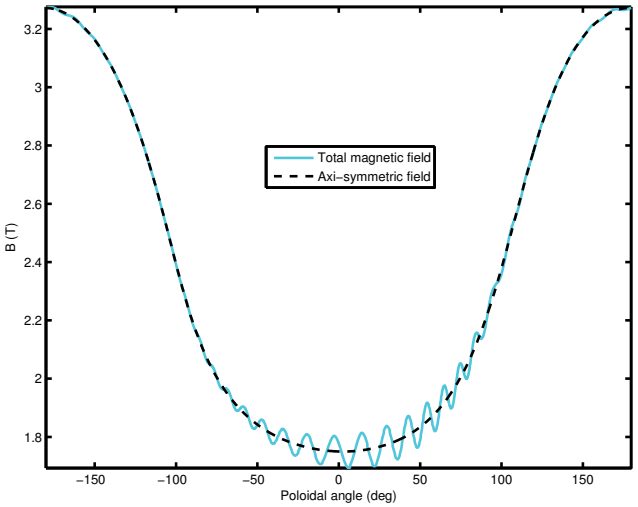

Figure 2.8. Total magnetic field strength for a JET discharge #77090 following a field line near separatrix for one poloidal turn. Dashed line shows the axi-symmetric contribution dominated by the 1/R dependence of the toroidal magnetic field and the full line shows the total strength including the ripple contribution (exaggerated).

In JET 32 toroidal field coils are used in normal operation. Uniquely among the current tokamak devices, JET can switch off every second coil or feed the even and odd numbered coils independently with different currents to adjust the level of ripple during experiments. Figure 2.9 depicts the numerical maps of the ripple magnitude δ for JET nominal operation with 32 coils and for the maximum possible ripple with every second coil turned off.

The shaded areas in the plasma show regions where ripple wells exist, i.e. regions where the gradient of the magnetic field strength along the magnetic field line changes sign due to the ripple (compare with Fig. 2.8). The existence of ripple wells depends also on the equilibrium magnetic field and is thus specific to each discharge. The boundary between ripple well region and region where ripple wells do not exist can be approximately described by the formula [34]

$$\alpha = \left| \frac{B_R}{BN\delta} \right| = 1 \tag{2.14}$$

where B_R is the major radius component of the equilibrium field and N is the number of toroidal field coils. Ripple wells exist for values $\alpha < 1$. The reason why ripple wells are of importance is because ions with small pitch $\xi = v_\parallel / v$ can be trapped toroidally. This can lead to rapid loss of ions due to the uncompensated vertical drift unless they de-trap either due to some interaction such as a collision or they pass through a region where ripple wells do not exist in which case they de-trap and remain in the plasma. For the JET plasmas studied here the ripple trapping for the NBI ions becomes important only at large ripple values $\delta > 1.5\%$.

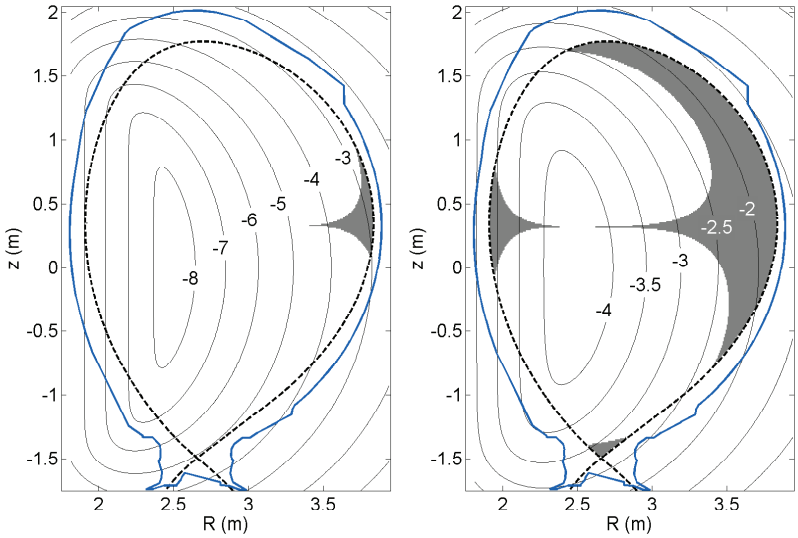

Figure 2.9. Toroidal magnetic field ripple δ plotted using $\log_{10}$ contours for a) the 32 coil operation and b) the 16 coil operation. Shaded areas show the regions where ripple wells exist (for plasmas similar to #77090).

Ripple magnitude varies strongly across the poloidal plane being largest on the outboard side close to the separatrix. Ripple decays exponentially in radius and becomes very small towards the core of the plasma. The decay length (away from the coils) for the 16 coil ripple magnitude is roughly 25 cm whereas it is half of that for the 32 coil case. When ripple magnitude is quoted it is customary to use a value which is either the maximum within the plasma or with respect to a fixed R-z coordinate. In the following the JET ripple magnitude is given at a location $R = 3.84$ m and $Z = 0$ m unless otherwise stated.

In general, the modelling capability of NBI sources for axi-symmetric plasmas

is considered to be good when neo-classical processes are dominating. However, prior to the work in this thesis the NBI torque sources in presence of toroidal field (TF) ripple were not well known despite the importance of ripple for ITER. In fact, the ASCOT calculations reported in Publication II are the first realistic fast ion ripple torque calculations in any tokamak.

2.3.1 Fast ions and ripple

Toroidal field ripple perturbs particle motion by giving rise to small oscillations in its velocity components and radial position

$$\tilde{v}_{\parallel} = -(v_{\perp}^2/2v_{\parallel})\delta \cos N\phi. \tag{2.15}$$

These oscillations are, however, self-cancelling along most of its trajectory. Significant contribution is only accumulated near the turning points of trapped particles where the oscillations are amplified ($v_{\parallel} \to 0$) and are not necessarily cancelled. For a simplified geometry the contribution around the turning point location can be integrated analytically using stationary phase method to yield a radial step size [35]

$$\Delta r = (N\pi/\theta_t)^{1/2}(q/\epsilon)^{3/2}\rho\delta \cos N\phi_t \tag{2.16}$$

where θ_t and ϕ_t are the poloidal and toroidal angles of the turning point location, q is the safety factor, ρ is the gyro radius and ϵ is the aspect ratio. It can be seen that the radial step size increases with particle energy $\Delta r \sim E^{1/2}$. Furthermore, since the diffusion coefficient scales like $D \sim (\Delta r)^2/\tau$ and the appropriate time scale (bounce time) is proportional to $\tau \sim E^{-1/2}$ the radial diffusion due to ripple depends strongly on energy $D \sim E^{3/2}$. Although very useful for physics insight the Eq. (2.16) is not accurate enough for quantitative calculations of fast ion ripple torque in an experiment. In this work ASCOT code is used to take into account ripple effects in realistic experimental geometry and in the presence of Coulomb collisions. All the intricacies of the ripple effect and the processes of trapping and de-trapping are trivially included in the guiding centre Monte Carlo approach where the ions are traced in the non-axisymmetric 3D magnetic field.

Theory has been developed for estimating the torque that results from the non-axisymmetric magnetic perturbations such as toroidal magnetic field ripple [36–40]. It has been applied to explain some experiments using resonant magnetic

perturbations (RMP) [41] but nevertheless it is rather sensitive to the collisionality regime and until so far it has not been shown to yield strong torques in the JET ripple field. Nevertheless, both in Tore Supra and in JET small negative rotation has been observed in Ohmic plasmas in the presence of large ripple [28, 42]. From the small counter current rotation in these discharges one can estimate that the magnitude of the Neoclassical Toroidal Viscosity (NTV) torque caused by the ripple should be quite modest. In this work the experimental observations and the modelling are indeed consistent with the assumption that NTV torque is small compared to the applied NBI torque. Finally, the supra-thermal electron losses ($\sim$200 keV) observed under strong LH heating in Tore Supra [43] are not expected to play a role in the typical JET plasmas with enhanced ripple where supra-thermal electrons are not present and therefore electron contribution to the torque is neglected.

2.4 Fast ion torque

Fast ions can transfer their toroidal momentum into the bulk plasma in two ways. First, simply via Coulomb collisions where part of fast ion toroidal kinetic momentum is absorbed by the bulk plasma $m\Delta v_\phi R$. The second mechanism ($j \times B$ – torque) for momentum transfer is somewhat less intuitive but in many cases of equal importance. It is associated with the radial current of fast ions [44] (see illustration in Fig. 2.10). Fast ion losses, fast ion ripple diffusion and injection of ions into trapped orbits are examples of processes which generate non-ambipolar fast ion currents. Due to the quasi-neutrality condition the plasma sets up a complex process to generate a *return* current that is equal but opposite to the fast ion current to cancel any charge accumulation. The torque on the plasma thus becomes

$$\tau_{j\times B} = j_{\mathrm{ret}} B_\theta R \tag{2.17}$$

where j_{ret} is the return current of the bulk plasma ($j_{\mathrm{ret}} = -j_{\mathrm{fast}}$), B_θ is the poloidal magnetic field and R is the major radius.

It is worth noting that while the radial return current also induces a poloidal torque it is usually not of interest because of the strong neoclassical damping of the poloidal flows [45–48]. On the other hand, toroidal direction in tokamaks is nearly symmetric which allows flows to develop. Therefore, in the following when

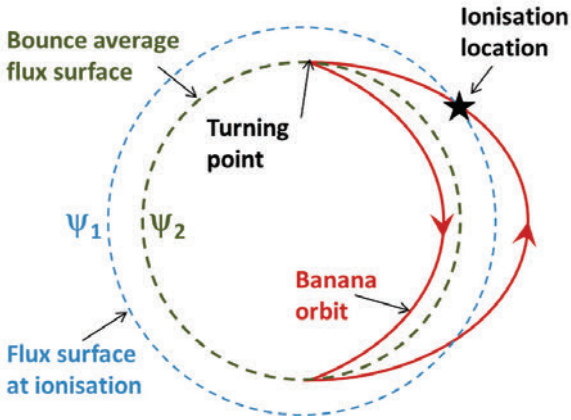

Figure 2.10. Schematic illustration of the instantaneous $j \times B$ – torque caused by the charge separation. Electron with thin orbit remains on the flux surface ψ_1 where the neutral is ionised while the trapped ion with a large orbit on average resides on its bounce averaged flux surface ψ_2. The torque on the plasma results from the radial return current that is set up to maintain quasi-neutrality.

torque is mentioned it is referring to the toroidal component of the torque.

It is neither trivial nor very accurate to use Eq. (2.17) as a basis for calculating the flux surface averaged $j \times B$ – torque profile which is of more interest, e.g. in transport modelling. A more useful form is obtained after noting that $B_\theta R = \nabla\Psi$ and that $j_{\text{fast}} = Zenv_r = Zen \cdot \dot{r} = Zen \cdot \dot{\Psi}/\nabla\Psi$ where Ψ is the poloidal flux and the dot means a time derivative. Using these identities the $j \times B$ – torque contribution is turned into a much better suited 1D form for diagnostics purposes

$$\tau_{j\times B} = -Zen\dot{\Psi}. \tag{2.18}$$

This quantity together with the collisional torque $\tau_{col} = m\Delta v_\phi R$ is used in ASCOT to estimate the total torque from fast ions into the plasma. Note that the ripple torque, which is related to the ripple induced radial current, is also captured by Eq. (2.18).

2.5 Momentum transport

Beyond analysing the ripple induced losses of torque and power, the accurate information of these quantities can be used to probe transport properties of the plasmas. In particular the evaluated torque is used to aid analysis of the toroidal momentum transport in JET plasmas. It has been shown both experimentally

[49–54] and theoretically [55–57] that momentum transport in fusion relevant tokamak plasmas is not purely diffusive but that convection also plays a role. Furthermore, although presently not very accurately quantified, momentum transport is affected by a term that is neither diffusive nor convective, thus named as the residual stress [58]. The equation governing the momentum transport in tokamak plasmas can be approximately written as [56, 59]

$$mnR\frac{\partial V_\phi}{\partial t} = \nabla \cdot \Gamma_\phi + S \tag{2.19}$$

where

$$\Gamma_\phi = mnR\left(\chi_\phi \nabla V_\phi + V_{pinch} V_\phi\right) + \Pi_{res} \tag{2.20}$$

is the toroidal momentum flux, V_ϕ is the toroidal velocity of the plasma, S is the torque source (e.g. NBI), χ_ϕ is the momentum diffusion coefficient, V_{pinch} is the convective coefficient (pinch velocity) and Π_{res} is the residual stress (the remaining part that is neither convective nor diffusive) and m, n, R are the mass, density and major radius, respectively. All terms, except mass and major radius, appearing in the above equations are functions of minor radius.

Experimentally the level of momentum transport has been observed to exceed the neo-classical level by a large factor [60–63]. Transport of momentum, like that of density or temperature, is indeed usually dominated by turbulent processes [56, 59, 64, 65]. Although much progress has been achieved in recent years to understand the processes responsible for the transport it is not possible to precisely predict the rotation even in simple L-mode plasmas. Experimental inter-machine scaling has been set up [66] but it fails to explain several observations [28]. Experimental analysis of the transport profiles χ_ϕ, V_{pinch} and the residual stress Π_{res} are thus necessary to validate the theory and to gain insight of the processes.

With many unknowns and only one differential equation Eq. (2.19) to use, special experimental arrangements are required to extract unambiguous information. In JET, the balanced neutral beam injection cannot be done due to the beamline geometry and momentum transport analysis is limited to cases where the residual stress term can be neglected. In such scenarios there are two ways to tackle Eq. (2.19). Either one looks at steady state rotation where one is left with an algebraic equation $\nabla \cdot \Gamma_\phi = -S$ with two unknowns, χ_ϕ and V_{pinch}, and is limited to estimating statistically the average transport across a number of dis-

charges (Publication III). Alternatively, one may use the information contained in the dynamical response of the plasma and make perturbation experiments where the torque source is modulated to perturb the rotation. In this case one can resolve the χ_ϕ and V_{pinch} profiles unambiguously [67].

2.5.1 NBI modulation technique

Modulation technique is a powerful experimental method for analysing various aspects of tokamak plasmas. It has been used on many tokamaks and using various modulated quantities (ECRH, ICRH, NBI, gas) e.g. [68–71]. NBI modulation, when properly executed, can be most useful for analysing momentum transport properties of plasmas. There are a number of criteria that must be met to be able to deduce χ_ϕ and V_{pinch} from the experiment. First, the target plasma to study needs to be quasi-stationary, i.e. the density, temperature and rotation should not drift or oscillate too strongly so that one can assume that the transport is the same during the time window of interest. The plasma should be MHD quiescent or at least the MHD effects should be non-interfering. Sawteeth oscillations in the core plasma or ELMs near the edge can sometimes be too strong or their frequency can get synchronised with the NBI modulation frequency to cause spurious rotation response and invalidate the data. Often the best target plasmas for the momentum transport analysis are in the low density L-mode regime or in H-mode where ELMs are absent and current profile can be tweaked to avoid sawteeth oscillations [72, 73]. Finally, the rotation measurement itself must have sufficiently good temporal and spatial resolution to resolve the dynamic plasma response accurately. In JET all these requirements are met easily after the CXRS upgrade [74].

In Fig. 2.11 the characteristic time traces of central signals are shown for a typical JET NBI modulation experiment. Plasma density, temperature, rotation and q-profile are the main parameters that determine the level of turbulent core transport and thus their modulation amplitude should remain as low as possible. The fact that the plasma in question is very stable and MHD free can be indirectly seen in the neutron measurement, which is dominated by the beam-thermal reactions; the amount of neutrons follows the NBI power waveform to the detail indicating very stable conditions. The NBI modulation frequency and amplitude have been chosen so that a sufficient perturbation ($\gtrsim$5%) in rotation is obtained

while simultaneously the density modulation is below noise level and only a limited response in ion and electron temperature is induced (typically $\lesssim 4\%$).

Note that as explained in Section 2.5.1 there are two mechanisms to transfer momentum from fast ions to the bulk plasma and they operate on different time scales; collisional torque on collisional timescale ($t \sim 100$ ms) and $j \times B$ – torque appearing almost instantaneously ($t \sim 100 \mu$s). Since the modulation cycle is shorter than the collisional time in JET it is usually the $j \times B$ – torque that is responsible for the majority of the rotation modulation amplitude. Since there are no corresponding fast mechanisms to transfer energy, at least in significant magnitudes, the modulation amplitude for temperature is automatically smaller helping to achieve sufficient rotation modulation while keeping the plasma otherwise in steady condition.

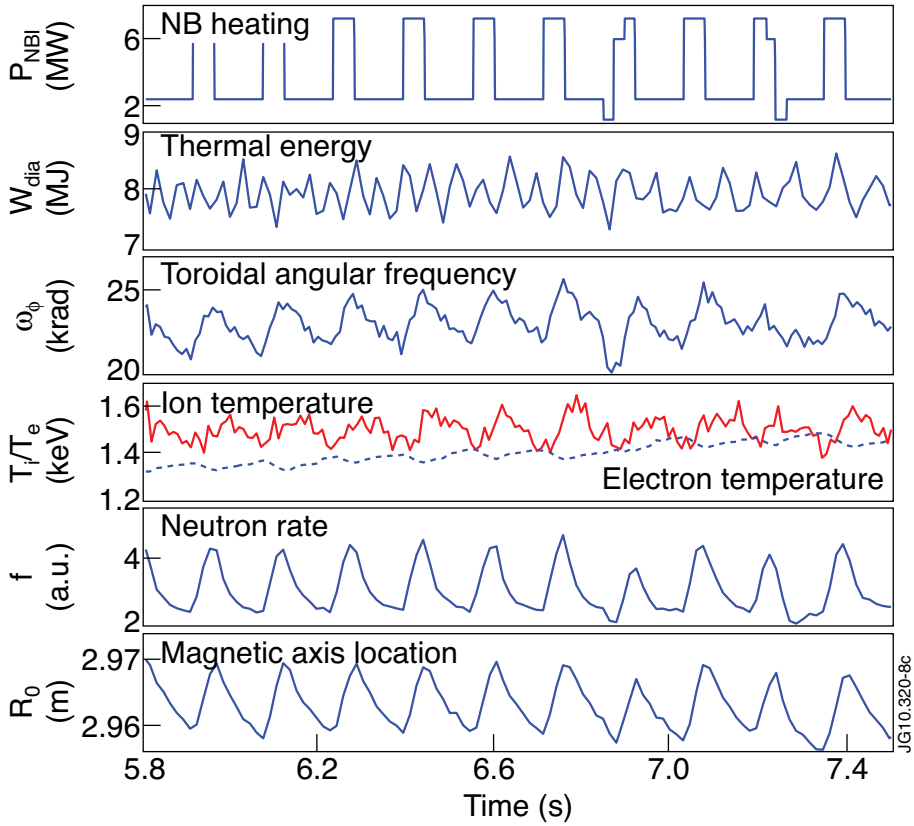

Figure 2.11. Time traces of relevant parameters in a typical momentum transport experiment in JET (#77089) utilising NBI modulation to perturb the plasma. (from Publication V)

In order to find out the prevailing momentum transport in the experiment one

can, e.g. use an iterative procedure where: (1) a transport solver is used to solve the Eq. (2.19) for V_ϕ with given profiles of χ_ϕ and V_{pinch}, (2) resulting rotation response is compared against the measured rotation and (3) χ_ϕ and V_{pinch} profiles are modified until agreement is found [67]. In Publications V–VI this procedure was automated using JETTO transport code for step 1, Fourier amplitude and phase profiles together with steady state rotation data for step 2 and a MatLab based non-linear minimisation algorithm for step 3.

3. Tools and methods

The type of work presented in this thesis consists of computer simulations and simulation aided analysis and interpretation of JET experimental data. Computer simulations are the bridge between theory and experiments and can give an idea whether the theoretical understanding (as it is implemented in the codes) of the physical phenomena is correct or whether some additional mechanisms are needed to explain the experimental data. The overall task has been to understand the fast ion behaviour in the plasma (in quiescent MHD conditions), to evaluate fast ion heat and torque sources for studying the bulk plasma properties and to validate the theory and the tools used. The difficulty lies in getting quantitative and accurate numbers from the codes that can be compared with experimental observations. This effort involves the use and development of both new and existing tools and methods to do the analysis. The most important tools and modifications to them are shortly introduced in the following.

3.1 ASCOT code and upgrades

ASCOT [75, 76] (**A**ccelerated **S**imulations of **C**harged particle **O**rbits in **T**ori) is a guiding centre following code with Monte Carlo operators for added physics, developed from the early 90's in VTT (Technical Research Centre of Finland) and Aalto University (formerly HUT, Helsinki University of Technology).

The standalone ASCOT is primarily used for fast particle studies where the particle ensemble of interest can be treated as a tracer species which does not self-interact or modify significantly the plasma itself. Monte Carlo techniques are used to add physics such as Coulomb collisions or ICRH interactions [77]. Many interesting and complicated fast particle physics can be studied with ASCOT by

simply imposing a realistic three dimensional magnetic perturbation, e.g. toroidal field ripple[78], NTMs [79, 80] or external perturbation coils [81–83] on top of the equilibrium field. The advantage of the orbit following MC codes such as ASCOT is that it is straightforward to study many interconnected and complex phenomena by adding MC operators on top of each other. For comprehensive details of ASCOT the reader is referred to the earlier work [84, 85] where more elaborated description of the equations of motion, collision operator etc. can be found.

As part of this thesis ASCOT has been upgraded to calculate the torque on the plasma coming from fast ion radial transport as described in Section 2.3.1. This supplied ASCOT with a unique feature within the orbit following codes in the world: a possibility to calculate fast ion ripple torque in real experimental condition. The torque evaluation feature has been utilised on several occasions, with and without ripple, to estimate fast ion torque and its influence on plasma rotation. Furthermore, ASCOT was integrated into the JET application management system (JAMS), featuring a graphical user interface, and to relevant codes within it to facilitate the JET NBI modelling capability. Without these and related code enhancements much of the subsequent results could not have been obtained.

3.2 JET integrated transport code

JET integrated transport code (JINTRAC) is a transport solver used at JET. At the core of JINTRAC is a 1.5D transport code JETTO [86] which solves a set of differential equations for flux surface averaged plasma density, temperature and momentum. The half a dimension is credited by the inclusion of plasma shape information through the flux surface averaging. For solving the time evolution of the plasma parameters JETTO is coupled to various models and sophisticated codes (incl. ASCOT) to provide information on transport, sources and magnetic equilibrium [87]. The integrated code can then be advanced sequentially to yield a consistent evolution of plasma density, temperature and rotation. A schematic overview of the system is shown in Fig. 3.1.

The evolution of density, temperature and momentum are coupled together (e.g. increasing density means less available power per particle which results in lower temperature and so on) and for full solution a coupled set of differential equa-

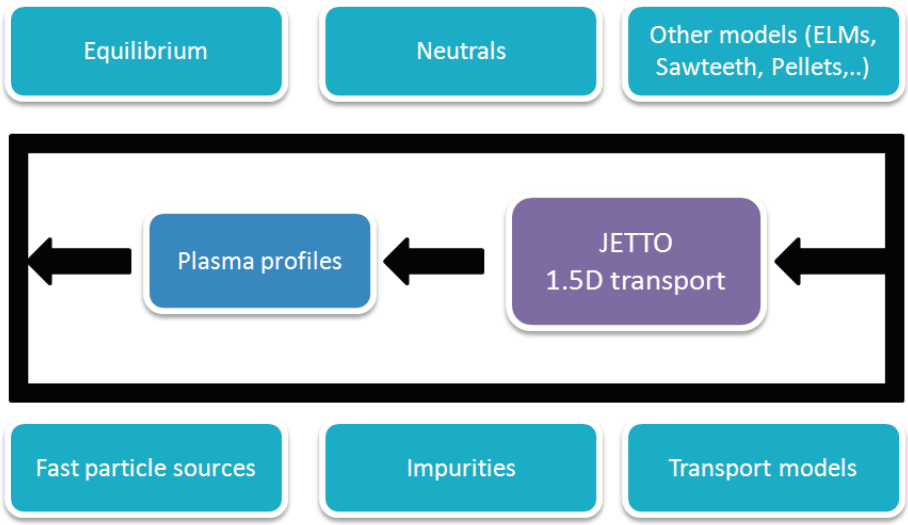

Figure 3.1. Schematic view of the JINTRAC operation. The modules for equilibrium, neutrals etc. feed information for the transport code JETTO that calculates the evolution of the plasma profiles based on their input. The plasma profiles are input for the modules which then evaluate the next round of input for JETTO. ASCOT is included in the Fast particles sources box.

tions need to be solved. JINTRAC can be used both in predictive and in interpretative mode. In predictive mode the transport coefficients (e.g. χ_ϕ and V_{pinch}) are given by the user, by some model or theory together with initial and boundary conditions and the evolution of plasma profiles are obtained. In interpretative mode JINTRAC takes the time histories of experimentally measured plasma profiles together with the calculated sources to yield the effective diffusion coefficients for momentum, temperature and density. The effective momentum diffusion coefficient $\chi_{\phi,\mathrm{eff}}$ for example is obtained through the momentum flux $\Gamma_\phi = mnR\chi_{\phi,\mathrm{eff}}\nabla V_\phi$ i.e. it assumes all flux is caused by diffusion. The predictive mode can be used in an iteration loop to fit the transport profiles that best reproduce the experimental measurements (see next Section).

During the course of this work JINTRAC was upgraded with a new module to provide a more accurate description of the NBI source. The module is based on ASCOT which was adapted for time dependent use and interfaced with relevant JINTRAC modules and experimental database. ASCOT became an important module within the box labelled as Fast particle sources in Fig. 3.1. This upgrade made it possible to calculate a realistic NBI deposition profile with either experimental or user defined NBI characteristics (power, energy, PINI mix) and to take

into account all relevant neoclassical physics from large orbit effects to charge exchange (CX) losses with appropriate dynamics.

3.3 Momentum transport analysis technique

In order to deduce the prevailing transport properties from experimental plasma we have developed an automated iterative scheme around JINTRAC using MatLab tools. For enabling this scheme a special version of JINTRAC was first made which allows externally provided radial profiles of χ_ϕ and V_{pinch} to be used in the predictive momentum transport simulation. Within the MatLab code JINTRAC was called repeatedly to provide the predicted toroidal rotation corresponding to the given χ_ϕ and V_{pinch} profiles. The objective is to vary these profiles until the best fit between the simulated toroidal rotation and the experimentally measured toroidal rotation is found. For finding the optimal profiles efficiently a built-in MatLab non-linear optimisation algorithm was employed.

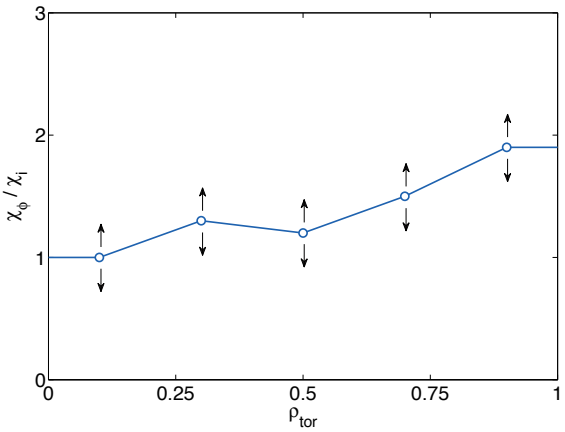

Figure 3.2. An example of profile parametrisation for finding the optimal transport profiles. The free parameters are connected by linear interpolation. The values at the boundaries are fixed to the closest point being optimised. The vertical arrows indicate that the values at the node locations are varied until the optimum profiles are found.

Although it seemingly is a simple task to find the optimal transport profiles to best match the experimental measurements, there are a couple of caveats that need closer attention. First of all, profile optimisation is an inherently multi-dimensional problem the dimensions being the sum of parameters needed to con-

struct the profiles. We chose to represent the profiles with 3 to 6 discrete points equispaced in radius with linear interpolation in between as illustrated in Fig. 3.2. This gives a 6 to 12 dimensional space to be scanned (using 2 profiles). It is rather obvious that in a multi-dimensional system several local minima can exist. To improve the robustness of finding the best fit (global minimum) the minimisation algorithm is run several times each with random initial condition. To speed up convergence and the likelihood of finding physically relevant profiles a certain level of smoothness was required of the transport profiles by penalising large second derivatives. Finally, it should be mentioned that not all problems like these can be solved uniquely. It is a matter of each individual case to check if such situation exists. Fortunately, the repetition of the optimisation with several randomly chosen initial conditions usually helps in the identification process.

3.4 ICRH modelling tools

Ion cyclotron resonance heating (ICRH) is in many ways a very complicated process to simulate [26]. For instance the absorption efficiency depends on the resonant ion distribution (in space and velocity space) both of which change during the heating, i.e. the process is non-linear unlike NBI in most relevant cases. The codes for ICRH are typically very specialised and require a self-consistent time-dependent treatment. In the future some recent work [77, 88] on ICRH theory is expected to provide orbit following codes such as ASCOT the capability to simulate ICRH as part of the integrated tokamak modelling (ITM) suite [89]. Present ICRH modelling work, however, is based on PION [90, 91] and FIDO [92] codes, described in the following.

PION is a simplified Fokker-Planck code for ICRH modelling. It is routinely used in JET and it has been extensively benchmarked against JET ICRH experiments (see e.g. [90, 91]). Unlike most of the ICRH codes PION is rather fast taking only from a few minutes to few hours to calculate the heating profiles from ICRH for the complete heating phase which can be over 10 seconds. PION solves the evolution of the pitch angle averaged fast ion distribution function f

$$\frac{\partial f}{\partial t} = \hat{C}(f) + \hat{Q}(f) \tag{3.1}$$

using finite differencing method. Here $\hat{C}$ is the collision operator and $\hat{Q}$ is the

quasi-linear RF diffusion operator [24] with an RF diffusion coefficient

$$D_{RF} \sim |E_+ J_{n-1}(k_\perp v_\perp/\Omega_{ci}) + E_- J_{n+1}(k_\perp v_\perp/\Omega_{ci})|^2 \tag{3.2}$$

where $E_+(E_-)$ are right (left) hand polarised electric field components, $k_\perp$ and $v_\perp$ is the perpendicular wave number of the fast wave, n is the harmonic number of the resonance and J_m are the Bessel functions of the first kind.

PION is a simplified code with a number of limitations and it cannot output detailed information of the resonant ion distribution function. However, in several common heating scenarios it has been shown to accurately predict the ICRH power absorption and the resulting fast ion energy content [93, 94]. In the work done for Publication I the role of PION is to provide the amount of energy absorbed by the resonant species as well as to calculate the ICRF antenna power spectrum to be used with the more sophisticated ICRH code FIDO.

FIDO solves the orbit averaged Fokker-Planck equation Eq. (3.1) using Monte Carlo methods [95, 96]. It goes one step further in orbit averaging than ASCOT. Where ASCOT follows the location of the guiding centre FIDO keeps track of the invariants of motion $(\tilde{E}, \Lambda, \tilde{P}_\phi)$ which are normalised versions of the invariants presented in Eqs. (2.4-2.6). In effect FIDO averages also over the poloidal motion of the particle. The collisions and RF interactions are modelled by Monte Carlo kicks in the invariant space. This approach has the obvious benefit of being much less CPU intensive than the guiding centre approach since the poloidal motion of the particles is not followed. Nevertheless, FIDO simulations last from several hours to several days even in massively parallel computing environment due to the large number of particles needed to accurately represent the high energy tail in the fast ion distribution.

For running FIDO the user must give the power spectrum of the fast wave as input such that it produces a correct amount of absorbed power. The shape of the spectrum is determined by the geometry of the antenna and the phasing between the current straps but the amplitude is often not known in advance. For this reason PION is used, as mentioned above, to provide the amount of power absorbed by the resonating ions. The power spectrum used in FIDO can then be normalised using an iterative procedure. Usually already one or two iterations will produce an accurate power absorption in FIDO. In the end FIDO delivers detailed information of the fast ion distribution function which can be compared

with experimental measurements such as the measurement from the neutral particle analyser (NPA) [97] in Publication I.

4. Results

4.1 Fast ion energy diffusion barrier confirmed in modelling

Quasi-linear theory predicts an effective energy diffusion barrier near $E = E^*$ where the RF diffusion coefficient D_{RF} in Eq. (2.12) has its first minimum. In order to test experimentally the validity of the prediction a dedicated experiment was planned on JET. The motivation for this work as reported in Publication I was the experimental validation of the theory and the benchmarking of the existing ICRH codes (FIDO/PION). The best suited ICRH scenario for this experiment was found to be the second harmonic heating scheme. Firstly, it allows to use low enough toroidal magnetic field ($E^* \sim B^2/n_e$) to put the energy diffusion barrier in the energy range where it can be measured by the neutral particle analyser (NPA) [97]. NPA measures the escaping fast neutrals from about 200 keV up to around 1.2 MeV (depending on species). Fast neutrals are born in charge exchange reactions between cold neutrals and fast ions which, in the presence of ICRH, are dominantly the resonant species and can thus yield a representative description of the ICRH accelerated ion population. Secondly, the second harmonic scheme is more efficient than higher harmonic heating schemes at low energies to pull out a high energy tail [98].

To test this theory, three plasma discharges were utilised to make two pairwise comparisons. First pair is a low density & low power plasma versus a high density & high power plasma. The purpose here is to vary the location of the barrier E^* via density variation while maintaining equal heating power per particle by having more ICRH power in the high density discharge. The second pair is formed between discharges with equal density but with different heating power. In this

case, if the quasi-linear theory is valid, similar shaped fast ion tail would develop in both discharges. Otherwise, the significantly higher heating power per particle would lead to a markedly longer tail in the energy distribution.

Fig. 4.1 shows the NPA measurements together with FIDO/PION simulation of the fast ion energy distribution for these discharges. It is apparent that the modelling agrees well with the measurements and that they both show distributions which drop rapidly at high energies. In the first harmonic ICRH heating scheme the resonant ion energy distribution would usually decay exponentially forming a straight line in the logarithmic plot. Here the fast ion population decreases increasingly faster towards higher energies which is expected from the quasi-linear theory at this range of parameters. Furthermore, by comparing the discharges #58738 and #58739 (low power v. high power) one can see that the shapes and the fall-off energies of the distributions are same as expected from quasi-linear theory. Comparison between discharges #58734 and #58738 (high density v. low density) also agrees with the theory as with similar heating power per particle the distribution falls off earlier in the high density discharge. For additional pairwise comparison of experimental data, see Publication I, Fig. 4.

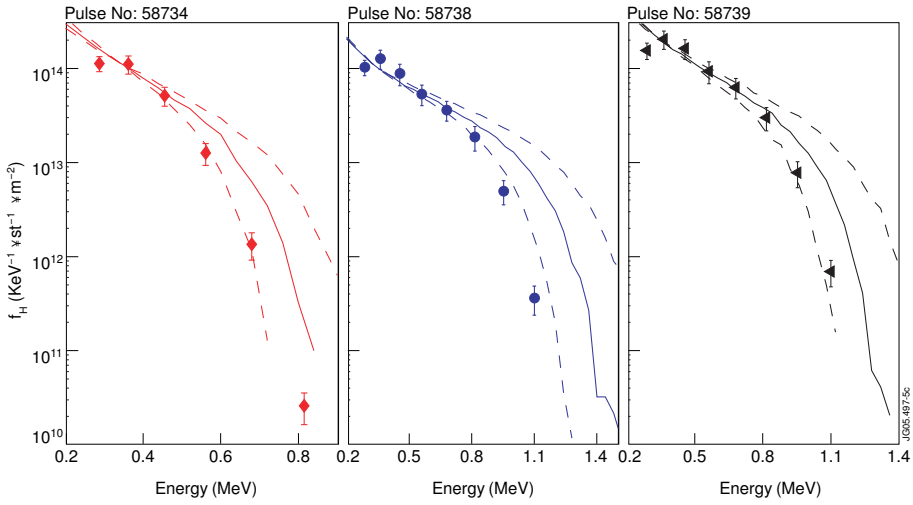

Figure 4.1. Comparison of the measured and simulated fast ion energy distributions in second harmonic hydrogen minority ICRF heated plasmas. a) high power & high density b) low power & low density c) high power & low density. Points with errorbars are the experimental measurements, full lines are the simulated distributions and dashed lines indicate the sensitivity of the simulations to 10% change in electron density (from Publication I).

4.2 Fast ion ripple torque calculation using the orbit following code ASCOT

Toroidal field ripple, as described in Section 2.3.1, can have a significant impact on plasma performance and thus it can influence the economics of fusion power. In the ITER design the number of toroidal field coils has been fixed to 18 which could cause ripple as high as 1.2%. In order to help to assess the consequences that might result from this large level of ripple, JET launched a dedicated experimental ripple campaign C18 to study its effect on, e.g. the plasma confinement, H-mode threshold, ELMs and fast ion losses. The key ingredient for the campaign, unique to JET, is its ability to control the level of ripple by driving unequal currents in even and odd numbered TF coils. This allows isolating the influence of ripple by running identical discharges where only the level of ripple is changed.

While it is relatively easy to show from the experimental data that ripple influences the plasma characteristics the quantitative understanding of these observations requires validated tools that are able to take into account the effect of ripple. To support the analysis of the experimental data ASCOT code was upgraded as a part of this thesis so that the influence of TF ripple on fast ion torque and losses could be estimated. In short, this work involved interfacing the orbit following ASCOT with PENCIL [99] code to obtain the 3D ionisation source of the JET neutral beam system. With this source ASCOT was used for the slowing down simulation during which the orbit losses and ripple effects occur. Furthermore, torque diagnostics were added to calculate the total torque from the injected NBI so that it includes both the slow collisional torque and the instantaneous $j \times B -$ torque.

As a result of the ASCOT implementation work the first ASCOT analysis of JET NBI torque in presence of magnetic field ripple was reported in Publication II. It was shown that the NBI torque, which in JET is normally in co-current direction, is significantly reduced by the ripple when the magnitude of the ripple increases above $\delta > 0.35\%$ (see Fig. 4.2).

This observation was consistent with the experimental data that showed little effect from ripple if $\delta < 0.35\%$ [100]. One somewhat surprising finding from the simulations was that the counter torque in JET was mainly generated by the radial ripple diffusion of the poloidally trapped ions instead of the losses of the toroidally trapped ions. According to ASCOT simulations the ripple trapping in

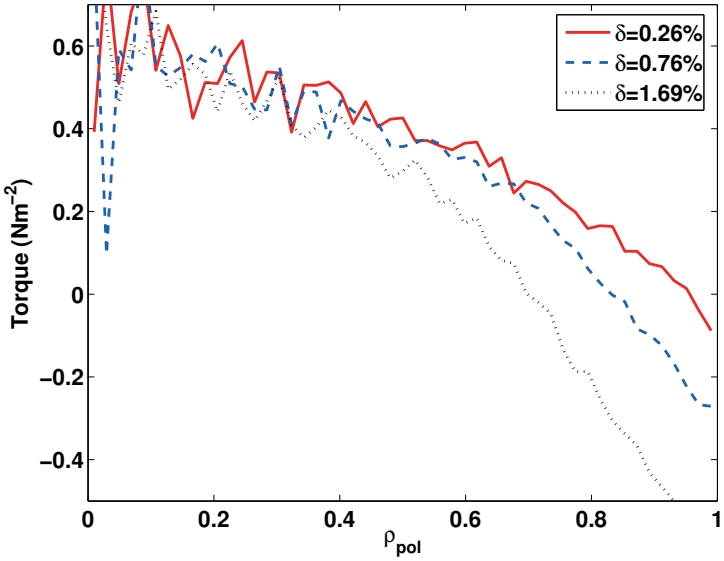

Figure 4.2. NBI torque profile for three different ripple magnitudes δ. Note how the magnitude of the negative (counter-current) torque increases towards the separatrix while the torque inside mid radius is unaffected even at the highest ripple (from Publication II).

JET becomes significant in NBI heated plasmas only at ripple levels larger than 1.5%. This was good news also because the areas where the ripple trapped ions hit the first wall are not well protected and therefore material melting could result more easily.

4.3 Fast ion ripple torque influence on plasma rotation

As an application of the newly obtained torque calculation functionality a mixture of H-mode experiments were analysed with ASCOT. The various plasmas had different density and temperature profiles as well as a broad selection of NBI heating power and alignment. Most of these plasmas were run with 1% ripple. The toroidal rotation in these plasmas was compared with the ASCOT calculated torque as shown in the Fig. 4.3. It was found that the fast ion ripple torque, which always points in the counter current direction, reduces the NBI torque significantly and depends on the alignment and deposition profile. With 1% ripple and perpendicular NBI the fast ion ripple torque can in some cases result in a counter current torque that completely cancels the NBI torque. The measured

total toroidal angular momentum of the plasmas correlates well with the ASCOT calculated torque suggesting that fast ions are responsible for the major part of the ripple generated toroidal torque.

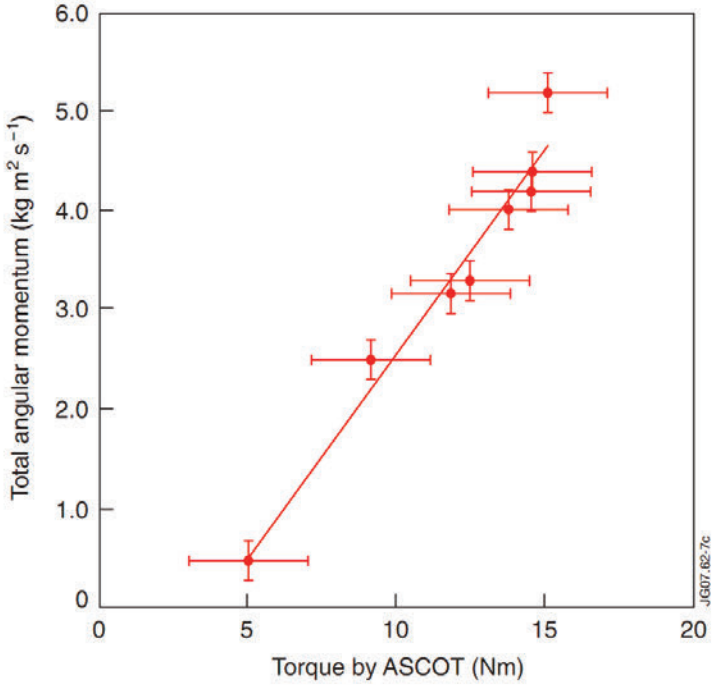

Figure 4.3. The measured total angular momentum versus ASCOT calculated NBI torque in presence of TF ripple (from Publication III).

However, it was also found that for some plasmas the edge region was rotating in counter current direction while ASCOT still predicted positive co-current total torque. This could signify an unaccounted missing torque contribution. One possible explanation for the observation is a contribution from thermal ions, e.g. neoclassical toroidal viscosity (NTV) as demonstrated in DIII-D [20].

4.4 Momentum transport in NBI heated JET plasmas

Toroidal rotation of the plasma is controlled by the momentum sources, e.g. NBI, and the radial transport of the momentum as given by Eq. (2.20). With the accurate knowledge of the sources, using codes like ASCOT, and the measured toroidal rotation, information of the momentum transport can be obtained experimentally with different approaches as described in Section 2.5.

The statistical approach was used in Publication III where the toroidal rotation of a number of JET discharges were analysed. Here only the steady state information of rotation and sources were used and the left hand side of Eq. (2.19) vanishes and momentum flux is obtained by simply integrating the known steady state source over the plasma volume $\Gamma_\phi = \int dvS$. Neglecting the residual stress and denoting the angular momentum density as $\Omega = mnRV_\phi$ the Eq. (2.20) can be written as

$$\frac{\nabla\Omega}{\Gamma_\phi} = -\frac{V_{pinch}}{\chi_\phi}\frac{\Omega}{\Gamma_\phi} - \frac{1}{\chi_\phi} \tag{4.1}$$

Since the terms $\nabla\Omega$, Ω and Γ_ϕ can be measured or calculated the unknowns χ_ϕ and V_{pinch} can now be obtained statistically.

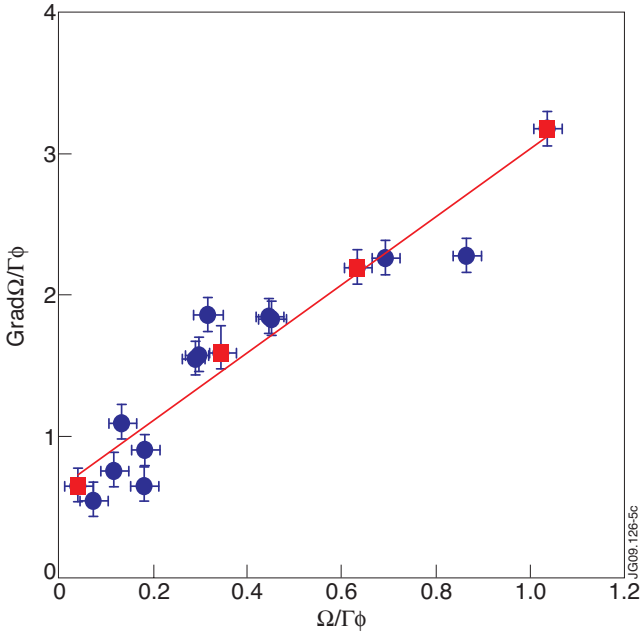

Figure 4.4. Normalised momentum density gradient versus normalised momentum density for a number of JET H-mode discharges. Square markers are ones from a ripple scan (from Publication IV).

In Fig. 4.4 the normalised gradient of the angular momentum density $\nabla\Omega/\Gamma_\phi$ is plotted against the normalised angular momentum density Ω/Γ_ϕ for a number of different discharges. The values shown are obtained at mid radius. By fitting a line into the scatter plot one can obtain the ratio V_{pinch}/χ_ϕ from the slope and $1/\chi_\phi$ from the crossing of the y-axis. It should be repeated that using this method based on steady state form of Eq. (2.19) only the average pinch velocity

and momentum diffusion coefficient across the discharges can be obtained. Nevertheless, by repeating the analysis for additional radial positions it was found that the magnitudes and trends of the radial profiles for χ_ϕ and V_{pinch} are similar than previously found using NBI modulation technique for low density L-mode plasmas [52]. The work thus not only confirms the earlier analysis but also shows that a non-zero convective momentum transport V_{pinch} is robustly found in large data sets and that similar processes are at play universally across various plasma conditions.

4.5 Experimental validation of the fast ion ripple torque calculation

While in earlier Publications the NBI torque in presence of TF ripple was calculated and used in further analysis, it was not until Publication V that it could be validated experimentally. The earlier efforts to validate the guiding centre following approach to account the ripple effects were limited to comparing quantities that did not include torque either because experimental data was not available or no other code could calculate the ripple torque. Nevertheless, other ripple effects have been successfully validated earlier, e.g. ripple induced fast ion heat loads on first wall have been compared against experimental data deduced from infra-red measurements [101, 102].

The main problem of validating the torque calculation arises nevertheless from the fact that the torque itself cannot be measured. Torque can only be inferred from Eqs. (2.19) and (2.20) when the rotation profile is measured and the transport is known. However, as discussed earlier, only two unknowns can be deduced experimentally from Eqs. (2.19) and (2.20) even with the dynamic information kept. With the addition of a significant TF ripple, the NBI torque source S itself becomes unknown. One is thus left with too many unknowns to solve from a single equation. The way forward from the apparent dead end is to design an experiment with negligible residual stress for two nearly identical discharges; one without ripple and one with ripple. The data from the ripple-free discharge can be used to find χ_ϕ and V_{pinch} profiles as described in Section 2.5.1. Then, with the just resolved transport coefficients, toroidal rotation can be found for the plasmas with TF ripple using the torque calculated by ASCOT. Should the torque calculation be accurate, the experimental and calculated rotation profiles will be consistent.

In order to use this experimental approach to validate ASCOT ripple torque calculation the code first had to be upgraded for time-dependent operation to obtain $S(r,t)$. With this new functionality the NBI torque profile was calculated for three discharges (#77089-#77091) with nearly identical plasma profiles. Ion and electron temperature and density profiles as well as the q-profiles were identical within the measurements accuracy and the density profiles differed less than 10% between the discharges. The calculations used a time resolution of 5 ms to obtain good statistics and sufficiently accurate dynamic information of the torque sources. The torque profiles as calculated by ASCOT were markedly different between the discharges (see Fig. 11, Publication V) in line with expectations and thus provide a nice set of data for validation.

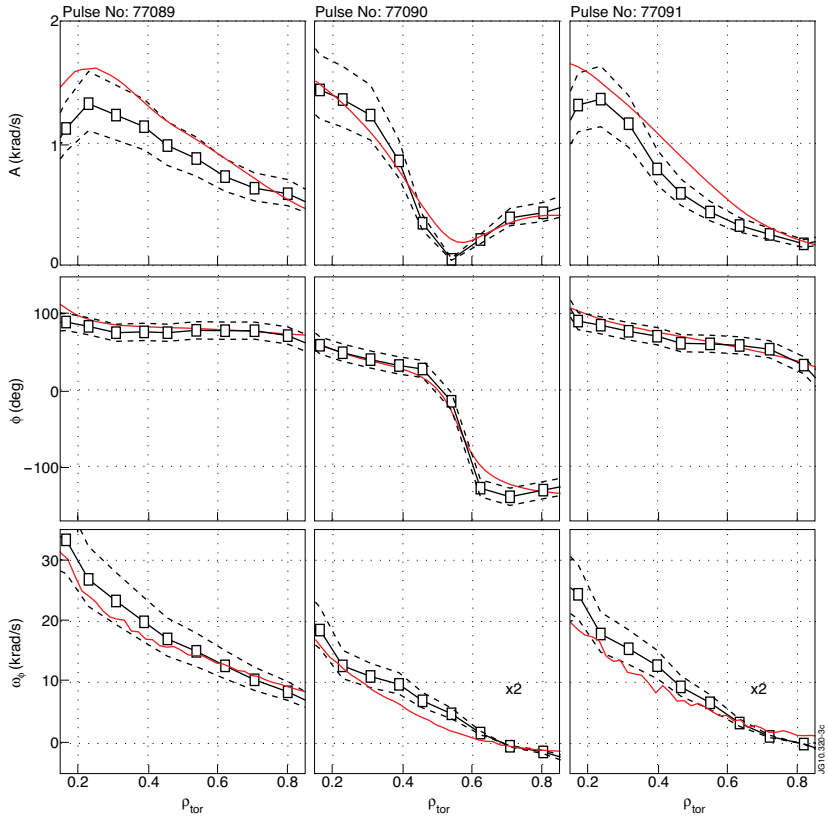

Figure 4.5. Amplitude, phase and steady state profiles for toroidal rotation (red = calculations, black = measurements). First column corresponds to the discharge #77089 ($\delta = 0.08\%$, perp. NBI), second column to #77090 ($\delta = 1.5\%$, perp. NBI) and third column to #77091 ($\delta = 1.5\%$, tang. NBI). Dashed lines are to guide the eye and give rough estimates of the error (from Publication V).

Using the procedure outlined above and in Section 2.5.1 the momentum transport profiles were iteratively solved for the reference discharge without ripple (#77089). With the transport found this way together with the ripple torque calculations the transport code predictions and experimental rotation measurements could be compared. Figure 4.5 gives the final result of this procedure. The left column shows the Fourier amplitude and phase at the 6.25 Hz modulation frequency together with the steady state rotation profile for the reference discharge without ripple. The middle and the right columns show the same data for the discharges with 1.5% ripple. Perpendicular NBI was used in the discharge #77090 whereas tangential NBI was used in #77091. In all plots one can see that the simulated rotation with torque calculated by ASCOT (red lines) agrees well with the experimentally measured toroidal rotation profiles (black squares) which suggest that the torque is evaluated correctly. The dashed lines give indication of the measurement errors in the rotation data. The plots also show that the counter current torque from ripple is significantly larger in the case of perpendicular NBI injection in line with the theoretical expectations.

It should be mentioned that although the ripple effect has been found to be strongest for fast ions both in theory and in simulations, the introduction of non-axisymmetric perturbations also affects thermal particles through the neoclassical toroidal viscosity (NTV) [36–40]. While there is experimental evidence showing that this effect is important with certain excited low toroidal harmonic perturbations [20] there have not been experimental observations that suggest that this effect would be particularly strong in the JET TF ripple field.

4.6 Parametric study of momentum transport using NBI torque modulation

The torque from NBI ions can be used to gain information of the momentum transport properties of the plasmas as explained in Sec. 2.5.1. The key ingredient here is the ability to accurately calculate the torque. NBI modulation technique has been used previously to show that momentum transport is not purely diffusive, as expected from the characteristics of the ion energy diffusion, but that a convective term also plays a role [51, 52]. In Publication VI momentum transport and in particular its convective part (pinch) is studied using the NBI modulation technique in JET plasmas. The aim is to find out how the pinch depends on plasma

parameters in an effort to make predictions for ITER. The importance of this topic is realised when noting that even a relatively small level of pinch in ITER could provide a mechanism for achieving a sufficient level of rotation to mitigate turbulence [103] and to avoid harmful mode locking and subsequent disruptions [20].

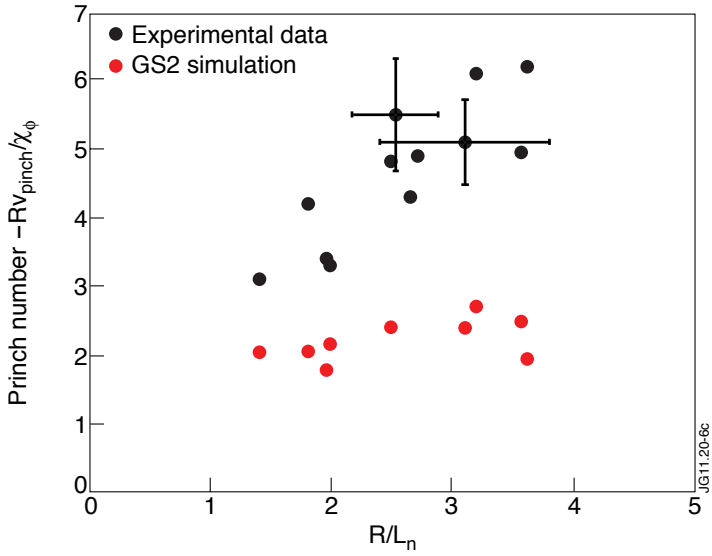

Figure 4.6. Comparison between experimental and numerical scaling of the pinch number RV_{pinch}/χ_ϕ against the inverse of the normalised density gradient scale length (from Publication VI).

The dependencies of the pinch on plasma parameters are studied by making a series of NBI modulation experiments with as wide parameter range as possible. The theoretically motivated parameters of interest that are varied are the q-profile, collisionality and the density gradient (more specifically the inverse of the normalised density gradient scale length $R/L_n = R\nabla n/n$) [56]. The experimental profiles for χ_ϕ and V_{pinch} are deduced using the iterative transport analysis based on JINTRAC (Sec. 2.5.1) with NBI torques calculated using well agreeing codes TRANSP [104] and/or ASCOT. It is found that the variation of pinch against q and collisionality is weak while the dependence with the R/L_n is strong. The weak dependence on the collisionality agrees well with the theory based modelling [105]. Figure 4.6 shows the pinch number against the inverse of the density gradient scale length for the experimental and numerical data from turbulence simulations using GS2 [106] code in linear mode. Linear simulations are thought to be sufficiently accurate for momentum transport analysis in ITG dominated plasmas

where they agree quite well with non-linear simulations [107–110]. Both experimentally and in simulations the pinch number increases with R/L_n although the dependence in the experimental data is clearly stronger (by roughly a factor or three). The reason for this difference is not yet understood and it requires more analysis to resolve. The result suggests that peaked density profiles could help ITER to achieve higher rotation and rotation shear even with the weak external torque sources in the plasma core.

5. Summary and discussion

Fast ions have several important roles in fusion plasmas. The 3.5 MeV alpha particles born in the D-T fusion are crucial in order to maintain the high temperature required for the fusion to occur while NBI+ICRF ions are needed to heat up the plasma during the start-up phase and to control the plasma burn. Understanding the generation of fast ions as well as the mechanisms that control their losses and distribution in the plasmas is important in order to successfully operate future fusion power plants. Furthermore, the accurate fast ion modelling capability makes it possible to use them as a tool for studying the bulk plasma properties.

Ion cyclotron heating is currently seen as the best option for heating bulk ions into the optimal 10–20 keV energy range for fusion burn in ITER. In this work, a prediction from the quasi-linear theory was tested with ICRF codes PION and FIDO. According to the theory the RF diffusion coefficient becomes small at certain energies due to the finite Larmor radius effects which is expected to manifest itself by strongly decaying fast ion tail around this energy. Simulations of this phenomenon agreed well with the experimental measurements and confirmed the importance of the finite Larmor radius effects in controlling the fast ion distribution function. This effect allows one to have some control over the tail of the ICRF heated fast ion distribution by adjusting the magnetic field strength and the electron density as required by the experiment.

During the course of this thesis the orbit following Monte Carlo code ASCOT code has been upgraded to calculate the fast ion torque to the plasma with and without ripple. ASCOT was also modified for time-dependent calculations which is crucial for analysing, e.g. the NBI modulation experiments. Furthermore, ASCOT was integrated into the JAMS (JET Application Management System) and interfaced with JETTO and experimental database to allow routine analysis of

NBI heated discharges at JET. A realistic fast ion ripple torque in presence of collisions and true geometry was first calculated with ASCOT.

The numerical analysis of fast ion losses and the effect of ripple on rotation in the JET ripple campaign have contributed in the ITER design recommendation that calls for a reduction of the ITER intrinsic ripple magnitude $\delta \sim 1.2\%$ to as low as reasonably achievable [111]. This could be achieved using in-vessel ferritic inserts (steel plates) [112] similar to as already demonstrated in JFT-2M and JT-60U [113–115]. Both ASCOT simulations and JET experiments have shown that for $\delta < 0.3\%$ the fast ion ripple losses and counter current torque become small and that the deterioration of the plasma performance becomes insignificant.

NBI modulation technique with ASCOT calculated torque was used for studying the momentum transport properties of plasmas. It was shown that the convective momentum transport (inward pinch) is present in a broad range of NBI heated discharges and that it does not depend significantly of the plasma collisionality while a relatively strong dependence was found against the density gradient scale length L_N. The existence of such inward pinch could allow peaking of the rotation profile in ITER even with the expected weak momentum sources in the core plasma.

The NBI modulation technique was also utilised in an effort to experimentally validate the ripple torque calculations for the first time. It was found that the torque calculated by ASCOT did successfully reproduce the experimentally measured rotation confirming that the counter current ripple torque is accurately calculated with the guiding centre approach. Having an experimentally validated tool for taking into account fast ion ripple effects makes it possible to apply it for predictive analysis in ITER and beyond.

Bibliography

[1] *World energy outlook 2011*. IEA, International Energy Agency OECD, Paris, 2011. ISBN 978-92-64-12413-4, Online.

[2] *BP energy outlook 2030*. British Petroleum, London, 2012, Online.

[3] Tokamak. In *The Great Soviet Encyclopedia, 3rd Edition*.

[4] M. Keilhacker, A. Gibson, C. Gormezano, et al. High fusion performance from deuterium-tritium plasmas in JET. *Nuclear Fusion*, 39(2):209, 1999, Online.

[5] ITER Technical Basis 2002. ITER EDA. *Documentation Series No 24. (Vienna: IAEA)*, 2002, Online.

[6] ITER Organisation. `http://www.iter.org/`.

[7] K. Ikeda. ITER on the road to fusion energy. *Nuclear Fusion*, 50(1):014002, 2010, Online.

[8] J. Wesson and D.J. Campbell. *Tokamaks*. Oxford engineering science series. Clarendon Press, 1997. ISBN 9780198562931.

[9] K. Tobita, K. Tani, Y. Kusama, et al. Ripple induced fast ion loss and related effects in JT-60U. *Nuclear Fusion*, 35(12):1585, 1995, Online.

[10] M. H. Redi, R. V. Budny, D. S. Darrow, et al. Modelling TF ripple loss of alpha particles in TFTR DT experiments. *Nuclear Fusion*, 35(12):1509, 1995, Online.

[11] M. H. Redi, M. C. Zarnstorff, R. B. White, et al. Collisional stochastic ripple diffusion of alpha particles and beam ions on TFTR. *Nuclear Fusion*, 35(10):1191, 1995, Online.

[12] H. H. Duong, R. K. Fisher, S. S. Medley, et al. The effect of toroidal field ripple on confined alphas in TFTR DT plasmas. *Nuclear Fusion*, 37(2):271, 1997, Online.

[13] K. Miyamoto. *Plasma physics and controlled nuclear fusion*. Springer, Berlin New York, 2005. ISBN 9783540242178.

[14] V. G. Kiptily, F. E. Cecil, O. N. Jarvis, et al. γ-ray diagnostics of energetic ions in JET. *Nuclear Fusion*, 42(8):999, 2002, Online.

[15] D. S. Darrow, H. W. Herrmann, D. W. Johnson, et al. Measurement of loss of DT fusion products using scintillator detectors in TFTR (invited). *Review of Scientific Instruments*, 66(1):476–482, 1995, Online.

[16] S. Baeumel, A. Werner, R. Semler, et al. Scintillator probe for lost alpha measurements in JET. *Review of Scientific Instruments*, 75(10):3563–3565, 2004, Online.

[17] R. L. Miller and R. E. Waltz. On the nature of rotational shear stabilization in toroidal geometry and its numerical representation. *Physics of Plasmas*, 1(9):2835–2842, 1994, Online.

[18] K. H. Burrell. Effects of E x B velocity shear and magnetic shear on turbulence and transport in magnetic confinement devices. *Physics of Plasmas*, 4(5):1499–1518, 1997, Online.

[19] P. Mantica, D. Strintzi, T. Tala, et al. Experimental study of the ion critical-gradient length and stiffness level and the impact of rotation in the JET tokamak. *Phys. Rev. Lett.*, 102:175002, Apr 2009, Online.

[20] A. M. Garofalo, M. S. Chu, E. D. Fredrickson, et al. Resistive wall mode dynamics and active feedback control in DIII-D. *Nuclear Fusion*, 41(9):1171, 2001, Online.

[21] G. Duesing, H. Altmann, H. Falter, et al. Neutral beam injection system. *Fusion Technology*, 11(1):163–202, 1987, Online.

[22] Heating ITER Physics Expert Group on Energetic Particles, Current Drive, and ITER Physics Basis Editors. Chapter 6: Plasma auxiliary heating and current drive. *Nuclear Fusion*, 39(12):2495, 1999, Online.

[23] J. P. Freidberg. *Plasma Physics and Fusion Energy*. Cambridge University Press, 2008. ISBN 9780521733175.

[24] T. H. Stix. Fast-wave heating of a two-component plasma. *Nuclear Fusion*, 15(5): 737, 1975, Online.

[25] D. Anderson. Distortion of the distribution function of weakly RF heated minority ions in a tokamak plasma. *Journal of Plasma Physics*, 29(02):317–323, 1983, Online.

[26] R. Cairns. *Radiofrequency heating of plasmas*. A. Hilger, Bristol, England Philadelphia, 1991. ISBN 0750300345.

[27] L.-G. Eriksson, T. Hellsten, M. F. F. Nave, et al. Toroidal rotation in RF heated JET plasmas. *Plasma Physics and Controlled Fusion*, 51(4):044008, 2009, Online.

[28] M. F. F. Nave, T. Johnson, L.-G. Eriksson, et al. Influence of magnetic field ripple on the intrinsic rotation of tokamak plasmas. *Phys. Rev. Lett.*, 105:105005, Sep 2010, Online.

[29] T. Hellsten, T. J. Johnson, D. Van Eester, et al. Observations of rotation in JET plasmas with electron heating by ion cyclotron resonance heating. *Plasma Physics and Controlled Fusion*, 54(7):074007, 2012, Online.

[30] Y. Lin, J. E. Rice, S. J. Wukitch, et al. Observation of ion-cyclotron-frequency mode-conversion flow drive in tokamak plasmas. *Phys. Rev. Lett.*, 101:235002, Dec 2008, Online.

[31] Y. Lin, P. Mantica, T. Hellsten, et al. Ion cyclotron range of frequency mode conversion flow drive in D(^{3}He) plasmas on JET. *Plasma Physics and Controlled Fusion*, 54(7):074001, 2012, Online.

[32] P. N. Yushmanov. *Reviews of plasma physics*, 16:117, 1990.

[33] K. Tani, T. Takizuka, and M. Azumi. Ripple loss of alpha particles in a tokamak reactor with a noncircular plasma cross-section. *Nuclear Fusion*, 33(6):903, 1993, Online.

[34] R. J. Goldston and H. H. Towner. Effects of toroidal field ripple on suprathermal ions in tokamak plasmas. *Journal of Plasma Physics*, 26(02):283–307, 1981, Online.

[35] R. J. Goldston, R. B. White, and A. H. Boozer. Confinement of high-energy trapped particles in tokamaks. *Phys. Rev. Lett.*, 47:647–649, Aug 1981, Online.

[36] K. C. Shaing. Magnetohydrodynamic-activity-induced toroidal momentum dissipation in collisionless regimes in tokamaks. *Physics of Plasmas*, 10(5):1443–1448, 2003, Online.

[37] K. C. Shaing, M. S. Chu, and S. A. Sabbagh. Eulerian approach to bounce/transit and drift resonance and neoclassical toroidal plasma viscosity in tokamaks. *Plasma Physics and Controlled Fusion*, 51(7):075015, 2009, Online.

[38] K. C. Shaing, S. A. Sabbagh, and M. S. Chu. Neoclassical toroidal plasma viscosity in the superbanana plateau regime for tokamaks. *Plasma Physics and Controlled Fusion*, 51(3):035009, 2009, Online.

[39] K. C. Shaing, S. A. Sabbagh, and M. S. Chu. Neoclassical toroidal plasma viscosity in the superbanana regime in tokamaks. *Plasma Physics and Controlled Fusion*, 51(5):055003, 2009, Online.

[40] Y. Sun, Y. Liang, K. C. Shaing, et al. Neoclassical toroidal plasma viscosity torque in collisionless regimes in tokamaks. *Phys. Rev. Lett.*, 105:7145002, Oct 2010, Online.

[41] A. J. Cole, J. D. Callen, W. M. Solomon, et al. Peak neoclassical toroidal viscosity at low toroidal rotation in the DIII-D tokamak. *Physics of Plasmas*, 18(5):055711, 2011, Online.

[42] A. Romannikov, C. Bourdelle, J. Bucalossi, et al. Measurement of central toroidal rotation in ohmic Tore Supra plasmas. *Nuclear Fusion*, 40(3):319–324, Mar 2000, Online.

[43] V. Basiuk, Y. Peysson, M. Lipa, et al. Studies of suprathermal electron loss in the magnetic ripple of Tore Supra. *Nuclear Fusion*, 41(5):477, 2001, Online.

[44] F. L. Hinton and J. A. Robertson. Neoclassical dielectric property of a tokamak plasma. *Physics of Fluids*, 27(5):1243–1247, 1984. doi: 10.1063/1.864478, Online.

[45] R. C. Morris, M. G. Haines, and R. J. Hastie. The neoclassical theory of poloidal flow damping in a tokamak. *Physics of Plasmas*, 3(12):4513–4520, 1996, Online.

[46] C. T. Hsu, K. C. Shaing, and R. Gormley. Time dependent parallel viscosity and relaxation rate of poloidal rotation in the banana regime. *Physics of Plasmas*, 1(1): 132–138, 1994, Online.

[47] S. P. Hirshman. The ambipolarity paradox in toroidal diffusion, revisited. *Nuclear Fusion*, 18(7):917, 1978, Online.

[48] K. C. Shaing and S. P. Hirshman. Relaxation rate of poloidal rotation in the banana regime in tokamaks. *Physics of Fluids B: Plasma Physics*, 1(3):705–707, 1989, Online.

[49] K. Nagashima, Y. Koide, and H. Shirai. Experimental determination of non-diffusive toroidal momentum flux in JT-60U. *Nuclear Fusion*, 34(3):449, 1994, Online.

[50] K. Ida, Y. Miura, T. Matsuda, et al. Evidence for a toroidal-momentum-transport nondiffusive term from the JFT-2M tokamak. *Phys. Rev. Lett.*, 74:1990–1993, Mar 1995, Online.

[51] M. Yoshida, Y. Koide, H. Takenaga, et al. Momentum transport and plasma rotation profile in toroidal direction in JT60-U L-mode plasmas. *Nuclear Fusion*, 47(8):856, 2007, Online.

[52] T. Tala, K.-D. Zastrow, J. Ferreira, et al. Evidence of inward toroidal momentum convection in the JET tokamak. *Phys. Rev. Lett.*, 102:075001, Feb 2009, Online.

[53] W. M. Solomon, K. H. Burrell, A. M. Garofalo, et al. Advances in understanding the generation and evolution of the toroidal rotation profile on DIII-D. *Nuclear Fusion*, 49(8):085005, 2009, Online.

[54] S. M. Kaye, W. Solomon, R. E. Bell, et al. Momentum transport in electron-dominated NSTX spherical torus plasmas. *Nuclear Fusion*, 49(4):045010, 2009, Online.

[55] A. G. Peeters, C. Angioni, and D. Strintzi. Toroidal momentum pinch velocity due to the coriolis drift effect on small scale instabilities in a toroidal plasma. *Phys. Rev. Lett.*, 98:265003, Jun 2007, Online.

[56] A. G. Peeters, C. Angioni, A. Bortolon, et al. Overview of toroidal momentum transport. *Nuclear Fusion*, 51(9):094027, 2011, Online.

[57] T. S. Hahm, P. H. Diamond, O. D. Gurcan, and G. Rewoldt. Nonlinear gyrokinetic theory of toroidal momentum pinch. *Physics of Plasmas*, 14(7):072302, 2007, Online.

[58] P. H. Diamond, C. J. McDevitt, Ö. D. Gürcan, T. S. Hahm, and V. Naulin. Transport of parallel momentum by collisionless drift wave turbulence. *Physics of Plasmas*, 15(1):012303, 2008, Online.

[59] J. S. deGrassie. Tokamak rotation sources, transport and sinks. *Plasma Physics and Controlled Fusion*, 51(12):124047, 2009, Online.

[60] K.-D. Zastrow, W. G. F. Core, L.-G. Eriksson, et al. Transfer rates of toroidal angular momentum during neutral beam injection. *Nuclear Fusion*, 38(2):257, 1998, Online.

[61] S. D. Scott, P. H. Diamond, R. J. Fonck, et al. Local measurements of correlated momentum and heat transport in the TFTR tokamak. *Phys. Rev. Lett.*, 64:531–534, Jan 1990, Online.

[62] J. S. deGrassie, D. R. Baker, K. H. Burrell, et al. Toroidal rotation in neutral beam heated discharges in DIII-D. *Nuclear Fusion*, 43(2):142, 2003, Online.

[63] P.C. de Vries, M.-D. Hua, D.C. McDonald, et al. Scaling of rotation and momentum confinement in JET plasmas. *Nuclear Fusion*, 48(6):065006, 2008, Online.

[64] J. Weiland, A. Eriksson, H. Nordman, and A. Zagorodny. Progress on anomalous transport in tokamaks, drift waves and nonlinear structures. *Plasma Physics and Controlled Fusion*, 49(5A):A45, 2007, Online.

[65] N. Mattor and P. H. Diamond. Momentum and thermal transport in neutral-beam-heated tokamaks. *Physics of Fluids*, 31(5):1180–1189, 1988, Online.

[66] J. E. Rice, A. Ince-Cushman, J. S. deGrassie, et al. Inter-machine comparison of intrinsic toroidal rotation in tokamaks. *Nuclear Fusion*, 47(11):1618, 2007, Online.

[67] P. Mantica, T. Tala, J. S. Ferreira, et al. Perturbative studies of toroidal momentum transport using neutral beam injection modulation in the Joint European Torus: Experimental results, analysis methodology, and first principles modeling. *Physics of Plasmas*, 17(9):092505, 2010, Online.

[68] G. Tardini, A. G. Peeters, G. V. Pereverzev, F. Ryter, and the ASDEX Upgrade Team. Theory-based modelling of ASDEX Upgrade discharges with ECH modulation. *Nuclear Fusion*, 42(7):L11, 2002, Online.

[69] G. Tardini, J. Ferreira, P. Mantica, et al. Angular momentum studies with NBI modulation in JET. *Nuclear Fusion*, 49(8):085010, 2009, Online.

[70] F. Ryter, C. Angioni, C. Giroud, et al. Simultaneous analysis of ion and electron heat transport by power modulation in JET. *Nuclear Fusion*, 51(11):113016, 2011, Online.

[71] F. Ryter, C. Angioni, A. G. Peeters, et al. Experimental study of trapped-electron-mode properties in tokamaks: Threshold and stabilization by collisions. *Phys. Rev. Lett.*, 95:085001, Aug 2005, Online.

[72] F. X. Söldner, K. McCormick, D. Eckhartt, et al. Suppression of sawtooth oscillations by lower-hybrid current drive in the ASDEX tokamak. *Phys. Rev. Lett.*, 57: 1137–1140, Sep 1986, Online.

[73] D. J. Campbell, D. F. H. Start, J. A. Wesson, et al. Stabilization of sawteeth with additional heating in the JET tokamak. *Phys. Rev. Lett.*, 60:2148–2151, May 1988, Online.

[74] C. R. Negus, C. Giroud, A. G. Meigs, et al. Enhanced core charge exchange recombination spectroscopy system on Joint European Torus. *Review of Scientific Instruments*, 77(10):10F102, 2006, Online.

[75] J. A. Heikkinen and S. K. Sipilä. Power transfer and current generation of fast ions with large-k_θ waves in tokamak plasmas. *Physics of Plasmas*, 2(10):3724–3733, 1995, Online.

[76] J. A. Heikkinen, W. Herrmann, and T. K. Kurki-Suonio. Fast response in the ripple trapped ion distribution to abrupt changes in a radial electric field in tokamaks. *Nuclear Fusion*, 38(3):419, 1998, Online.

[77] T. Johnson, A. Salmi, G. Steinbrecher, et al. Library for RF interactions in orbit following codes. *AIP Conference Proceedings*, 1406(1):373–376, 2011, Online.

[78] K. Shinohara, T. Kurki-Suonio, D. Spong, et al. Effects of complex symmetry-breakings on alpha particle power loads on first wall structures and equilibrium in ITER. *Nuclear Fusion*, 51(6):063028, 2011, Online.

[79] T. Kurki-Suonio, O. Asunta, E. Hirvijoki, et al. Fast ion power loads on ITER first wall structures in the presence of NTMs and microturbulence. *Nuclear Fusion*, 51 (8):083041, 2011, Online.

[80] M. García-Muñoz, P. Martin, H.-U. Fahrbach, et al. NTM induced fast ion losses in ASDEX Upgrade. *Nuclear Fusion*, 47(7):L10, 2007, Online.

[81] G. Park, C. S. Chang, I. Joseph, and R. A. Moyer. Plasma transport in stochastic magnetic field caused by vacuum resonant magnetic perturbations at diverted tokamak edge. *Physics of Plasmas*, 17(10):102503, 2010, Online.

[82] Y. Sun, Y. Liang, H. R. Koslowski, et al. Toroidal rotation braking with n = 1 magnetic perturbation field on JET. *Plasma Physics and Controlled Fusion*, 52 (10):105007, 2010, Online.

[83] Y. Liang, H. R. Koslowski, P. R. Thomas, et al. Active control of type-I edge-localized modes with $n = 1$ perturbation fields in the JET tokamak. *Phys. Rev. Lett.*, 98: 265004, Jun 2007, Online.

[84] S. K. Sipilä. *ASCOT: accelerated simulation of charged particle orbits in a Tokamak*. TKK, PhD Thesis, Espoo, 1992. ISBN 951-22-1137-8.

[85] V. Hynönen. *Orbit-following simulation of fast ions in ASDEX upgrade tokamak in the presence of magnetic ripple and radial electric field*. Helsinki University of Technology, PhD Thesis, Espoo, 2008. ISBN 978-951-22-9459-6, Online.

[86] G. Genacchi and A. Taroni. JETTO: a free boundary plasma transport code (basic version). *Rapporto ENEA RT/TIB*, 1988.

[87] L. L. Lao, J. R. Ferron, R. J. Groebner, et al. Equilibrium analysis of current profiles in tokamaks. *Nuclear Fusion*, 30(6):1035, 1990, Online.

[88] L.-G. Eriksson and M. Schneider. Monte Carlo operators for ions interacting with radio frequency waves. *Physics of Plasmas*, 12(7):072524, 2005, Online.

[89] P. Strand, I. C. Plasencia, B. Guillerminet, et al. A european infrastructure for fusion simulations. In *Parallel, Distributed and Network-Based Processing (PDP), 2010 18th Euromicro International Conference on*, pages 460–467, Feb 2010, Online.

[90] L.-G. Eriksson, T. Hellsten, and U. Willen. Comparison of time dependent simulations with experiments in ion cyclotron heated plasmas. *Nuclear Fusion*, 33(7): 1037, 1993, Online.

[91] L.-G. Eriksson and T. Hellsten. A model for calculating ICRH power deposition and velocity distribution. *Physica Scripta*, 52(1):70, 1995, Online.

[92] J. Carlsson, L.-G. Eriksson, and T. Hellsten. FIDO, a code for calculating the velocity distribution function of a toroidal plasma during ICRH. In *Theory of Fusion Plasmas*, page 351, Varenna, 1994. Joint Varenna-Lausanne International Workshop, Societá Italiana di Fisica.

[93] L.-G. Eriksson, M. J. Mantsinen, V. P. Bhatnagar, et al. Theoretical analysis of ICRF heating in JET DT plasmas. *Nuclear Fusion*, 39(3):337, 1999, Online.

[94] M. J. Mantsinen, O. N. Jarvis, V. G. Kiptily, et al. First observation of pT fusion in JET tritium plasmas with ICRF heating of protons. *Nuclear Fusion*, 41(12):1815, 2001, Online.

[95] L.-G. Eriksson and P. Helander. Monte Carlo operators for orbit-averaged Fokker–Planck equations. *Physics of Plasmas*, 1(2):308–314, 1994, Online.

[96] L.-G. Eriksson, M. J. Mantsinen, T. Hellsten, and J. Carlsson. On the orbit-averaged Monte Carlo operator describing ion cyclotron resonance frequency wave–particle interaction in a tokamak. *Physics of Plasmas*, 6(2):513–518, 1999, Online.

[97] A. A. Korotkov, A. Gondhalekar, and A. J. Stuart. Impurity induced neutralization of megaelectronvolt energy protons in JET plasmas. *Nuclear Fusion*, 37(1):35, 1997, Online.

[98] L.-G. Eriksson, M. J. Mantsinen, F. G. Rimini, et al. ICRF heating of JET plasmas with the third harmonic deuterium resonance. *Nuclear Fusion*, 38(2):265, 1998, Online.

[99] C. D. Challis, J. G. Cordey, H. Hamnén, et al. Non-inductively driven currents in JET. *Nuclear Fusion*, 29(4):563, 1989, Online.

[100] G. Saibene, R. Sartori, P. de Vries, et al. Toroidal field ripple effects on H-modes in JET and implications for ITER. *Proc. 34th EPS Conf. on Plasma Physics Controlled Fusion (Warsaw, Poland, 2007)*, Online.

[101] K. Tobita, K. Tani, Y. Neyatani, et al. Ripple-trapped loss of neutral-beam-injected fast ions in JT-60U. *Phys. Rev. Lett.*, 69:3060–3063, Nov 1992, Online.

[102] T. Johnson, J. Lönnroth, P.C. de Vries, et al. HALEKAR modelling of fast particle transport and losses with TF ripple in JET. In *10th IAEA Technical Meeting on Energetic Particles in Magnetic Confinement Systems*.

[103] H. Biglari, P. H. Diamond, and P. W. Terry. Influence of sheared poloidal rotation on edge turbulence. *Physics of Fluids B: Plasma Physics*, 2(1):1–4, 1990, Online.

[104] R. J. Goldston, D. C. McCune, H. H. Towner, et al. New techniques for calculating heat and particle source rates due to neutral beam injection in axisymmetric tokamaks. *Journal of Computational Physics*, 43(1):61–78, 1981, Online.

[105] A.G. Peeters, Y. Camenen, F.J. Casson, et al. The nonlinear gyro-kinetic flux tube code GKW. *Computer Physics Communications*, 180(12):2650 – 2672, 2009. ISSN 0010-4655, Online.

[106] M. A. Kotschenreuther, G. B. Rewoldt, and W. M. B. Tang. Comparison of initial value and eigenvalue codes for kinetic toroidal plasma instabilities. *Computer Physics Communications*, 88(2-3):128–140, 1995, Online.

[107] A. G. Peeters, C. Angioni, A. Bottino, et al. Toroidal momentum transport. *Plasma Physics and Controlled Fusion*, 48(12B):B413, 2006, Online.

[108] J. E. Kinsey, R. E. Waltz, and J. Candy. Nonlinear gyrokinetic turbulence simulations of E x B shear quenching of transport. *Physics of Plasmas*, 12(6):062302, 2005, Online.

[109] D. Strintzi, A. G. Peeters, and J. Weiland. The toroidal momentum diffusivity in a tokamak plasma: A comparison of fluid and kinetic calculations. *Physics of Plasmas*, 15(4):044502, 2008, Online.

[110] A. G. Peeters, C. Angioni, and ASDEX Upgrade Team. Linear gyrokinetic calculations of toroidal momentum transport in a tokamak due to the ion temperature gradient mode. *Physics of Plasmas*, 12(7):072515, 2005, Online.

[111] R. J. Hawryluk, D. J. Campbell, G. Janeschitz, et al. Principal physics developments evaluated in the ITER design review. *Nuclear Fusion*, 49(6):065012, 2009, Online.

[112] A. Portone, M. Roccella, R. Roccella, F. Lucca, and G. Ramogida. The ITER TF coil ripple: Evaluation of ripple attenuation using Fe insert and of ripple enhancement produced by TBM. *Fusion Engineering and Design*, 83(10-12):1619–1624, 2008. ISSN 0920-3796, Online. Proceedings of the Eight International Symposium of Fusion Nuclear Technology, ISFNT-8 SI.

[113] H. Kawashima, M. Sato, K. Tsuzuki, et al. Demonstration of ripple reduction by ferritic steel board insertion in JFT-2M. *Nuclear Fusion*, 41(3):257, 2001, Online.

[114] K. Shinohara, H. Kawashima, K. Tsuzuki, et al. Effects of complex magnetic ripple on fast ions in JFT-2M ferritic insert experiments. *Nuclear Fusion*, 43(7):586, 2003, Online.

[115] K. Shinohara, S. Sakurai, M. Ishikawa, et al. Ferritic insertion for reduction of toroidal magnetic field ripple on JT-60U. *Nuclear Fusion*, 47(8):997, 2007, Online.

PUBLICATION I

JET experiments to assess the clamping of the fast ion energy distribution during ICRF heating due to finite Larmor radius effects

In: Plasma Physics and Controlled Fusion 48,
pp. 717–726, 2006.

http://iopscience.iop.org/0741-3335/48/6/001/pdf/0741-3335_48_6_001.pdf

INSTITUTE OF PHYSICS PUBLISHING PLASMA PHYSICS AND CONTROLLED FUSION

Plasma Phys. Control. Fusion **48** (2006) 717–726 doi:10.1088/0741-3335/48/6/001

JET experiments to assess the clamping of the fast ion energy distribution during ICRF heating due to finite Larmor radius effects

A Salmi[1], M J Mantsinen[1], P Beaumont[2], P de Vries[2], L-G Eriksson[3], C Gowers[2], P Helander[2], M Laxåback[4], J-M Noterdaeme[5,6], D Testa[7] and EFDA JET contributors[8]

[1] Helsinki University of Technology, Association Euratom-Tekes, Finland
[2] Euratom/UKAEA Fusion Association, Culham Science Centre, Abingdon, UK
[3] Association EURATOM-CEA, CEA/DSM/DRFC, CEA-Cadarache, St. Paul lez Durance, France
[4] Alfvén Laboratory, Association Euratom-VR, Stockholm, Sweden
[5] Max-Planck IPP-EURATOM Assoziation, Garching, Germany
[6] Gent University, Belgium
[7] CRPP, Association Euratom-Confédération Suisse, EFPL, Lausanne, Switzerland

Received 17 January 2006, in final form 14 March 2006
Published 24 April 2006
Online at stacks.iop.org/PPCF/48/717

Abstract

Experiments have been performed on the JET tokamak with 2nd harmonic ion cyclotron resonance heating (ICRH) of hydrogen in deuterium plasmas to assess the role of finite Larmor radius (FLR) effects on the resonant ion distribution function. More specifically, the clamping of high-energy resonant particle distribution due to weak wave-particle interaction at high energy is studied. The distributions of ICRH heated hydrogen ions have been measured with a high-energy neutral particle analyser in the range of 0.29–1.1 MeV. By changing the electron density the energy E^*, around which the wave-particle interaction becomes weak, is varied. The dependence of the ion distribution on E^* is experimentally observed for a number of discharges and FLR effects are clearly seen to affect the high energy tail shape. Experiments have been analysed with the combination of ICRH modelling codes PION and FIDO, including FLR effects, and good agreement with measurements have been found.

(Some figures in this article are in colour only in the electronic version)

1. Introduction

One of the principal ICRF heating schemes foreseen for ITER is the second harmonic heating of tritium, $\omega \approx 2\omega_{cT}$. For this heating scheme, as for other harmonic ICRF schemes with

[8] See annex of J Pamela *et al* 2002 *Proc. 19th Int. Conf. on Fusion Energy 2002 (Lyon, France, 2002)* (Vienna: IAEA).

0741-3335/06/060717+10$30.00

$\omega \approx n\omega_{ci}$ and $n > 1$, the absorption of wave power at the ion cyclotron resonance is a finite Larmor radius effect. Consequently, the wave absorption by the resonating ions is weak at low energies but increases strongly as the ratio of the ion Larmor radius, $\rho = v_\perp/\omega_{ci}$, to the perpendicular wavelength of the fast wave increases. Here, $v_\perp$ is the ion velocity component in the direction perpendicular to the background magnetic field. However, when the ion Larmor radius further increases (corresponding typically to mega electron volt range) the absorption weakens again and effectively prevents particles from reaching higher velocities. To predict with confidence the performance of the second harmonic heating of tritium, as well as to estimate the consequences of ICRH heated fast particles on plasma stability and on some diagnostics in ITER, it is important to have a good understanding of the resonant ion energy distribution. The information on the fast ion energy content or mean energy is not enough in all cases. Therefore, detailed investigations of second and higher-harmonic scenarios and, in particular, of finite Larmor radius effects, are required in present-day tokamaks. In this paper, we will present results from the JET tokamak that demonstrate the important role of finite Larmor radius (FLR) effects on the high-energy part of the ICRF-driven ion distribution.

It is not trivial to define experimental conditions to test in detail the role of the finite Larmor radius effects during ICRF heating. Naturally, the creation of a fast ion population when ICRF power is applied at a harmonic of the ion cyclotron frequency is itself a manifestation of the finite Larmor radius effects. However, there is seldom enough experimental data to draw conclusions on the exact nature of the ICRF absorption process including the influence of finite Larmor radius effects. Essential for this sort of study are the good confinement of the energetic ions as well as an accurate means of measuring their energy distribution at high energies.

The experiments reported in this paper continue an earlier work [1] on the JET tokamak where it was found that for the second harmonic heating the number of particles at high-energy part of the distribution decreases strongly when the ion energy reaches E^*, the expected location for weak wave-particle interaction. By comparing the measured energy distributions between fundamental and second harmonic heating scenarios, the rapid fall-off seen in the distribution for the second harmonic case could be attributed to FLR effects. This was an important experimental result because it showed that the FLR effects can influence the distribution function of the resonating ions. Furthermore, it indicated the possibility of assessing directly the importance of finite Larmor radius effects during high-harmonic ICRF heating by measuring the ion distribution function for different E^*, as has been done in the experiments reported in this paper.

This paper is organized as follows. In section 2, we discuss the ICRF physics relevant for the present experiments and discuss the interplay between the distribution function and the RF diffusion coefficient. In section 3, the experimental set-up and measurements are presented and in section 4, computer simulations which take FLR effects into account are compared with the experimental measurements. Section 5 concentrates on discussing certain issues that remain, for instance, the possibility of the existence of an adiabatic barrier. Finally in section 6 follows the summary.

2. Relevant ICRF physics

The distribution function f for the ICRF resonant ions can be derived using the quasi-linear Fokker–Planck equation:

$$\frac{\partial f}{\partial t} = \hat{C}(f) + \hat{Q}(f),$$

where $\hat{C}$ is a collision operator and $\hat{Q}$ is a quasi-linear RF diffusion operator. In order to gain insight into the details of the perpendicular fast ion distribution, we use this equation in a simplified form:

$$\frac{\partial f\,(v_\perp, t)}{\partial t} \approx \frac{1}{v_\perp}\frac{\partial}{\partial v_\perp}\left[-\alpha v_\perp f + \frac{1}{2}\frac{\partial}{\partial v_\perp}(\beta v_\perp f) + \frac{1}{4}\gamma f + D_{\mathrm{RF}} v_\perp \frac{\partial f}{\partial v_\perp}\right]. \tag{1}$$

The equation is the same as in [2] with the exception that the RF diffusion coefficient, here denoted with D_{RF}, is not an expansion but fully includes finite orbit effects and is thus suitable for this work where the 2nd harmonic heating is studied. Here $f(v_\perp) = f(v)\mathrm{d}v_{||}$ and α, β and γ are the Spitzer collision coefficients [3] and D_{RF} is given by

$$D_{\mathrm{RF}} = K\left|J_{n-1}\left(\frac{k_\perp v_\perp}{\omega_{ci}}\right) + \frac{E_-}{E_+}\mathrm{J_{n+1}}\left(\frac{k_\perp v_\perp}{\omega_{ci}}\right)\right|^2, \tag{2}$$

where J_n denotes the nth order of Bessel function of the first kind, n is the number of the cyclotron harmonic, K is a constant proportional to the square of the co-rotating electric field E_+ and $k_\perp$ and ω_{ci} are the perpendicular wave number and the ion cyclotron frequency, respectively. Note, that in deriving of equation (1) it has been assumed [2] that $\mathrm{v}_\perp >> v_{||}$ and $\mathrm{v} >> v_{\mathrm{th}}$. In simulations we found that the kinetic energy content in the perpendicular component of fast ions is typically 8–10 times higher than the energy in the parallel component, thereby increasing the confidence in these approximations.

The steady-state solution for a test particle distribution is readily solved from equation (1) by integration and yields

$$f\,(v_\perp) \approx f_0 \exp\left(-\int_0^{v_\perp} \mathrm{d}v_\perp \frac{-4\alpha v_\perp + 2\,(\beta v_\perp)' + \gamma}{2\beta v_\perp + 4 D_{\mathrm{RF}} v_\perp}\right). \tag{3}$$

The above equation is the same as in [2] except for the term D_{RF} which we have kept here unexpanded. To achieve our aim it is not necessary to simplify the equation further. We only wish to point out that except close to the local minima of D_{RF} the term "$4D_{\mathrm{RF}}\ v_\perp$" is large compared with all other terms in the integrand for a wide parameter range (applies when $\mathrm{v} >> v_{\mathrm{th}}$). In fact, if "$4D_{\mathrm{RF}}\ v_\perp$" were small no fast tail would be able to develop in the first place. After realising this, the qualitative behaviour of the distribution function, as shown in the subsequent figures, is easy to see; when the dominating term D_{RF} is large the integrand is small and therefore the distribution stays flat, whereas when D_{RF} is small the integrand is large and the distribution drops quickly.

Figure 1(*a*) shows D_{RF} for the fundamental (full line) and the second harmonic resonance heating (dash-dotted line) where FLR effects are included. In comparison, also an imaginary case where D_{RF} is set to a constant is shown (dashed line). In figure 1(*b*) the corresponding distributions are plotted. The simple arguments given above are seen to be valid as the distribution functions behave as expected. In practise, if the first minimum of D_{RF} in the plasma is small and wide enough then practically no particles can get accelerated beyond energy E^* (the energy where D_{RF} has its first minimum). Note that the power levels for the different scenarios in figure 1 are not equal. The purpose of the figure is to illustrate the drops in the distributions due to the weak wave-particle interaction regions.

Figures 1(*a*) and (*b*) also demonstrate that shortly before E^* value distributions already start to clamp because the available power is not enough to compensate the slowing down of the ions. The figures make obvious why the second harmonic heating scheme was chosen for the experiments: E^* value for the fundamental heating is typically at too high energies That is, either the particles experience orbit losses before reaching E^* or the available diagnostics capabilities on JET will not allow accurate measurements around E^* for fundamental heating.

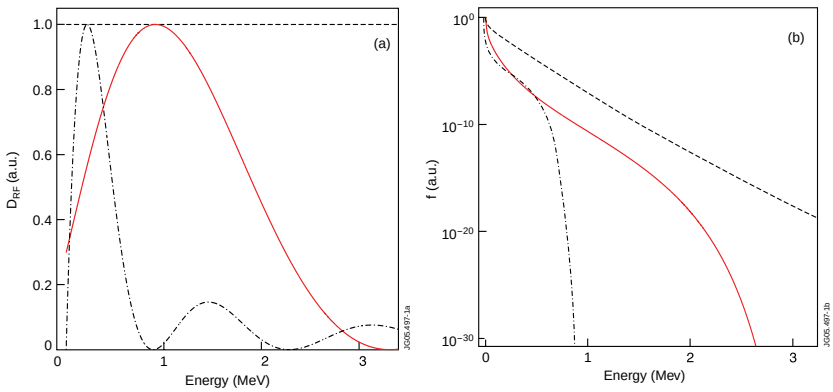

Figure 1. (*a*) Quasi linear RF diffusion coefficient for the fundamental (–) and second (–·) harmonic ICRF heating. The dashed line (- -) shows a fictitious case where D_{RF} is constant and (*b*) the corresponding energy distributions calculated from equation (3).

For ICRF heating of minority ion species the ratio E_-/E_+ stays almost constant as the electron density is varied. Consequently, in these cases the location of the first minimum of D_{RF} depends only on the argument of the Bessel functions, see equation (2). Writing $\alpha^* = k_\perp v_\perp^*/\omega_{ci}$, where α^* is the argument at the minimum and solving for E^* we get an approximate scaling, $E^* \propto B^2/n_e$. Here, it was assumed that $\omega_{\mathrm{ci}} \propto B$ and that $k_\perp \propto \sqrt{n_e}$ by cold plasma theory.

To show how electron density affects the distribution and its shape we have plotted three resonant particle energy distributions in figure 2 using parameters that are typical for the experiments performed. That is, second harmonic hydrogen minority heating in a deuterium plasma with an electron density of $3 \cdot 10^{19}\mathrm{m}^{-3}$ using dipole phasing of the JET ICRF antennas having the maximum power at $|k_{||}| = 8\mathrm{m}^{-1}$ and a frequency of 51 MHz. The broken lines symbolize cases where electron densities were varied keeping otherwise identical plasma parameters. PION code [4, 5] was used to quantify the changes in the perpendicular wave number and in the polarization of the wave due to density changes. The graph shows that a 10% change in the density results in a significant, and measurable, change in the distribution. We can now see that from the experimental point of view a convenient way of assessing the importance of FLR effects is to vary electron density (and thus E^*) and see how well the distribution responds to it.

So far we have only considered monochromatic heating, i.e. a fast wave with a single wave number $\mathrm{k}_\perp$. Of course, in reality a wave emitted from a finite antenna has a wave number spectrum. Having a $\mathrm{k}_\perp$-spectrum means that the effective D_{RF} becomes an average over different $\mathrm{k}_\perp$ and consequently $D_{\mathrm{RF}}(E^*)$ is not zero but has a finite value. It is not, however, feasible to incorporate all the necessary corrections due to the wave number spectrum or the effect of, e.g. non-constant plasma profiles, Doppler shift, non-Maxwellian particle distribution or orbit effects into the analytical equation. To do this, numerical simulations are required. Later, in section 4 we will show simulation results where these effects are taken into account.

Thus from previous considerations we can expect that the distribution drops rapidly in cases where the RF diffusion coefficient in the plasma has a pronounced first maximum and first minimum similar to those shown in figures 1 and 2. Now taking a completely opposite

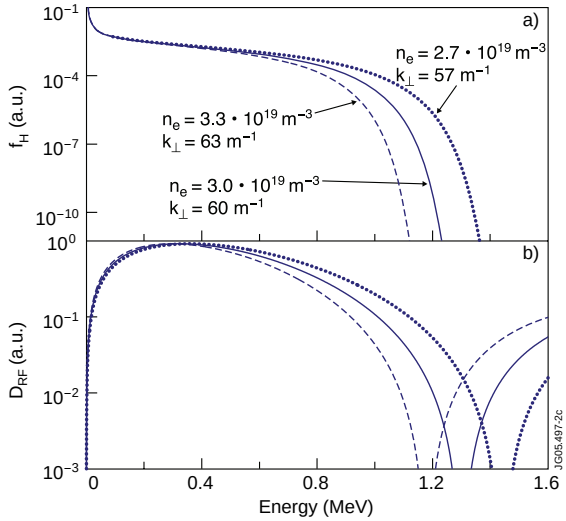

Figure 2. (*a*) Steady-state energy distribution functions of hydrogen with second-harmonic minority heating scenario, (2H)D and (*b*) the corresponding RF diffusion coefficients. Full lines are with ICR frequency $f = 51.25\,\mathrm{MHz}$, electron temperature $T_e = 4.5\,\mathrm{keV}$, ion temperature $T_i = 2.5\,\mathrm{keV}$, electron density $n_e = 3 \times 10^{19}\,\mathrm{m}^{-3}$ and perpendicular wave number $k_\perp = 60\,\mathrm{m}^{-1}$. Broken lines correspond to a situation where $k_\perp$ is altered by changing electron density by 10%.

point of view: if, for some reason, there were effects that would average out the RF diffusion coefficient to the extent that it could be approximated with a constant, the behaviour of the distribution would be markedly different. In that case the solution for equation (3) would have a nearly exponential form, $f \approx f_0 \exp(-E_\perp / T_{\mathrm{eff}})$, where $T_{\mathrm{eff}} \propto p_\perp T_e^{3/2} / n_r n_e$ (see [2] and figure 1). Here $p_\perp$ is the flux surface averaged power density absorbed by resonant species, n_r is the density of the resonant ions and T_e and n_e are the temperature and density of the electrons, respectively. Hence, in the limit of the constant D_{RF}, local ion tail temperature would increase with increasing power and electron temperature and decrease with increasing ion and electron density. As we will soon see this is not a good approximation and as it is well known Stix T_{eff} approximation for fundamental heating [2] should not be used for second and higher harmonic heating cases.

For completeness we mention here two additional effects which we have not yet discussed but which deserve some attention. The first one is the sawtooth oscillations that were also present in the experiments reported in this paper. Many studies have shown that sawtooth oscillations redistribute energetic ions inside the sawtooth inversion radius, see for example a recent review in [6]. They are known to have the most pronounced effect on particles which are closely tied to a flux surface and thus feel the reconnection process. Secondly, redistribution favours particles that do not have too small ratio of $v_{||}/v_\perp$. This means that sawteeth are not expected to play a major role for the highly energetic ICRH accelerated particles both having a small $v_{||}/v_\perp$ ratio and broad banana orbits.

Secondly, what needs to be discussed is the so-called super-adiabatic motion [7,8] of ions. Super-adiabatic motion happens when the relative phase between the wave and the Larmor motion of the resonating ion is not sufficiently perturbed as required for true diffusion. When

the phases become correlated ICRH no longer heats the particles which remain oscillating in phase space islands. Stochasticity of the phase results usually from particle collisions or from the non-linear interaction between the wave and particles. Normally, at energies in megaelectronvolt range, collisions are not sufficient for randomizing the phase and when in addition the wave-particle interaction becomes weak, as it does close to E^*, the phase of the ion Larmor motion remains correlated with the wave, phase space islands are formed and particles are not heated to higher temperatures. For now we will disregard this effect, but we will return to it again in the discussion elsewhere in the paper.

3. Experimental results

The experiments reported here were designed and carried out on the JET tokamak to verify whether the details in the ICRH diffusion coefficient (i.e. FLR effects) have an effect on the high energy part of the resonant ion energy distribution or whether the distribution functions qualitatively obey the simple relation $T_{\mathrm{eff}} \propto \mathrm{p}_\perp\ T_{\mathrm{e}}^{3/2}/n_{\mathrm{r}}n_{\mathrm{e}}$ as discussed in section 2. The scenario chosen for the experiments is second harmonic hydrogen minority heating in L-mode deuterium plasma, (2H)D. This scenario is favourable because it allows E^* to be easily adjusted, by varying the plasma density, to be in the measurement window of the high-energy neutral particle analyser (NPA) [9] which was used to measure the high-energy ion distribution functions.

The eight energy channels of the NPA were set to measure the proton flux in the range of 0.29–1.1 MeV. The NPA has a vertical line-of-sight at major radius 3.07 m, i.e. less than 10 cm to the low field side of the magnetic axis, and thus enables the deduction of the line integrated distribution function of fast ions close to the centre of the plasma. The magnetic field in the experiment was 1.65 T, the plasma current 1.65 MA and the electron density was varied in the range 2.8×10^{19}–$4.4 \times 10^{19}\ \mathrm{m}^{-3}$. Externally only ICRH (3–5 MW) was used for plasma heating. IC waves were launched with four JET A2 antennas applied with a frequency of 51.25 MHz using dipole phasing (toroidal mode number at the maximum of the antenna power spectrum was $|\mathrm{N}| \approx 26$). In this configuration, the second harmonic hydrogen minority resonance locates close to the centre of the plasma.

In figure 3, most relevant experimental parameters, ICRH power, neutral beam power (NBI), electron density and temperature at magnetic axis and plasma diamagnetic energy for the three discharges are shown. Short duration NBI pulses (blips) at 64.1 and 67.1 s were used to measure the ion density and temperature. Plasma parameters in these discharges were such that initially 58738 and 58739 had identical plasmas (also identical electron densities) but due to higher input power electron temperature and plasma energy become higher in 58739. The plasma and power levels for discharge 58734 were chosen so that the effective temperature, T_{eff}, is the same as in pulse 58738. The match was achieved by injecting more power in the high density pulse 58734. Table 1 highlights the relative differences for the most relevant parameters for these discharges.

The line integrated perpendicular energy distributions deduced from NPA measurements are shown in figure 4 for the three discharges of interest. From the comparison between discharges 58734 and 58738 one can see that the local tail temperature is significantly lower and the tail is shorter for the high electron density pulse 58734. At the same time T_{eff} is almost equal for both pulses and the location of the first minimum in D_{RF}, E^*, is about 30% smaller for the high density pulse 58734 (table 1). These results indicate that D_{RF} cannot be considered a constant. Otherwise both distributions should have the same shape and should not have a steep gradient region. Comparing table 1 and figure 4 we can see that E^* is reasonably accurate in estimating the energy at which the fast ion distribution rapidly decreases and effectively vanishes.

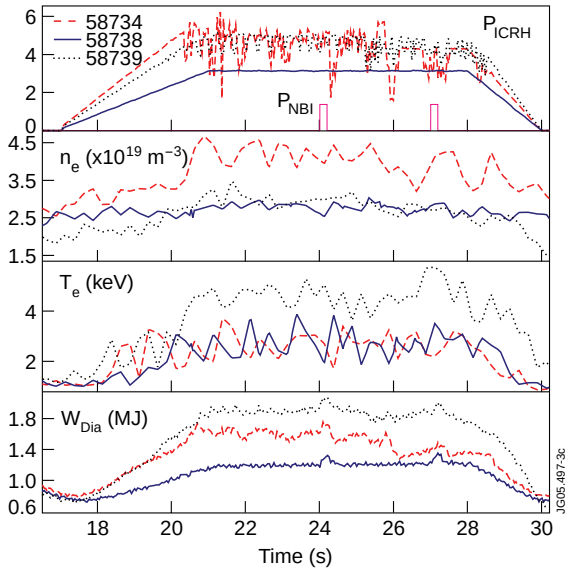

Figure 3. (*a*) ICRH and NBI power, (*b*) central electron density, (*c*) central electron temperature and (*d*) plasma diamagnetic energy. Charge exchange measurements from plasma centre at $t = 64.1$ s gave for the effective charge of ions $Z_{\rm eff} = 1.75$, 1.45 and 2.15 and for the ion temperature $T_{\rm i} = 1.2$, 1.2 and 2.25 keV for the pulses 58734, 58738 and 58739, respectively.

Table 1. The key parameters for the discharges. Values are normalised to those of discharge 58738 with an electron density $n_{\rm e}(0) = 2.8 \times 1019\,{\rm m}^{-3}$, power absorbed by hydrogen $\rm P_H = 2.9$ MW, central electron temperature $T_{\rm e}(0) = 3$ keV, hydrogen density $\rm n_H(0) = 1.3 \times 1018\,m^{-3}$, effective tail temperature $T_{\rm eff} = 1$ a.u. and E* = 1.37 MeV (E* has been evaluated in the plasma centre for |N| = 26, i.e. at the peak of the power spectrum).

Pulse	$\rm n_{e0}$	$\rm P_H$	$T_{\rm e0}$	$\rm n_{H0}$	$T_{\rm eff}$	$E*$
58734	1.5	1.2	1.0	0.9	0.92	0.7
58738	1.0	1.0	1.0	1.0	1.00	1.0
58739	1.0	1.2	1.7	1.0	2.38	1.0

The comparison between pulses 58738 and 58739 basically tells the same story from another viewpoint. This time the discharges have equal $E*$ but substantially different $T_{\rm eff}$. In this case if FLR effects were not important the discharge 58739 would have to have much higher local tail temperature (table 1). Experimental measurements, however, show identically shaped distributions (equal local temperatures) having the steeper gradient zones at the same place. Again, this provides clear evidence for the significance of FLR effects and rules out $D_{\rm RF}$ being a constant.

4. Comparison with modelling

For the modelling of the experiments ICRF codes PION [4] and FIDO [10] were used. PION is a simplified time-dependent Fokker-Planck code for calculating ICRF power deposition profiles

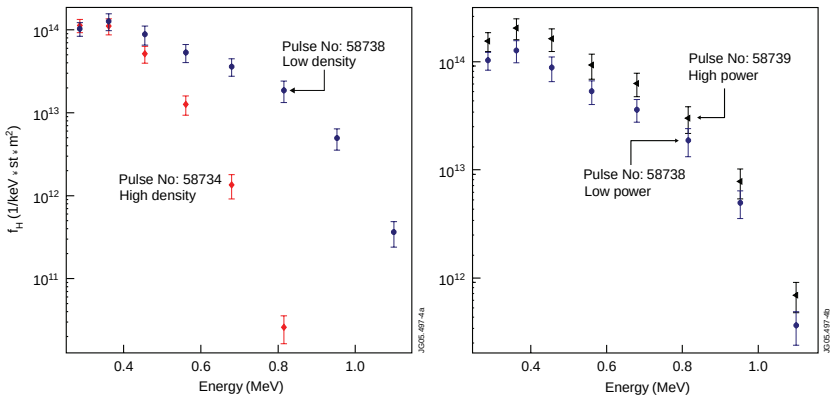

Figure 4. Experimental hydrogen energy distribution deduced from high-energy NPA measurements with error bars included.

and pitch-angle-averaged ion distribution functions self-consistently (i.e. ICRF power deposition and the resulting resonant ion distributions are consistent). We used PION here to estimate the power absorbed directly on hydrogen as well as to solve the perpendicular wave number spectrum $k_\perp$ and the polarization of the wave. This data together with measured plasma profiles were used as input for the 3D Monte Carlo code FIDO to solve the full energy distribution of the resonant particles. The wave number spectrum fed into FIDO consists of ten perpendicular wave numbers. FIDO is a sophisticated code and can take, for instance, FLR effects, orbit effects, radial pinch effects and plasma profile effects into account. However, it does not handle sawtooth activity or super-adiabaticity which is why their possible additional effects have to be dealt separately, see section 5. Other approaches for modelling this phenomenon could also be used. Possible choices include at least hot plasma theory, i.e. using a multi-harmonic asymptotic expansion of the wave-driven effective electric field that accelerates the ions [11].

The comparisons between the simulated distributions and the measured ones are shown in figure 5. Solid lines show the calculated perpendicular energy distributions where simulations have been done using the measured plasma parameters. Dashed lines are from simulations made with a 10% higher/lower electron density while keeping ion fractions and other parameters constant. The data clearly show that simulations are consistent with the measurements with rather good accuracy.

These simulations also confirm the sensitivity of the distribution to electron density as deduced from theory earlier. Since the uncertainty of measuring electron density at JET is normally 10%, we can take the regions between the dashed lines as an estimate for the uncertainty in modelling. Of course there are ambiguities also in other quantities such as in the excited $k_{||}$ spectrum or in the measured ones; ion densities and temperatures of different species, etc. However, as explained in the previous section the distribution is most sensitive to electron density variations which make this a sensible lower estimate for the total error. We can conclude that the uncertainties in measuring the plasma parameters alone could explain the differences. Unfortunately they also prevent one for making even more detailed comparisons between measurements and modelling and possibly finding out some minor details still missing from the simulations.

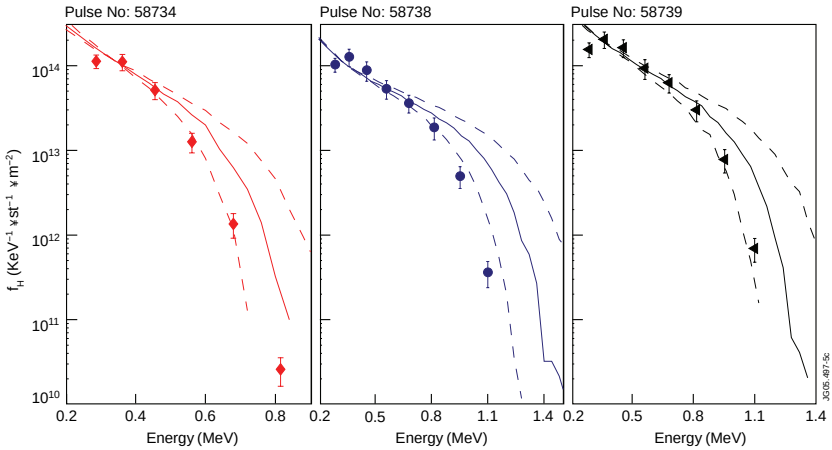

Figure 5. FIDO simulations of proton perpendicular energy distribution (lines) compared with NPA measurements (points with error bars). Dashed (–) lines reflect the uncertainty of modelling due to the uncertainty of plasma parameters.

5. Discussion

Earlier, in section 2, we briefly discussed sawtooth activity in relation to fast ion distribution function. It was anticipated that they would not have a large effect on the highly energetic particles due to the wide orbits of the particles and small $v_{||}/v_{\perp}$ ratio. This is also supported by experimental data when we compare the sawtooth frequencies of the discharges. They were approximately 6.5 Hz (58734), 7 Hz (58738) and 3.5 Hz (58739). Here, with about equal sawteeth frequencies, discharges 58734 and 58738 have markedly distinct spectra and with quite different frequencies; discharges 58738 and 58739 have similar spectra. Also, if the ion slowing down times of about 0.2 (58734), 0.2 (58738) and 0.4 s (58739) are taken into account we cannot find a trend that would explain the measured perpendicular energy distributions.

The possible effect of the super-adiabatic motion was studied with a STOCH [7] code for this ICRF heating scenario. The results indeed indicated the presence of an adiabatic barrier just at the location of E^* for a monochromatic wave. Weak wave-particle interaction close to E^* can only create minor perturbations to the particle orbits leading to super-adiabatic motion which would tend to enhance the barrier created by the weak interaction (FLR effect) alone. We could not, however, obtain criteria for adiabacity in the presence of multiple frequencies and wave number spectra as would be required for a realistic case. The analysis of the fundamental ICRH minority scheme [12] however shows that the inclusion of the spectral effects will increase stochasticity considerably and move the adiabatic barrier to higher energies. It was also seen that the trapped ion motion is more stochastic than the motion of passing ions—here the energetic particles are mainly trapped. Adiabatic motion is therefore not likely to be of importance for the distribution below E^*.

6. Conclusions

The experiments presented in this paper show clear clamping of the high-energy part of the second harmonic ICRF heated minority ions. The energy, around which the clamping occurs, is

consistent with the expected energy where the ICRF waves and the particles interact weakly due to the finite Larmor radius effect. For the first time systematic experimental evidence together with modelling including relevant physics has been presented that demonstrates the importance of the finite Larmor radius effects on the high energy part of the resonant ion distribution. For all heating schemes, the increased magnetic field will move E^* to higher energies and increased electron density will move E^* to lower energies roughly as $E^* \propto B^2/n_e$. In the ITER case the magnetic field and the electron density are normally significantly higher than here. Due to E^*'s higher sensitivity on magnetic field strength E^* will typically be in multi-megaelectronvolt range in the ITER. Thus, it can be concluded that the FLR effects are not likely to limit the fast ion energies in ITER. However, it also should be noted that the relatively low amount of power per particle available in ITER main heating scenarios will usually guarantee that the fast ion tail will not be able to develop up to E^* and therefore the ICRF power will be channelled to the bulk ions as desired.

References

[1] Mantsinen M J, Eriksson L -G, Gondhalekar A and Hellsten T 1999 *Nucl. Fusion* **39** 459
[2] Stix T H 1975 *Nucl. Fusion* **15** 737
[3] Spitzer L Jr 1965 *The Physics of Fully Ionized Gases* 2nd edn (New York: Interscience)
[4] Eriksson L-G and Hellsten T 1995 *Phys. Scripta* **55** 70
[5] Eriksson L-G, Hellsten T and Willén U 1993 *Nucl. Fusion* **33** 1037
[6] Kolesnichenko Ya I, Lutsenko V V, White R B and Yakovenko Yu V 2000 *Nucl. Fusion* **40** 1325
[7] Helander P and Lisak M 1992 *Phys. Fluids* B **4** 1927
[8] Stix T H 1985 Application of RF waves to tokamak plasmas *Proc. Course Workshop (Varenna, 1985)* vol 1 (Perugia: Monotypia Franchi) p 24
[9] Korotkov A A, Gondhalekar A and Stuart A J 1997 *Nucl. Fusion* **37** 35
[10] Carlsson J, Eriksson L-G and Hellsten T 1997 *Nucl. Fusion* **32** 719
[11] Testa D, Core W G F and Gondhalekar A 1999 *Phys. Plasmas* **6** 3498–510
[12] Bergeaud V, Nguyen F, Becoulet A and Eriksson L-G 2001 *Phys. Plasmas* **8** 139

PUBLICATION II

ASCOT Modelling of Ripple Effects on Toroidal Torque

In: Contributions to Plasma Physics 48,
pp. 77–81, 2008.

Contrib. Plasma Phys. **48**, No. 1-3, 77 – 81 (2008) / **DOI** 10.1002/ctpp.200810013

ASCOT Modelling of Ripple Effects on Toroidal Torque

A. Salmi[*1], **T. Johnson**[2], **V. Parail**[3], **J. Heikkinen**[4], **V. Hynönen**[1], **T. P. Kiviniemi**[1], **T. Kurki-Suonio**[1], and **JET EFDA Contributors**[**]

[1] Helsinki University of Technology, Association Euratom-Tekes, Finland
[2] Association EURATOM-VR, Fusion Plasma Physics, EES, KTH, 10044 Stockholm, Sweden
[3] Euratom/UKAEA Fusion Association, Culham Science Centre, Abingdon, OX14 3DB, UK
[4] VTT, Association Euratom-Tekes, Helsinki, Finland
[**] See appendix of M.L. Watkins, et al., Fusion Energy 2006 (Proc. 21th Int Conf. Chengdu) IAEA (2006)

Received 23 May 2007, accepted 17 November 2007
Published online 18 March 2008

Key words MC, GC orbit following, ripple, torque.
PACS 52.25.Fi, 52.55.Fa, 52.65.Pp

Toroidal field ripple, δ=(B_{max}-B_{min})/ (B_{max}+B_{min}), in ITER will be relatively large, about 0.5% at the outer midplane. Due to the importance of toroidal rotation on plasma stability and confinement it is important to understand the consequences of a non-negligible ripple field on rotation. Guiding centre following Monte Carlo code ASCOT is used to evaluate the torque on plasma from co-current NBI in presence of toroidal magnetic field ripple. Simulations are made for a JET discharge from 2007 Ripple Campaign aimed to clarify the effect of ripple on fusion plasmas in preparation for ITER. ASCOT results show large reduction of torque from co-NBI and negative torque from thermal ions, which together could create a counter rotating edge plasma.

1 Introduction

Toroidal magnetic field ripple is known to have an effect on plasma density, rotation and confinement. Energetic ions, e.g. fusion alphas and NB and RF heated ions are most vulnerable to ripple and it has been studied much before. The increased losses of fast ions naturally lead to both; decreased heating efficiency and increased heat load on the vessel first wall. However, they may also play a crucial role in the loss of confinement through ripple reduced toroidal rotation. Toroidal field ripple breaks the axi-symmetry of the magnetic field which allows the ions and the toroidal field coils to exchange toroidal momentum. As ITER, having 18 toroidal field coils, will be operating in relatively strong ripple field it is important to understand the effect that ripple has on plasma toroidal rotation.

Recognising the importance of ripple on ITER and its design, JET launched its third ripple campaign in 2007 to study these effects in a controlled way. JET has the capability to drive uneven currents in the adjacent coils thus gaining control over the level of ripple. In JET Ripple Campaign 2007 (RIP3) some discharges have shown that with increased level of ripple the toroidal rotation can reverse to counter direction (relative to the current and NBI injection angle) [1]. Although fast ions and ripple have an important role when explaining experimental observations it is generally not possible to limit the analysis for fast ions only. The ripple can namely also affect thermal ions. For thermal ions, however, the effect of ripple is much affected by the radial electric field in the plasma in particular close to the separatrix where the thermal energy is comparable to the potential well depth.

In this contribution plasma discharges from the JET RIP3 Campaign are analysed with a guiding centre following Monte Carlo code ASCOT [2]. Toroidal torque in presence of magnetic ripple is calculated from both fast (NBI) and thermal ions. ASCOT results show that NBI heated JET plasma can produce torque that can give rise to counter rotation if ripple is high enough and/or torque from the thermal ions is taken into account.

*Corresponding author: e-mail: antti.salmi@tkk.fi

2 Torque from NBI in presence of ripple

NBI ions usually have much greater kinetic energy than the electrostatic potential difference that they encounter during their orbit. Radial electric field is then not expected to more than make a small perturbation on fast ion orbits. We will therefore neglect the electric field when estimating the torque from NBI. The experimental set-up for the discharge, #69648 (60s), being investigated is: 15.4 MW of co-current NBI with an average injection energy of 75 keV, central electron density $n_{e,0} = 5 \times 10^{19}$ m^{-3}, central electron temperature $T_{e,0} = 5$ keV, density and temperature at the pedestal top $n_e = 3 \times 10^{19}$ m^{-3} and $T_{e,i} = 1$ keV. With these parameters the plasma is in the banana regime.

ASCOT simulations use EFIT reconstructed magnetic equilibrium and experimental plasma density and temperature profiles. As an NBI source for ion birth profile ASCOT uses Fokker-Plank code PENCIL. Ion birth profiles are sampled to generate typically 10^4 test particles. The ripple model in ASCOT uses a numerical poloidal 2D map of the toroidal field ripple and sinusoidal harmonics in toroidal direction.

To illustrate the agreement between ASCOT and PENCIL when ripple is not present Fig. 1 shows a comparison between the codes. The scenario used for this is the JET shot #69648 which had $\delta = 1\%$ ripple at the outer midplane separatrix but which was set zero in the simulation to allow for comparison. As can be seen the agreement is very good especially in the middle of the minor radius[1] where also most of the power goes. The difference close to the separatrix is due to orbit losses, which PENCIL does not evaluate. The reason for the difference in the central plasma is attributed to the fact that in PENCIL all of the power and torque end up on the same flux surface where the neutrals were first ionised. ASCOT, however, accounts both collisional transport effects and the shift in radius between ion birth point and the bounce average GC position. The beam deposition being mostly off axis and injection in co-current direction means that both these and volumetric effects tend to enhance the power density in the central plasma as compared to PENCIL.

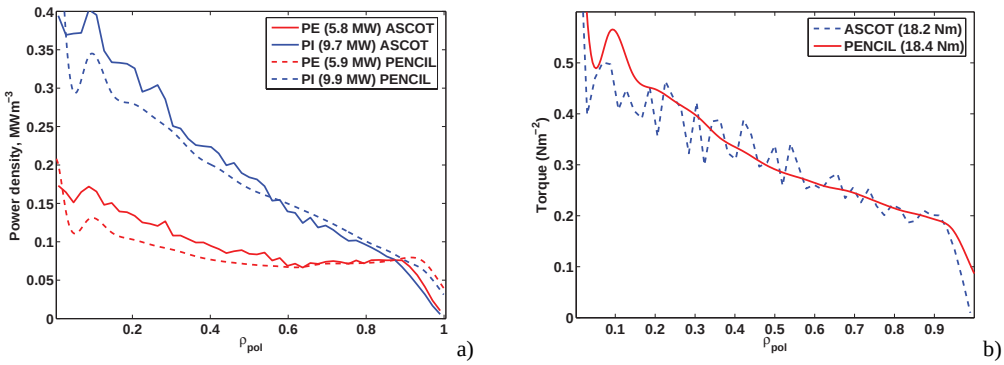

Fig. 1 a) Power and b) torque density profiles comparing PENCIL and ASCOT for #69848 without ripple. Positive sign in torque refers to co-current direction. (Online colour: www.cpp-journal.org.)

In axi-symmetric field torque from NBI is transferred to the plasma either through particle collisions on through the *instantaneous* current originating from the difference in particle birth point and its bounce averaged position. To maintain quasi-neutrality the plasma sets up a return current, which leads to torque through $j \times B$ force.

In the presence of ripple the canonical angular momentum is not conserved and ions can exchange momentum with the toroidal field coils. This leads to non-ambipolar radial current of ions, usually directed radially outwards. One can interpret this radial current as externally driven which can then induce torque on the plasma. As for the instantaneous (or direct) torque generation it is the requirement of quasi-neutrality that ensures that non-ambipolar radial current leads to torque.

[1]Minor radius co-ordinate used here is $\rho_{pol} = \sqrt{(\Psi_{pol} - \Psi_{pol}(0))/(\Psi_{pol}(a) - \Psi_{pol}(0))}$, i.e. the square root of the normalised poloidal flux.

In ASCOT simulations the radial current includes both the instantaneous current and the ripple induced radial current and also the orbit loss current. We do not make a difference where the current originates. The $j \times B$ torque we quote is the sum of all these components. Figure 2a shows ASCOT results of momentum transfer into the plasma for #69648 without ripple. Torque has been split explicitly into two parts; a friction due to collisions between NBI ions and bulk plasma and a $j \times B$ part. More specifically the torque density is defined as $T = Rj_r B_{pol}$, where R is the major radius, j_r is the current density induced into the plasma and B_{pol} is the poloidal component of the magnetic field.

It can be seen that in the centre of the plasma, due to the small trapping fraction, only collisions can transfer toroidal torque from fast ions into the plasma. However, at outer part of minor radus, where the number trapped ions increases the radial current becomes larger and the $j \times B$ force becomes the dominating momentum exchange mechanism. Figure 2b shows the total torque profiles for three levels of ripple for a JET plasma #69648 with 15.8 MW of NBI which in axi-symmetric and lossless case would generate 18.4 Nm of co-current torque. It is seen that with increasing ripple the torque becomes negative at the edge; first only close to the separatrix but with $\delta = 1.69\%$ already at $\rho_{pol} = 0.7$. In the central part of the plasma, where the ripple is small and collisions dominate, the momentum transfer is almost unaffected by the ripple.

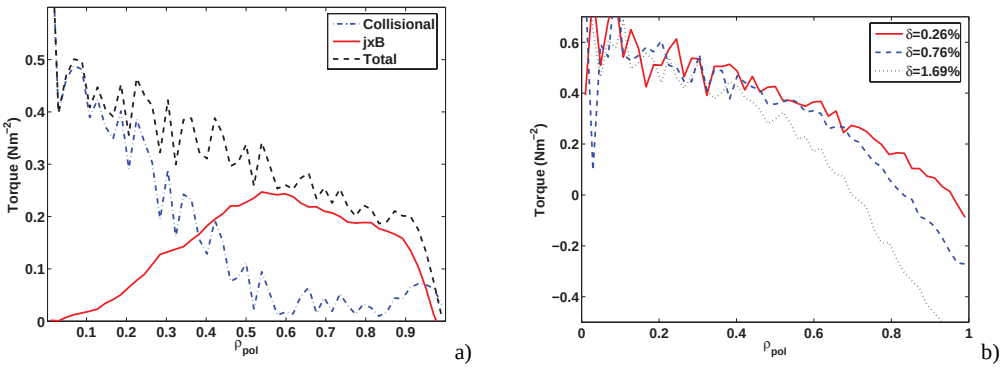

Fig. 2 a) Torque profile split into collisional and $j \times B$ parts and b) total torque for 3 levels of ripple. Co-current torque is defined as positive. (Online colour: www.cpp-journal.org.)

Table 1 Total torque from a ripple scan for NBI heating case similar to #69648. Here *Wall* denotes the torque lost through separatrix along with escaped NBI ions, *Colls* is the torque received by the plasma through collisional slowing down of fast ions, $J \times B$ is the torque on plasma due to non-ambipolar radial current of fast ions, *Co-torque lost* is the loss of co-current initial torque and *Power lost* is the lost NBI power. Initial torque evaluated from ion birth profile for all cases is 18.4 Nm.

Ripple (%)	Wall (Nm)	Colls (Nm)	JxB (Nm)	Co-torque lost (%)	Power lost (%)
0.0	0.2	6.3	12	2	2
0.26	0.8	6.5	11	7	7
0.51	1.5	6.9	7.2	24	11
0.76	2.3	6.7	2.0	54	16
1.00	2.9	6.7	-3.2	82	21
1.69	3.8	6.5	-15	150	30
3.26	4.2	6.0	-39	280	45

Table 1 shows the volume integrated values of the profiles shown in Fig. 1b together with other levels of ripple which were not plotted to keep the figure readable. Table 1 separates also the amount of momentum transferred

through collisions and through $j \times B$ force. This split shows clearly that collisional torque is almost independent of ripple. The torque from $j \times B$ force, which in modest ripple levels stays co-current becomes negative between $\delta = 0.76\% - 1\%$. This is because with small level of ripple the instantaneous current, which is directed radially inwards, dominates. With higher level of ripple radial current becomes more and more outward and negative total torque can result as also depicted in Fig. 3. Generally ripple induced torque is always counter current thus reducing torque from co-injected NB.

From momentum balance equation one finds that the total torque on the plasma must be negative if counter rotation at the edge is to be expected as observed in experiments [1]. According to ASCOT one finds that 18.4 Nm torque from 15.4 MW of NBI is reduced by 82% due to ripple. Although greatly reduced the total torque from NBI is still positive and can not alone explain why the edge was counter rotating. The missing negative torque is believed to arise from the thermal ions and it is studied in the next section.

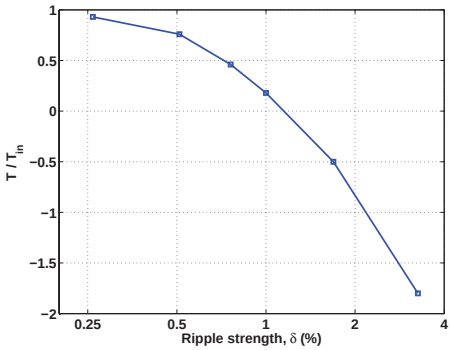

Fig. 3 ASCOT calculated torque divided by input NBI torque. For small ripple levels the total torque is close to the beam input but as the ripple is increased more and more of co-torque is lost dominantly through the ripple induced outward radial current. With ripple exceeding 1% the total torque becomes counter NBI. As expected ripple reduces the torque near quadratically for ripple levels up to 0.8% after which the increase of counter torque slows down to near linear since relatively weak collisions do not continue to maintain pure stochastic behaviour of ripple diffusion.

3 Torque from thermal plasma in presence of ripple

Estimating the torque from thermal ions due to ripple is more complicated than for fast ions due to the existence of radial electric field. Radial electric field perturbs the orbits of thermal ions relatively strongly because usually the depth of the potential well is of the order of thermal energy. Ripple generated torque from the thermal ions is tightly coupled with the radial electric field.

To study this effect one should, in principle, solve the radial electric field self-consistently using *full-f* techniques and collisions that conserve energy and momentum because of the importance of the edge region where ripple is strongest and particle distributions asymmetric. In addition when interpreting experiments one really should have a simulation system, which is not sensitive to initial conditions. To make plasma profiles consistent with experimental heat and particle fluxes, recycling and radial electric field, transport time scale simulations would be needed. One also might need to include the effect from ELM's and turbulence to match simulations and experiments.

To avoid these complications and the noise from time varying electric field, which are likely to confuse the interpretation of the ripple effects, we fix the radial electric field in these simulations. We use the equation [3] with zero toroidal rotation condition:

$$E_r = \frac{T}{e}\left(\frac{n'}{n} + \gamma\frac{T'}{T}\right) \tag{1}$$

to solve the electric field. Although this estimate clearly does not produce the correct electric field it will serve for our purposes in estimating the effect of electric field on the torque generated by the ripple.

We set up the simulations by loading 250 000 thermal test particles between $\rho_{pol} = 0.8 - 1.0$ homogeneously in phase space while maintaining the experimental temperature and density profiles. Test particles collide against fixed Maxwellian background and are allowed to escape the plasma. No recycling is used. Maxwellian collisions used here are expected to be more efficient in providing ion flux into ripple trapped region of phase space than

conserving collisions due to asymmetric distribution close to the edge. In the end, even in this case we lose at most 0.2% of the particles due to ripple trapping justifying the use of non-conserving collisions for this analysis.

Figure 4 shows the torque from thermal ions in the presence of ripple as a function on radial electric field strength. The torque shown is only due to ripple and it is separated from the torque arising from orbit losses. Note that without ripple $j \times B$ torque and collisional torque cancel each other exactly due to ambipolarity except close to the edge where orbit losses occur. In 1% ripple field but without electric the resulting torque (-40 Nm) is more than twice and counter of what can be achieved with 15.4 MW of NBI in the absence of ripple and about 10 times and counter of what remained from NBI in the ripple field. From experiments we know that total torque on the plasma must be very small as edge rotation was marginally counter. From Fig. 4a we can read that ASCOT results indicate that thermal torque would be of the correct order (~ -5 Nm) if the NC electric field was enhanced by a factor of 3.5. This enhancement could result, e.g. from ripple itself. Without self-consistent evaluation of electric field one can not say quantitatively if the ripple acting on the thermal component explains the counter rotation observed but these calculations indicate that it is indeed a good candidate.

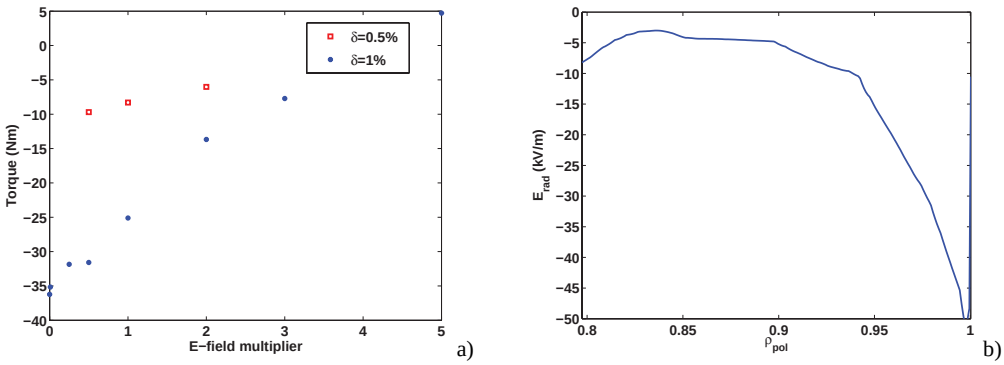

Fig. 4 a) Torque from thermal ions with ripple and b) radial electric field without scaling factor.

4 Conclusions and Discussion

Ripple effects on toroidal torque generation have been modelled using GC following Monte Carlo code ASCOT. Simulations show that with $\delta = 1\%$ ripple the co-current torque from NBI is reduced by 82% from what would be achieved without ripple. Despite this large reduction of torque from NBI, the volume integrated torque remained positive. Main mechanism for the loss of co-torque is the increased ripple diffusion of fast ions leading to outward radial current. Due to the nature of momentum balance it could be concluded that torque from NBI alone could not explain experimentally observed counter rotating plasma edge.

Simulations with thermal ions showed large counter torque for smaller levels of radial electric field. With increasing (negative) electric field the amount of torque dropped to a level that could explain the measured counter rotation. Self-consistent evaluation of radial electric field with ripple, however, is needed to make quantitative conclusion of the thermal ion torque.

Acknowledgements This work has been partly funded by Fortum Säätiö

References

[1] P. de Vries et al., Toroidal Field Ripple and the formation of Internal Transport Barriers, Proceeding of 34th EPS Conf on Plasma Physics, Warsaw, Poland, June 2007.
[2] J. A. Heikkinen, S. K. Sipilä, Phys. Plasmas **2**, 3724 (1995).
[3] F. L. Hinton and R. D. Hazeltine, "Theory of plasma transport in toroidal confinement systems", Rev. Mod. Phys. **48**, 239 (1976).

PUBLICATION III

Effect of toroidal field ripple on plasma rotation in JET

In: Nuclear Fusion 48, 035007 (6 pp), 2008.

http://iopscience.iop.org/0029-5515/48/3/035007/pdf/0029-5515_48_3_035007.pdf

IOP PUBLISHING and INTERNATIONAL ATOMIC ENERGY AGENCY NUCLEAR FUSION

Nucl. Fusion **48** (2008) 035007 (6pp) doi:10.1088/0029-5515/48/3/035007

Effect of toroidal field ripple on plasma rotation in JET

P.C. de Vries[1], A. Salmi[2], V. Parail[1], C. Giroud[1], Y. Andrew[1], T.M. Biewer[3], K. Crombé[4], I. Jenkins[1], T. Johnson[5], V. Kiptily[1], A. Loarte[6], J. Lönnroth[2], A. Meigs[1], N. Oyama[7], R. Sartori[6], G. Saibene[6], H. Urano[7], K.-D. Zastrow[1] and JET EFDA Contributors[a]

JET-EFDA Culham Science Centre, OX14 3DB, Abingdon, UK
[1] EURATOM/UKAEA Fusion Association, Culham Science Centre, OX14 3DB, Abingdon, UK
[2] Association Euratom-Tekes, Helsinki University of Technology, PO Box 4100, 02015 TKK, Finland
[3] Oak Ridge National Laboratory, Oak Ridge, TN 37831, USA
[4] Department of Applied Physics, Ghent University, Ghent, Belgium
[5] Association EURATOM - VR, Fusion Plasma Physics, EES, KTH, Stockholm, Sweden
[6] EFDA Close Support Unit, c/o MPI für Plasmaphysik, 2 Boltzmannstrasse, 85748 Garching, Germany
[7] Japan Atomic Energy Agency, Naka, Ibaraki-ken 311-0193, Japan

E-mail: Peter.de.Vries@jet.uk

Received 31 August 2007, accepted for publication 26 November 2007
Published 23 January 2008
Online at stacks.iop.org/NF/48/035007

Abstract
Dedicated experiments on TF ripple effects on the performance of tokamak plasmas have been carried out at JET. The TF ripple was found to have a profound effect on the plasma rotation. The central Mach number, M, defined as the ratio of the rotation velocity and the thermal velocity, was found to drop as a function of TF ripple amplitude (δ) from an average value of $M = 0.40$–0.55 for operations at the standard JET ripple of $\delta = 0.08\%$ to $M = 0.25$–0.40 for $\delta = 0.5\%$ and $M = 0.1$–0.3 for $\delta = 1\%$. TF ripple effects should be considered when estimating the plasma rotation in ITER. With standard co-current injection of neutral beam injection (NBI), plasmas were found to rotate in the co-current direction. However, for higher TF ripple amplitudes ($\delta \sim 1\%$) an area of counter rotation developed at the edge of the plasma, while the core kept its co-rotation. The edge counter rotation was found to depend, besides on the TF ripple amplitude, on the edge temperature. The observed reduction of toroidal plasma rotation with increasing TF ripple could partly be explained by TF ripple induced losses of energetic ions, injected by NBI. However, the calculated torque due to these losses was insufficient to explain the observed counter rotation and its scaling with edge parameters. It is suggested that additional TF ripple induced losses of thermal ions contribute to this effect.

PACS numbers: 52.55.Fa, 52.65.Cc, 52.50.Gj

(Some figures in this article are in colour only in the electronic version)

1. Introduction

Plasma rotation is thought to play an important role in the stability properties of tokamak plasmas. Furthermore, rotational shear could affect plasma turbulence and consequently has an impact on transport processes and the performance of tokamak plasmas. Hence it is relevant to accurately predict the rotation properties of ITER plasmas.

Because of the finite number of toroidal field (TF) coils, a toroidal variation (ripple) of the main magnetic field exists in tokamaks. The TF ripple breaks the axisymmetry of the magnetic field and enhances particle losses, in particular energetic ions, such as alpha particles created in fusion reactions or those injected by the neutral beam (NB) system. These non-ambipolar ion losses are expected to have a non-negligible effect on the plasma rotation. Ferrite material will be mounted between the ITER coils in order to reduce the ripple. Nevertheless, the estimated maximum TF ripple at the

[a] See appendix of Watkins M.L. *et al* 2006 *Proc. 21st Int. Conf. on Fusion Energy 2006 (Chengdu, China)* (Vienna: IAEA).

separatrix in ITER is in the order of $\delta \sim 0.5\%$ while this value in JET is only $\delta \sim 0.08\%$. The maximum ripple at the separatrix is mostly found at the outboard mid-plane. Here the TF ripple amplitude, δ, is defined as the relative amplitude of the magnetic field variation: $\delta = (B_{max} - B_{min})/(B_{max} + B_{min})$. In order to extrapolate the rotation properties of present experiments to that of ITER plasmas, TF ripple effects should be understood.

Studies on TF ripple induced particle losses have been reported by several devices [1–3]. Previous experiments on JET reported a reduction of the NB driven plasma rotation with TF ripple [4]. In JT-60U significant plasma rotation in the counter-current direction was observed with near perpendicular neutral beam injection (NBI) in the presence of a TF ripple of $\delta \sim 1\%$ [5]. However, the rotation characteristics of the JT-60U plasmas were altered after the TF ripple was reduced using ferrite inserts [6, 7]. Up to now, no detailed, quantitative analysis of TF ripple effects on plasma rotation has been carried out.

At JET it is possible to vary the TF ripple amplitude by independently powering the odd and even-numbered TF coils. The imbalance current between the two sets of coils can be changed arbitrarily, increasing the TF ripple up to $\delta \sim 3\%$. A series of experiments has been performed analysing the effects of TF ripple by increasing its value on a pulse-by-pulse basis from the standard JET value of $\delta \sim 0.08\%$ up to $\delta \sim 1.5\%$. The plasma rotation has been measured by means of charge exchange recombination spectroscopy (CXRS). The measured quantities are those of carbon ions and here it is assumed that the main plasma ions have equal temperature and velocities.

This paper presents the effects of an enhanced TF ripple on the plasma rotation. In the second section the scaling of JET plasma rotation with TF ripple is presented. The basic mechanisms via which TF ripple affects the plasma rotation are discussed and experimental examples are shown. The experimental observations are compared with modelling of TF ripple induced particle losses. By means of the orbit following Monte Carlo code ASCOT, the trajectories of energetic ions, for example those injected by the NB system and those accelerated by ICRH, can be accurately traced in the presence of TF ripple [8]. This enables the determination of the fraction of energetic particles lost due to the TF ripple. These calculations are discussed in section 3 and compared with detailed experimental analysis. Finally the observations are summarized and the implications for ITER are discussed in section 4.

2. TF ripple and plasma rotation

Dedicated experiments were carried out in which the TF ripple in JET was artificially increased. These experiments were done with various plasma parameters. In order to compare rotation properties of different experiments, it is convenient to use the dimensionless thermal Mach number, defined as the ratio of the rotation velocity and the thermal or ion sound velocity [9]. In figure 1, the toroidal Mach numbers measured at the plasma centre ($R = 3.1$ m, $\rho \sim 0$) and edge ($R = 3.8$ m, $\rho \sim 0.9$) are shown as a function of TF ripple amplitude, where R is the location in major radius and the ρ co-ordinate is the

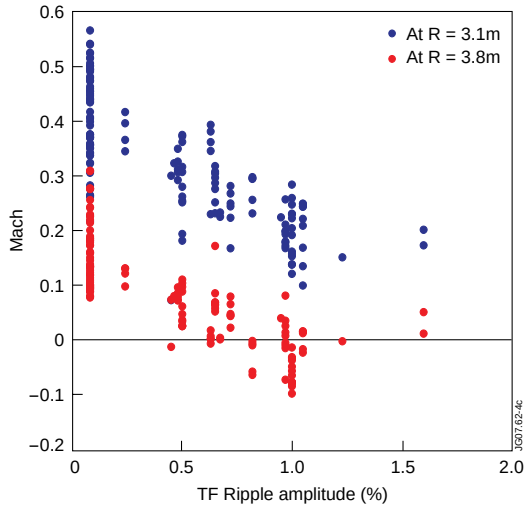

Figure 1. Mach numbers measured at the plasma centre ($R = 3.1$ m, $\rho \sim 0$) and edge ($R = 3.8$ m, $\rho \sim 0.9$) are shown asa function of TF ripple amplitude at the outer separatrix. The data have been taken over various scenarios and plasma conditions.

normalized square root of the poloidal flux. The central Mach number decreases from standard values of $M = 0.40$–0.55 to $M = 0.25$–0.35 for $\delta = 0.5\%$ and $M = 0.1$–0.3 for $\delta = 1\%$. For these experiments the NBI system is the only external source of momentum.

A few data points around $\delta \sim 1.5\%$ seem to break the trend. However, one should be aware that these discharges were all in the L-mode with low levels of NBI power ($\sim$3–4 MW^{-1}). At this TF ripple amplitude, NBI operations was restricted due to the power large loss fraction and the resulting power loads on in-vessel components. JET operation at the predicted ITER TF ripple amplitude of $\delta = 0.5\%$ shows a significantly lower rotation compared with those at $\delta = 0.08\%$. For higher TF ripple amplitudes ($\delta \sim 1\%$) negative Mach numbers, i.e. counter rotation, is observed at the edge in various discharges while the core still rotates in the co-current rotation. The core and edge poloidal rotation velocity have been measured for plasmas with and without TF ripple. First results indicate that there is no significant effect of TF ripple on the core poloidal rotation. The influence of ripple on poloidal rotation in the core and edge region is currently under investigation.

The question that arises is, how does the TF ripple reduce toroidal plasma rotation? But firstly it is useful to recall the mechanisms of NBI momentum transfer to the bulk plasma. Because of the tangency of the neutral beams at JET, the particles carry toroidal momentum and the NBI system exerts a toroidal torque on the plasma which is directed in the co-current direction (see figure 2). This torque, called NBI torque (T_{NBI}) in this paper, depends on the energy of the beam particles, particle flux and the tangency of the beams. There are three mechanisms explaining how this NBI torque acts on the plasma and the NBI momentum is transferred, which are described in detail in [10]. After ionization the injected NB particle can either become a passing particle or be trapped in a banana-orbit.

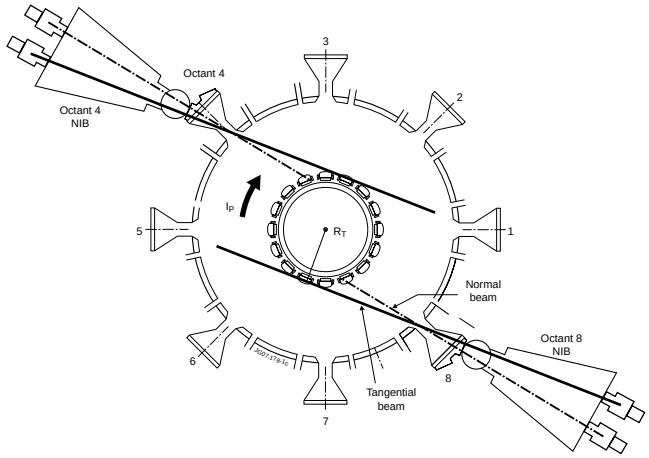

Figure 2. The location of two NB heating systems are shown on the top view of the JET torus. Both inject usually in the co-current direction. Each system consists of eight independent NB injectors, of which half are aligned with a tangency radius of $R_T = 1.31$ m (the so-called normal injection) while the other half have a tangency radius of $R_T = 1.85$ m (the so-called tangential injection), as indicated in the figure. The major radius of the JET torus is $R_o = 2.95$ m.

This depends on the position where the particle is deposited and the tangency of the NB. Passing particles transfer their momentum in two ways, either via collisions with the bulk plasma or by enhancement of the total angular momentum once the particles can be assumed thermalized. The characteristic transfer rate of these two mechanisms is in the order of the ion–ion collision time. The third mechanism is connected to those particles injected into banana-orbits. Since there is a radial separation of the position where the NB particle is ionized and its bounce averaged radial position, there is a radial current of fast ions. In order to maintain quasi-neutrality, there has to be a radial displacement current in the background plasma resulting in a $\boldsymbol{j} \times \boldsymbol{B}$ torque. This torque is transferred during one bounce time of the trapped particles and because of this fast time scale this torque component is often called the 'instantaneous' torque.

The presence of a TF ripple affects the energetic particles that are, for example, injected by the NB system in two ways. Firstly, particles can be trapped in the magnetic ripple. Being toroidally trapped, the field curvature causes these particles to drift out of the plasma. Secondly, the TF ripple alters the trajectory of particles trapped in banana-orbits and causes these to drift radially outwards [11]. Both losses have an effect on the plasma rotation. Toroidal rotation can be damped by friction between the circulating particles and those locally trapped in the TF ripple [12]. Furthermore, the TF ripple can be viewed as an external force that drives non-ambipolar radial current. The outward ion loss flow, due to, for example, banana-orbit diffusion, induces a radial return current, j, in order to preserve neutrality. This gives rise to a $\boldsymbol{j} \times \boldsymbol{B}$ torque on the plasma which is in the counter-current direction. This return current is similar, but unrelated, to the return current that creates the 'instantaneous' torque. Note that the 'instantaneous' torque is always directed in the same direction as NBI and is unaffected by the ripple, while the TF ripple induced $\boldsymbol{j} \times \boldsymbol{B}$ torque is always directed counter-current. NBI particles that are directly injected in the TF ripple should be treated similar to those trapped in banana-orbits and these would therefore contribute to the 'instantaneous' torque. This contribution may, however, be negligible compared with the counter-current torque generated by the losses of these particles.

For high enough TF ripple the torque from the non-ambipolar radial current, here called T_{RIP}, can become non-negligible and have an important effect on the plasma rotation. The reduction of plasma rotation or angular momentum with TF ripple, as observed in figure 1, implies a loss of momentum compared with that injected by the NB system. The momentum loss from the plasma is, however, transferred via the TF ripple to the coils, thus momentum conservation is not violated.

The first mechanism, involving friction with particles trapped in the TF ripple, tends to relax the plasma rotation to zero, while the second mechanism, related to banana-orbit diffusion, actually drives rotation in the counter-current direction. This first effect depends on the number of particles trapped in the TF ripple, while the second will be stronger in the case of a larger fraction of particles that are trapped in banana-orbits. The latter effect can be illustrated by comparing discharges with a large TF ripple but using different angles of NBI. At JET the NB system can apply near tangential injection with a tangency radius of $R_T = 1.85$ m ($\theta_{inject} \sim 25^\circ$) and so-called normal injection with smaller tangency radius of $R_T = 1.31$ m ($\theta_{inject} \sim 17^\circ$) (see figure 2). The major radius at JET is $R_o = 2.95$ m. The beam energy varies between 70 and 130 keV. In figure 3, two discharges are shown both with a TF ripple of $\delta = 0.5\%$ but one with predominantly tangential and the other so-called normal NBI. The powers in both discharges are chosen such that the total toroidal torque applied by NBI ($T_{NBI} = 15.1 \pm 1$ Nm) is the same in both discharges. The overall rotation of these two discharges is reduced considerably compared with similar discharges with minimum ripple ($\delta = 0.08\%$). Furthermore, it can be seen that the plasma with tangential NBI has significantly larger (20%) angular momentum compared with the one with normal

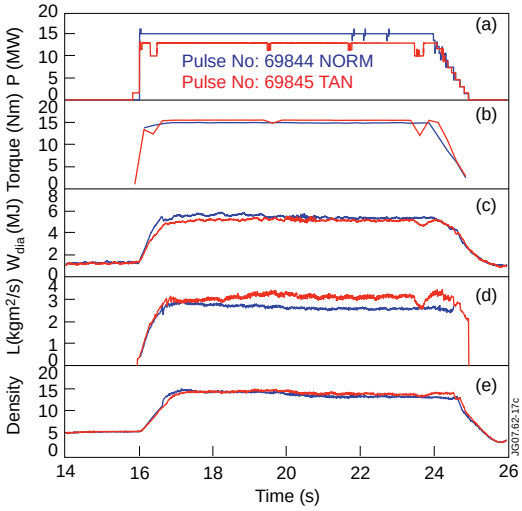

Figure 3. (*a*) NBI power for the two JET discharges with predominantly normal and tangential injection in blue and red, respectively. Lower power was injected in the discharge with tangential NBI. The TF ripple in both discharges was $\delta = 0.5\%$. (*b*) The toroidal torque applied by NBI. (*c*) The diamagnetic energy. (*d*) The total angular momentum. The lower angular momentum is found for the discharge with normal NBI. (*e*) The line-integrated density in $10^{19}\,\mathrm{m}^{-2}$.

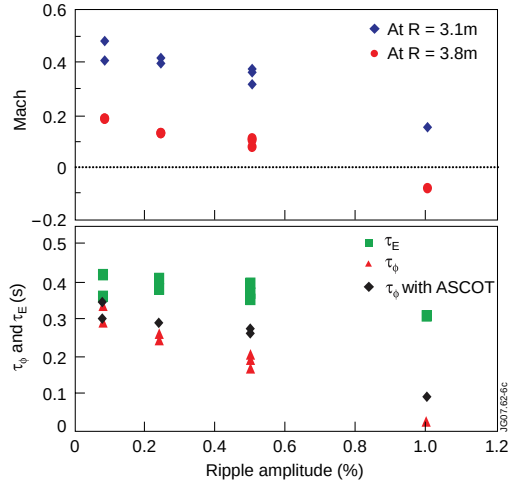

Figure 4. Series of identical type I ELMy H-modes pulse but with increasing TF ripple. The top graph shows again the core ($R = 3.1\,\mathrm{m}$, $\rho \sim 0$) and edge ($R = 3.8\,\mathrm{m}$, $\rho \sim 0.9$) Mach number, while the bottom graph presents the energy (green squares) and momentum (red triangles) confinement times. The black diamonds show the momentum confinement times with the toroidal torque calculated by ASCOT.

injection. Such a difference is not observed in discharges with a standard JET ripple of only $\delta = 0.08\%$, indicating that the difference is due to TF ripple.

The observed difference in toroidal rotation can be explained by the fact that normal NBI produces more ions that are trapped in banana-orbits, which are affected by the TF ripple. The higher density of trapped particles in the presence of a large TF ripple results in a larger counter torque induced by the radial banana-orbit diffusion (T_{RIP}), hence reducing the rotation. ASCOT indeed calculates a larger power loss fraction for the case with normal bank injection, 13% compared with 9%. ASCOT is able to calculate the resulting induced $\boldsymbol{j} \times \boldsymbol{B}$ torque due to these losses. It determined that these extra losses resulted in a lower torque (by 2.7 Nm) for plasma with normal NB. The total torques on the plasma calculated by ASCOT, including the external NBI (T_{NBI}) and that induced by TF ripple losses (T_{RIP}), were $T_{\mathrm{NBI}} + T_{\mathrm{RIP}} = T_{\mathrm{ASCOT}} = 9.1\,\mathrm{Nm}$ and $T_{\mathrm{ASCOT}} = 11.8\,\mathrm{Nm}$ for the normal and tangential cases, respectively.

The dependence on the fraction of particles trapped in banana-orbits indicates that the toroidal rotation is likely affected by the banana-orbit diffusion losses. ASCOT calculations show that the fraction of particles lost due to trapping by the TF ripple is negligible (less than 0.1%) for the small to medium levels of TF ripple discussed in this paper $\delta < 1.0\%$. Hence, the friction of these trapped particles with the rotating plasma can be neglected. The ASCOT calculations have shown that the radial profile of the TF ripple induced torque is not confined to the edge of the plasma. The radial profile of the TF ripple driven $\boldsymbol{j} \times \boldsymbol{B}$ torque can affect the region from $\rho > 0.5$ for $\delta = 1\%$ [8].

3. Comparison of experiment and modelling

In figure 4 a dedicated TF ripple scan is shown, where besides the TF ripple, the other plasma parameters are kept unchanged in a series of ELMy H-mode discharges. Again the Mach number and total angular momentum are found to decrease with TF ripple amplitude. Furthermore the momentum confinement time, τ_ϕ, defined as the ratio of the total angular momentum and the externally applied torque by NBI (T_{NBI}), is found to be much smaller than that of the energy confinement time. In JET for a standard TF ripple ($\delta = 0.08\%$) these parameters are found to be of the same order of magnitude [12]. The slight drop in energy confinement time with TF ripple is due to the degradation of the H-mode pedestal for larger TF ripple as discussed in detail in [13].

As shown in the previous section, the torque on the plasma is not due to NBI alone but also TF ripple induced losses also play a role. Thus, the momentum confinement time should be determined using the torque as calculated by ASCOT, which include TF ripple effects ($T_{\mathrm{ASCOT}} = T_{\mathrm{NBI}} + T_{\mathrm{RIP}}$). These values are shown in figure 4 to be larger than the original confinement times but the values still drop with ripple amplitude and are considerably lower than those of the energy confinement. Figure 5 shows that the angular momentum for these discharges scales with the torque as calculated by ASCOT. All these discharges had approximately the same NBI torque (T_{NBI}). The offset scaling indicates that either the momentum transport is strongly affected by the TF ripple or the TF ripple induced counter torque (T_{RIP}) as calculated by ASCOT is too small. Negative or counter rotation has been observed at the edge in discharges for which ASCOT still calculates a positive total torque. The ASCOT calculations show that for a TF ripple $\delta = 1\%$ approximately 67% of the co-NBI torque (T_{NBI}) is lost

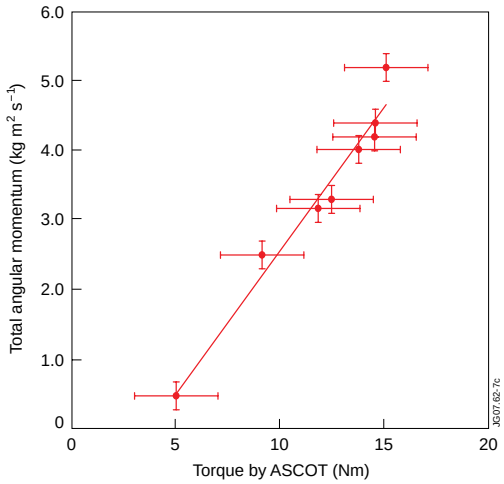

Figure 5. The total angular momentum as a function of the torque as calculated by ASCOT (including TF ripple effects) for the discharges shown in figure 4. The NBI torque for each of these discharges varied between $T_{\mathrm{NBI}} = 14.8$–17.1 Nm. The main variation of total torque as calculated by ASCOT was obtained by changing the TF ripple amplitude.

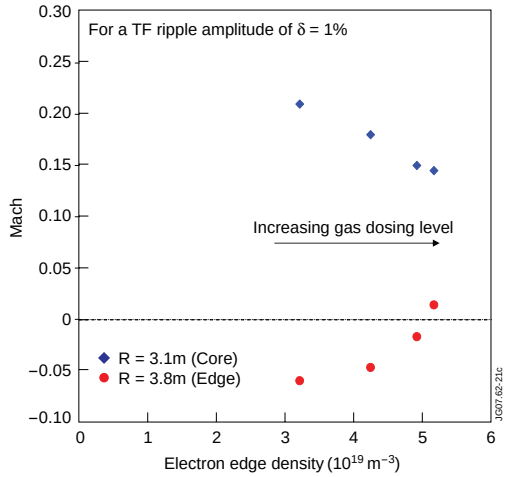

Figure 6. The core (blue diamonds) and edge (red circles) plasma rotation as a function of the edge density (e.g. increasing gas dosing).

due to a counter acting TF ripple torque (T_{RIP}). However, the negligible angular momentum indicates that this may be nearer to 100% of the NBI torque ($T_{\mathrm{NBI}} \sim -T_{\mathrm{RIP}}$) or that another source for negative torque is present. If one would assume the same momentum confinement time for all the discharges in figure 5, one could determine the required torque. For the discharge with almost negligible angular momentum ($\delta = 1\%$) this gives ∼2 Nm, which is several Nm smaller than provided by the ASCOT (∼5 Nm). The effect of TF ripple on the torque is much stronger than on the fractional loss of heating power, which is estimated to be in the order of about 18% in this case. A further increase of TF ripple would have led to a spin-up in the counter direction.

The edge counter-current rotation with TF ripple amplitude of $\delta = 1\%$ seems similar to that observed in JT-60U prior to the installation of ferrite inserts when the TF ripple was in the order of $\delta = 1$–2%. The counter-current rotation in JET was found to depend on local plasma conditions. For example, a fast increase of counter-current rotation was seen at times when an H-mode pedestal built up. Furthermore, increasing the edge density could reduce the counter rotation. In figure 6, the edge ($R = 3.8$ m, $\rho \sim 0.9$) and core ($R = 3.1$ m, $\rho \sim 0$) rotation for a series of four discharges (ELMy H-mode) is shown with varying amounts of gas dosing. The edge temperature was reduced while the edge density was increased due to the gas dosing, yielding a change in normalized edge collisionality from $\nu^* = 0.08$ to 0.28. Levels up to 4.5×10^{22} electrons per second were used. The fast counter-current rotation at the edge of $M_{\mathrm{edge}} = -0.06$ for the unfuelled case reverses to the co-current direction at high levels of gas dosing. Consequently, the angular momentum increases. Although there are variations in density and temperature, these are mainly found at the edge, and do not significantly alter the ASCOT calculations for this series, all of which produce similar values of effective torque. The total angular momentum for the four discharges increases with density (from $L_{\mathrm{tot}} = 0.98$ to $1.20\,\mathrm{kg\,m^2\,s^{-1}}$). This increase was mainly due to the lower counter rotation at the edge. The energy confinement time was, however, similar for all the four discharges. The change in angular momentum suggests that either the momentum confinement improves significantly with edge density or that the torque differs from that calculated by ASCOT. The actual torque may be affected by the higher edge density.

During the TF ripple experiments, the fastest cases of counter-current rotation have been observed in advanced tokamak scenarios. Compared with the base-line ELMy H-mode scenario these usually have high edge temperatures (∼1 keV). In advanced tokamak scenarios predominantly heated with co-current NBI and a TF ripple of $\delta = 1\%$, a large area of the plasma between $\rho = 0.6$ and 1 was found to rotate in the counter-current direction with co-rotation in the core [14].

These observations suggested that the level of negative, counter-current, edge rotation in the presence of large TF ripple would depend on the local temperature. In figure 7, the measured core and edge Mach numbers are shown for JET plasmas with a TF ripple of $\delta = 1\%$. All these discharges are predominantly heated by co-NBI. The edge rotation clearly correlates with the temperature. Discharges with very high edge temperatures produce a stronger counter-current rotation in the presence of a large TF ripple. The normalized edge collisionality ranged from $\nu^* = 0.04$ for the high temperature cases to $\nu^* = 0.5$ for the lower temperature and high density cases. This trend can partly explain the spread in the edge Mach numbers observed in figure 1, at the specific ripple amplitude of $\delta = 1\%$.

4. Discussion

TF ripple induced particle losses have been shown to affect the toroidal rotation of the plasma. The basic mechanisms

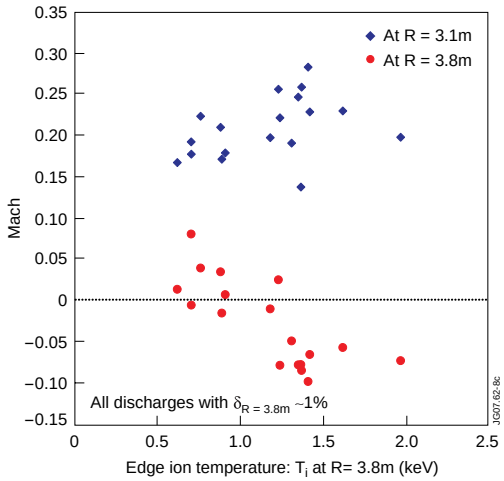

Figure 7. The centre and edge Mach number ($R = 3.8$ m, $\rho \sim 0.9$) for all JET discharges with a TF ripple of $\delta \sim 1\%$ (at $R = 3.8$ m) as a function of the local ion temperature.

behind the effect and experimental characteristics have been described.

Friction with particles trapped in the TF ripple cannot explain counter rotation. Furthermore, ASCOT calculations have shown that the loss fraction of particles due to trapping in the TF ripple is negligible (less than 0.1%) for the levels of TF ripple discussed in this paper, $\delta < 1.0\%$. The dominant mechanism that drives the observed edge counter rotation in JET discharges with a large TF ripple $\delta > 0.5\%$ can be associated with banana-orbit diffusion of trapped energetic ions. However, calculations of the induced torque due to these losses do not fully explain the observations. The edge toroidal rotation in the presence of a large TF ripple in JET depended on the local ion temperature or possibly collisionality, suggesting that other ion losses, possibly those of thermal ions, may be involved [15]. At a TF ripple amplitude of $\delta = 1\%$ these additional losses are thought to be responsible for a (counter) torque of several Nm. The effect of TF ripple on thermal ions has so far not been included in the ASCOT calculations shown in this paper.

Even for small TF ripple amplitudes of $\delta \sim 0.5\%$, which is expected in ITER, the JET plasma rotation was significantly reduced compared with normal levels. In JET discharges with a TF ripple of $\delta \sim 0.5\%$ the counter-current torque was found to be in the order of 20–30% of that supplied by the JET NBI system in the co-current direction. It should be noted that TF ripple in general does not reduce rotation, it merely provides a counter-current torque. In JT-60U with almost perpendicular NBI and larger ripple $\delta \sim 1\%$ the ripple induced ion losses may have been the dominant drive for the observed counter-current plasma rotation [5]. Furthermore, a larger angular momentum was observed when using counter-current compared with the co-current NBI in the presence of a TF ripple of $\delta \sim 0.5\%$ [7]. With counter-current NBI the TF ripple induced torque actually supports the NBI torque and enhances the angular momentum, albeit in the counter direction. This shows that the orientation of the NBI, e.g. tangential versus normal/perpendicular injection, at these ripple amplitudes is of importance.

Predictions for plasma rotation in ITER often assume that the momentum and energy confinement times are proportional and do not include TF ripple effects [16]. Predicting plasma rotation in ITER by extrapolating from present devices, such as JET, which have significantly lower TF ripple may, however, be more complicated. The TF ripple induced torque is always in the counter-current direction and will reduce the NBI co-current torque, yielding a lower rotation in ITER than presently expected. These experiments have shown that for TF ripple amplitudes of $\delta \sim 0.5\%$ the Mach numbers are approximately 30% low. However, to accurately quantify these effects detailed modelling of TF ripple effects on ITER rotation is required. The effect of thermal ion losses on the torque is being investigated, by modelling these losses with ASCOT. Initial results indicate that these losses may indeed contribute to the counter-current torque on the plasma [8].

Acknowledgments

This research was funded partly by the United Kingdom Engineering and Physical Sciences Research Council and by the European Communities under the contract of Association between EURATOM and UKAEA. The views and opinions expressed herein do not necessarily reflect those of the European Commission. This work was carried out within the framework of the European Fusion Development Agreement.

References

[1] Tobita K. *et al* 1995 *Nucl. Fusion* **35** 1585
[2] Redi M.H. *et al* 1995 *Nucl. Fusion* **35** 1509
[3] JET TEAM 1993 *Proc. 14th Int. Conf. on Plasma Physics and Controlled Nuclear Fusion (Würzburg, Germany, 1992)* (Vienna: IAEA) vol 1 p 429
[4] Tubbing B. *et al* 1995 *Proc. 22th EPS Conf. on Plasma Physics Controlled Fusion (Montpellier, France, 1995)* vol 19C p IV-001
[5] Koide Y. *et al* 1993 *Plasma Phys. Control. Nucl. Fusion Res.* **1** 777
[6] Yoshida M. *et al* 2006 *Plasma Phys. Control. Fusion* **48** 1673
[7] Urano H. *et al* 2007 *Nucl. Fusion* **47** 706
[8] Salmi A. *et al* 2007 ASCOT modelling of ripple effects on plasma rotation *Proc. 11th Int. Workshop on Plasma Edge Theory in Fusion Devices (Takayama, Japan, 2007)*
[9] de Vries P.C. *et al* 2006 *Plasma Phys. Control. Fusion* **48** 1693
[10] Zastrow K.-D. *et al* 1998 *Nucl. Fusion* **38** 257
[11] Goldston R.J., White R.B. and Boozer A.H. 1981 *Phys. Rev. Lett.* **47** 647
[12] Mikhailovskii A.B. 1995 *Phys. Lett.* A **198** 131
[13] Saibene G. *et al* 2007 Toroidal field ripple effects on H-modes in JET and implications for ITER *Proc. 34th EPS Conf. on Plasma Physics Controlled Fusion (Warsaw, Poland, 2007)* http://www.eps2007.ifpilm.waw.pl/pdf/O4_001.pdf
[14] de Vries P.C. *et al* 2007 Toroidal field ripple and the formation of internal transport barriers *Proc. 34th EPS Conf. on Plasma Physics Controlled Fusion (Warsaw, Poland, 2007)* http://www.eps2007.ifpilm.waw.pl/pdf/O4_002.pdf
[15] Parail V. *et al* 2006 *Proc. 21st Int. Conf. on Fusion Energy 2006 (Chengdu, China, 2006)* (Vienna: IAEA) CD-ROM file TH/P8-5
[16] Polevoi A.R. *et al* 2002 *Proc. 19th Int. Conf. on Fusion Energy 2002 (Lyon, France, 2002)* (Vienna: IAEA) CD-ROM file CT/P-08

PUBLICATION IV

Momentum transport studies in JET H-mode discharges with an enhanced toroidal field ripple

In: Plasma Physics and Controlled Fusion 52, 065004 (11 pp), 2010.

http://iopscience.iop.org/0741-3335/52/6/065004/pdf/0741-3335_52_6_065004.pdf

Plasma Phys. Control. Fusion **52** (2010) 065004 (11pp) doi:10.1088/0741-3335/52/6/065004

Momentum transport studies in JET H-mode discharges with an enhanced toroidal field ripple

P C de Vries[1,2], T W Versloot[2], A Salmi[3], M-D Hua[4], D H Howell[1], C Giroud[1], V Parail[1], G Saibene[5], T Tala[6] and JET EFDA Contributors[7]

JET-EFDA Culham Science Centre, Abingdon, OX14 3DB, UK
[1] EURATOM/CCFE Association, Culham Science Centre, Abingdon, OX14 3DB, UK
[2] FOM institute for Plasma Physics Rijnhuizen, Association EURATOM-FOM, PO Box 1207, Nieuwegein, The Netherlands
[3] Association Euratom-Tekes, Helsinki University of Technology, PO Box 4100, 02015 TKK, Finland
[4] Imperial College, SW7 2BY, London, UK
[5] Fusion for Energy Joint Undertaking, 0819 Barcelona, Spain
[6] Association Euratom-Tekes, VTT, PO Box 1000, 02044 VTT, Finland

E-mail: Peter.de.Vries@jet.efda.org

Received 20 November 2009, in final form 29 March 2010
Published 27 April 2010
Online at stacks.iop.org/PPCF/52/065004

Abstract
In this study, enhancement of the toroidal field (TF) ripple has been used as a tool in order to reveal the impact of the momentum pinch on the rotation profiles in H-mode JET discharges. The analysis showed that flatter rotation profiles were obtained in discharges with a high TF ripple, attributed to a smaller inward momentum convection. An average inward momentum pinch of approximately $V_p \approx 3.4\,\mathrm{m\,s^{-1}}$ and a normalized pinch value of $RV_p/\chi \approx 6.6$ could explain the observation. The data show that the momentum at the edge affects the peaking of the rotation and momentum density profiles. Under the assumption that the heat and momentum diffusivities are equal, an estimate of the levels of the momentum pinch in all discharges in the JET rotation database was made. For H-mode discharge these ranged from $0.3\,\mathrm{m\,s^{-1}} < V_p < 17\,\mathrm{m\,s^{-1}}$, with $2 < RV_p/\chi < 10$. A larger momentum pinch was found in discharges with a smaller density profile gradient length, i.e. a more peaked density profile.

(Some figures in this article are in colour only in the electronic version)

1. Introduction

The study of plasma rotation and momentum transport has gained interest over the last few years as rotation is thought to play an important role in the stability of tokamak plasmas. Furthermore,

[7] Annex to Romanelli F 2008 *Proc. 22nd IAEA Conf. on Fusion Energy 2008 (Geneva, Switzerland, 2008)* (Vienna: IAEA).

0741-3335/10/065004+11$30.00

it may affect transport properties via the stabilization of turbulence. A proper understanding of all aspects that affect the rotation of tokamak plasmas, in particular momentum transport and rotation sources, is therefore important if one wants to make an accurate prediction of the rotation in ITER.

Momentum transport was previously assumed to be closely linked to the transport of energy and hence in modelling predictions rotation profiles were thought to be similar to those of the temperature [1, 2]. It was shown, however, that such an assumption does not hold and effective energy and momentum diffusivities can differ significantly. The effective Prandtl number, i.e. the ratio of effective momentum and energy diffusivities, was found to be below unity in the core of JET plasmas [3, 4]. Furthermore, the global energy and momentum confinement times were not always equal and their ratio was found to increase with decreasing average rotation. Many of these aspects may be linked to the presence of a momentum pinch [5, 6]. Past experiments already indicated a convective component in momentum transport [7–9], while evidence for a momentum pinch has been found from experiments in various devices [10–13]. Beside these transport issues one needs to understand the sources of rotation. Generally considerable toroidal rotation has been observed in plasmas with tangential neutral beam injection (NBI), for which the momentum transfer from the injected particles to the bulk plasma seems to be reasonably well understood [14]. This picture is, however, complicated in the presence of a large toroidal field (TF) ripple which via non-ambipolar losses of fast (NBI) ions strongly influences the torque on the plasma [15]. Plasma rotation has also been observed in plasmas with no external momentum sources [16, 17] or those with balanced NBI [18], suggesting the presence of possible intrinsic momentum sources.

This paper will not deal in detail with mechanisms of TF ripple induced torque on the plasma but utilize TF ripple as a tool, in order to reveal the impact of the momentum pinch on the rotation profiles in H-mode JET discharges. The observations will be placed in the context of earlier studies done at JET [3, 4, 11]. The details of these specific experiments will be described in section 2. Thereafter, in section 3, the momentum transport properties of these discharges will be studied and compared with that of the energy. In section 4 it will be shown that an inward momentum pinch can explain the observations. The momentum pinch for these H-mode discharges will be determined and the magnitude of this pinch is estimated for all entries in the JET rotation database [4]. The last section will summarize the conclusions.

2. Description of the experiments

Standard operations at JET are carried out with a set of 32 TF coils all carrying equal current. But at JET it is possible to vary the TF ripple amplitude by independently powering the 16 odd and 16 even-numbered coils. The imbalance current between the two coil sets can be changed in a controlled way increasing the TF ripple. The TF ripple amplitude, δ_{B_T}, is defined as the relative amplitude of the magnetic field variation: $\delta_{B_T} = (B_{max} - B_{min})/(B_{max} + B_{min})$. The values quoted in this paper give the maximum amplitude in the plasma, found near the mid-plane ($z = 0$) at the low-field-side separatrix.

A series of experiments were performed to investigate the impact of the TF ripple on the H-mode pedestal properties [19, 20] for which the TF ripple was increased from the standard JET level of $\delta_{B_T} = 0.08\%$ up to 1.0%. This paper will discuss the characteristics of the rotation profiles and momentum transport in these experiments. In total, 16 discharges were analysed which were standard type I ELMy H-modes with a plasma current of $I_p = 2.6$ MA, a toroidal magnetic field of $B_T = 2.2$ T and $q_{95} = 3$, using a plasma configuration with a low triangularity and standard elongation ($\delta = 0.23, k = 1.65$). The auxiliary heating came from NBI only, which in JET is injected near tangentially, in the direction of the plasma current.

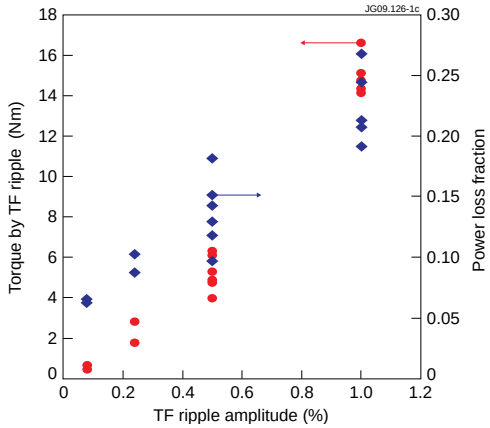

Figure 1. The power loss fraction (diamonds) and TF ripple induced counter-current torque (circles) as calculated by ASCOT for the series of discharges to be studied in this paper.

The NBI power ranged from 13 to 19 MW and supplied a toroidal torque of the order of 15 N m. Generally, these plasmas had equal ion and electron temperatures ($T_i/T_e \sim 1$) and density profiles with a typical inverse gradient length of $R/L_n \sim 2$. These H-mode plasmas can furthermore be characterized by the main global dimensionless parameters; normalized collisionality ($\nu^* = 0.007$–0.01), normalized Larmor radius $\rho^* = 2 \times 10^{-4}(0.02\%)$ and normalized β ($\beta_N = 1.7$–2.0). The effective charge of these plasmas was $Z_{eff} = 1.5 \pm 0.2$.

The TF ripple breaks the axi-symmetry of the magnetic field and enhances particle losses, in particular energetic ions, such as alpha particles created in fusion reactions or those injected by NBI. The non-ambipolar ion losses have a significant effect on the plasma rotation as have been shown experimentally [15, 21]. For the purpose of transport studies it is important to understand the energy and momentum sources, or torque deposition profiles, which will be affected by the varying TF ripple. An orbit-following Monte Carlo code, ASCOT, was used to determine the TF ripple induced losses of NBI ions, the details of which are described in [22]. In this way it was possible to calculate the fraction of NBI power that was lost and how much toroidal torque was induced due to the TF ripple losses. For TF ripple values up to $\delta_{B_T} = 1.0\%$, the dominant contribution to the TF ripple induced torque is due to its effect on fast ions, injected by NBI, and trapped in banana-orbits and not those actually trapped in the TF ripple [15]. ASCOT analysis has shown that the fraction of particles trapped in the TF ripple is negligible. The torque due to the TF ripple is directed in the counter-current direction and hence opposes the co-current NBI torque. In the calculation of the torque deposition used in this paper, only the effect of the TF ripple on fast ions has been considered.

In figure 1, the power loss fraction and the TF ripple induced total torque, as calculated by ASCOT, are plotted as a function of TF ripple amplitude for all discharges used in this study. It can be seen that for $\delta_{B_T} = 1.0\%$ approximately 20–25% of all NBI power is not absorbed in the plasma but deposited on plasma-facing components. The effect on the rotation will be more pronounced, as the TF ripple induced torque for $\delta_{B_T} = 1.0\%$ is of the same magnitude as, but opposing, the torque supplied by the NBI. Hence the net torque on the plasma for this TF ripple amplitude is near zero. This does not mean that the entire plasma experiences a counter-current torque. In figure 2(a) the total torque deposition profiles as calculated by ASCOT are

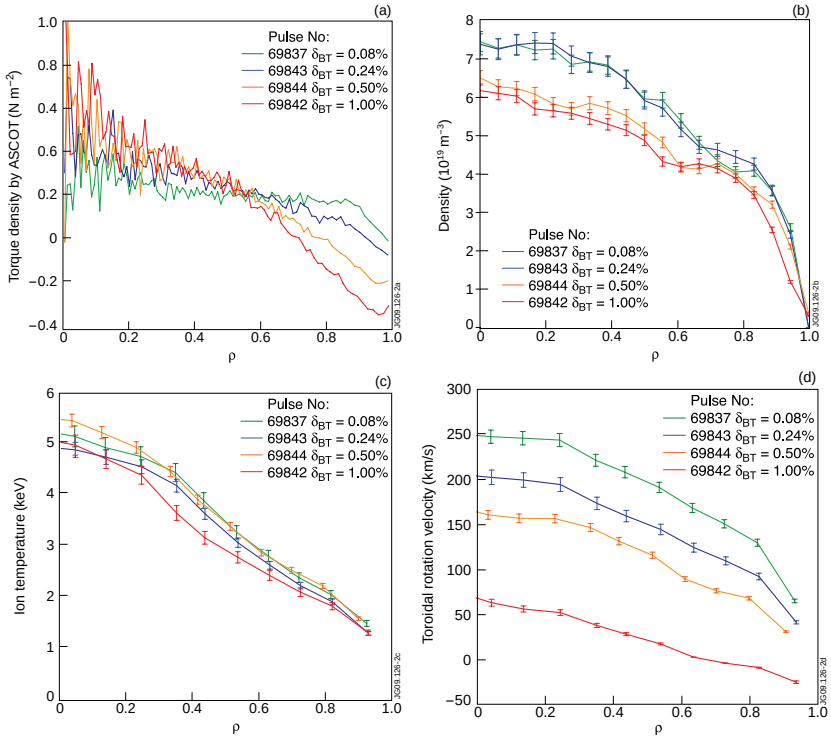

Figure 2. (*a*) The torque deposition profiles as calculated by ASCOT for four similar discharges but with different TF ripple amplitudes. (*b*) The corresponding density profiles measured by the LIDAR Thomson scattering diagnostic. (*c*) The ion temperature profiles measured by CXRS. (*d*) The toroidal rotation profiles measured by the same diagnostic.

shown for four discharges with different TF ripple amplitudes. The increased TF ripple causes a region with counter-current torque near the outer part of the plasma. However, the torque deposited in the core ($\rho < 0.5$) is largely unaffected. Actually, in order to compensate for the TF ripple induced power losses and keep the total absorbed power constant, the requested NBI power was often higher for the higher TF ripple cases, resulting in a higher torque density in the core.

For the same four discharges the electron density, measured by the LIDAR Thomson scattering diagnostic, and ion temperature and toroidal rotation, measured by charge exchange spectroscopy (CXS), are shown in figures 2(*b*)–(*d*). The profiles are plotted versus the normalized radius, ρ. As has been reported earlier, the increase in TF ripple affected the density profiles by lowering the density [20]. The pulses with the highest TF ripple had a lower stored energy ($\beta_N = 1.7$) as well as a lower ν^*. The core ion temperature profiles seem unaffected by the changes in TF ripple, while it has a strong effect on the rotation profiles. Not only does the increase in TF ripple push the plasma rotation at the edge in the counter-current direction, the gradient of the rotation profile is reduced significantly (by approximately a factor 4 from $\delta_{B_T} = 0.08\%$ up to 1.0%). Such a large reduction in rotation gradient and lower

momentum density, while the deposited torque inside $\rho < 0.5$ is actually larger, suggests that the momentum transport differs strongly for these cases.

3. Momentum transport properties

Experiments have shown that TF ripple affects the plasma performance, mainly by a change in the H-mode pedestal [19, 20]. However, its effect on the plasma rotation and momentum transport seems to be significantly larger. This paper will not deal with the detailed effects of TF ripple on the general plasma performance but will compare the momentum transport with the energy transport properties of these discharges.

In order to determine the effective momentum, χ_ϕ^{eff}, and ion heat, $\chi_{\text{i}}^{\text{eff}}$, diffusivities, both the gradients and the sources have to be determined using steady-state power and momentum balance equations, assuming purely diffusive transport:

$$Q_{\text{i}} = -\chi_{\text{i}}^{\text{eff}} n \nabla T_{\text{i}}, \tag{1}$$

$$\Gamma_\phi = -\chi_\phi^{\text{eff}} \nabla \Omega, \tag{2}$$

where Q_{i} is the ion heat flux, Γ_ϕ is the torque flux (i.e. the amount of torque deposited within a certain region divided by the surface), as determined by the ASCOT code, and ∇T_{i}, $\nabla\Omega$ are the gradients in the ion temperature and momentum density, respectively. To begin with, all values are calculated at mid-radius ($\rho = 0.5$) averaged over the gradient region from $\rho = 0.3$–0.7. In order to further reduce the error bars on the gradients, the profiles have been averaged over a large time window of 2 s in which the plasmas were in quasi-steady state. Nevertheless, the error in the diffusivities was still of the order of 30%. It was found that the heat diffusivity varied from $0.92\,\text{m}^2\,\text{s}^{-1} < \chi_{\text{i}}^{\text{eff}} < 1.8\,\text{m}^2\,\text{s}^{-1}$ although for most discharges the value was close to the average of $\chi_{\text{i}}^{\text{eff}} = 1.3\,\text{m}^2\,\text{s}^{-1}$. The variation in core heat diffusivity may be attributed to the changes in density between the pulses. However, a much larger variation was found for the effective momentum diffusivity. The Prandtl number, P_r, can be used to compare the relative changes between both diffusivities. The effective Prandtl number is defined as

$$P_r^{\text{eff}} = \frac{\chi_\phi^{\text{eff}}}{\chi_{\text{i}}^{\text{eff}}}. \tag{3}$$

In figure 3 it can be seen that for low TF ripple amplitudes, again effective Prandtl numbers of about 0.2–0.3 are found, similar to standard JET discharges [3, 4], but this increases to around unity when the TF ripple is increased to $\delta_{B_{\text{T}}} = 1.0\%$.

Although the TF ripple affects the torque on the plasma, its effect for an amplitude of $\delta_{B_{\text{T}}} = 1.0\%$ only reaches up to $\rho > 0.6$ as can be seen from figure 2(*a*). As mentioned above, the torque deposited in the core ($\rho < 0.5$) slightly increases with TF ripple for this dataset. Hence it is not the momentum source that is changing with TF ripple but the effective diffusivity that flattens the rotation profiles as seen in figure 2(*d*). The increase in TF ripple results in a reduction in edge rotation. If the effective Prandtl number is plotted versus the rotation, as shown in figure 3(*b*), the trend suggests that with a larger rotation in the outer part of the plasma, one will have a smaller effective Prandtl number. The effective momentum diffusivity is increased with respect to the heat diffusivity, when a larger TF ripple results in a smaller momentum in the outer part of the plasma.

Besides looking at the local diffusivities, one can compare the global energy and momentum confinement times. Here, the energy confinement time is defined as the total integrated kinetic energy divided by the absorbed power, while the momentum confinement time is the total angular momentum divided by the total torque on the plasma. The ratio of the

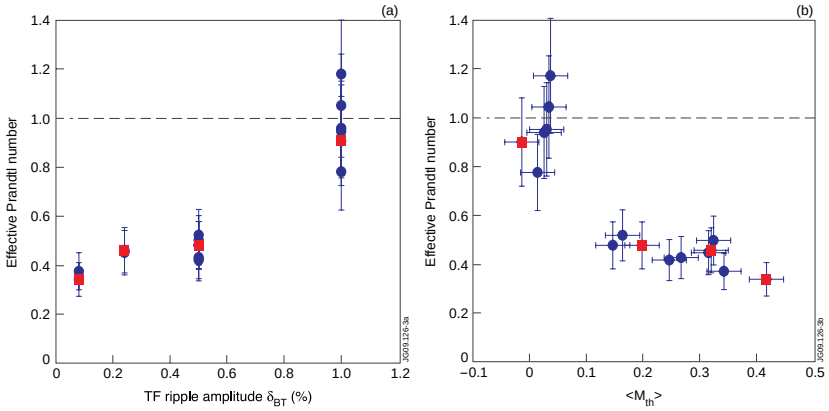

Figure 3. (*a*) The effective Prandtl number versus the TF ripple amplitude. (*b*) The effective Prandtl number versus average thermal Mach number at $\rho = 0.55$. The four discharges from figure 2 are marked by the red squares.

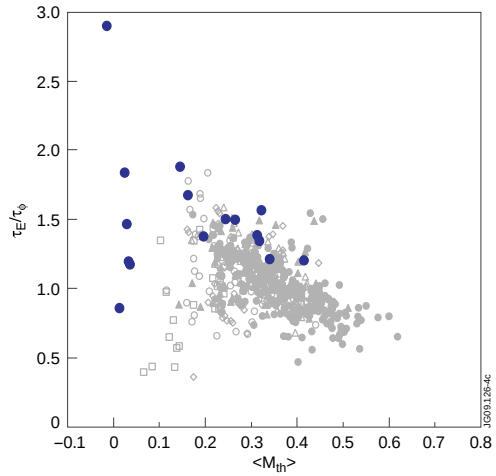

Figure 4. The ratio of the energy and momentum confinement time versus the average thermal Mach number for these TF ripple H-mode discharge (blue dots). The Mach number decreases for increasing TF ripple. In grey the points are from the JET rotation database as in figure 8(*c*) in [4].

two is plotted in figure 4 versus the average thermal Mach number similarly as in figure 8(*c*) of [4]. The thermal Mach number is determined by normalizing the plasma velocity to the thermal velocity [4]. The data follow the main trend found in the JET rotation database: the ratio of energy and momentum time increases with decreasing average Mach number. The energy and momentum confinement time are approximately equal for those discharges with a low TF ripple. However, for the high TF ripple cases, and low to zero edge rotation, the momentum confinement time worsens and is found to be much smaller than the energy confinement.

The momentum confinement time for discharges with TF ripple of $\delta_{B_T} = 1.0\%$ shows a large variation. This causes the break in the trend seen in figure 4, where the ratio for the low Mach number cases seems to be lower. This may be due to an inaccuracy in the calculated torque on these plasmas. For these TF ripple amplitudes, the ripple induced counter-current torque approaches that supplied by the NBI system, resulting in a near zero net torque on the plasma. The data suggest that this net torque, as determined by ASCOT, may be slightly overestimated (roughly by 2–4 N m). Similar issues have been presented when operating with balanced NBI in DIII-D with the suggestion of the presence of an intrinsic torque [18]. The discrepancy shown here could be attributed to differences in the levels of rotation in Ohmic plasmas at larger TF ripple [23] or possibly thermal ion losses [15] or neo-classical toroidal viscosity [24] which is not included in the ASCOT calculations of the torque. Larger TF ripples may also affect thermal particle orbits, enhancing the neo-classical toroidal viscosity [24]. This effect was estimated for two discharges with a TF ripple of $\delta_{B_T} = 1.0\%$, and 0.5%, using the equations in [24] and found to depend strongly on $Z_{\rm eff}$. The torque due to neo-classical viscosity was of the order of about 3 N m for $Z_{\rm eff} \sim 1.5$. But because it is always difficult to accurately determine the effective charge of the plasma, a rather large uncertainty remains.

4. Estimation of the effect of the momentum pinch

Usually the effective Prandtl number in JET H-mode discharges is well below unity. Here the effective momentum diffusivity was found to increase with respect to the ion heat diffusivity when the (edge) rotation was reduced due to the larger TF ripple. The question is, however, whether momentum transport is purely diffusive. The observations can be explained by including an inward convection term to the momentum transport as

$$\Gamma_\phi = -\chi_\phi \nabla\Omega - V_{\rm p}\Omega. \tag{4}$$

Here the symbols Ω and $\nabla\Omega$ represent the momentum density and its gradient, $V_{\rm p}$ is the inward pinch velocity. One may question whether one has to take into account possible intrinsic sources by adding an additional term in equation (4), independent of the velocity or its gradient. This may originate from, for example, residual stress [25] or up–down asymmetries in the equilibrium [26]. The latter may be of less relevance because of the symmetric, low triangularity, plasma configurations used in these experiments. In any case at JET the intrinsic rotation is usually at least one order of magnitude smaller than that in predominantly NBI heated discharges [4, 27]. Hence in equation (4) a possible intrinsic momentum flux, independent of the velocity or its gradient, could be neglected with respect to the flux supplied by NB (Γ_ϕ). The momentum diffusivity, χ_ϕ, contrasts with the effective momentum diffusivity, $\chi_\phi^{\rm eff}$, calculated by equation (2). The presence of an inward convection reduces the effective momentum diffusivity $\chi_\phi^{\rm eff}$ with respect to χ_ϕ [27]. It is clear from equation (4) that a smaller momentum density Ω (in the outer part of the plasma) would reduce the inward convection flux. Hence, in these cases, such as with a large TF ripple ($\delta_{B_T} \sim 1.0\%$), $\chi_\phi^{\rm eff}$ may approach χ_ϕ which may be similar to $\chi_{\rm i}$. While when a significant inward convection is present one obtains an effective Prandtl number smaller than unity. This is indeed what was found in figure 3. Similarly a reduction in the inward convection term (by increasing the TF ripple) will result in a lower momentum confinement time with respect to that of the energy as found in figure 4.

$V_{\rm p}\Omega$ is a parameter that can be indirectly altered by the TF ripple. One can rewrite equation (4) by normalizing it by Γ_ϕ the torque flux, removing the variations in the central deposited torque from discharge to discharge. Because of the small values of Ω in the discharges

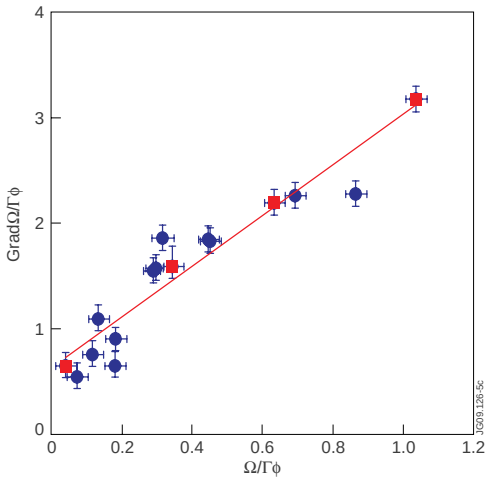

Figure 5. The normalized gradient, $\nabla\Omega/\Gamma_\phi$, for the series of discharges in which the TF ripple was varied between $\delta_{B_T} = 0.08$ and 1%, plotted versus the normalized momentum density, Ω/Γ_ϕ. The red line is a fit through the data points with a slope of 2.19 and an off-set of 0.66. The four discharges from figure 2 are marked by the red squares.

with a high TF ripple, normalization by Ω was found to be impractical. This gives

$$\frac{\nabla\Omega}{\Gamma_\phi} = -\frac{V_p}{\chi_\phi}\frac{\Omega}{\Gamma_\phi} - \frac{1}{\chi_\phi}. \tag{5}$$

In figure 5 the above equation has been plotted for the 16 discharges. As before, these parameters have been determined at $\rho = 0.5$ averaged from $\rho = 0.3$–0.7. The normalized gradient, $\nabla\Omega/\Gamma_\phi$, clearly scales with the normalized momentum density Ω/Γ_ϕ. Note that according to equation (2) the normalized gradient on the y-axis is also equal to χ_ϕ^{eff}. The slope is determined by the magnitude of the pinch velocity, while the off-set is equal to $1/\chi_\phi$. This gives an estimate of the average pinch velocity and momentum diffusivity of this set of discharges. An important parameter is the average normalized pinch velocity, $RV_p/\chi_\phi \sim 6.6$, where R is the major radius, which can be compared with the theoretical predictions [5]. The average pinch velocity was found to be $\langle V_p\rangle = 3.4\pm0.2\,\text{m s}^{-1}$, while the average momentum diffusivity was $\chi_\phi = 1.5 \pm 0.2\,\text{m}^2\,\text{s}^{-1}$. The latter parameter is close to the average ion heat diffusivity of $\chi_i^{\text{eff}} \sim 1.3\,\text{m}^2\,\text{s}^{-1}$ for these discharges. Hence the diffusive transport of momentum was found to be approximately the same as the energy diffusivity as predicted by gyro-kinetic calculations. As was pointed out above, there is some variation from discharge to discharge and it is likely that this is the same for momentum. Nevertheless, the data from figure 5 give an estimate of the average momentum pinch and diffusivity to explain the changes in the rotation profiles with varying TF ripple. It should be pointed out that the near zero values of Ω or $\langle M_{\text{th}}\rangle$ are obtained at $\rho = 0.5$, with the outer part rotating in the counter-current direction while the core rotates in the same direction of the plasma current (and NBI injection).

The above analysis provides a profile averaged momentum pinch over the gradient region of the plasmas. In order to get an idea of the radial profile of the pinch velocity one can redo the analysis for a smaller inner region (i.e. $\rho = 0.10$–0.45) and an outer region (i.e. $\rho = 0.65$–0.90), albeit increasing the error in the determination of the gradients. As shown in figure 6, the slope and thus also the normalized momentum pinch for the outer region are close

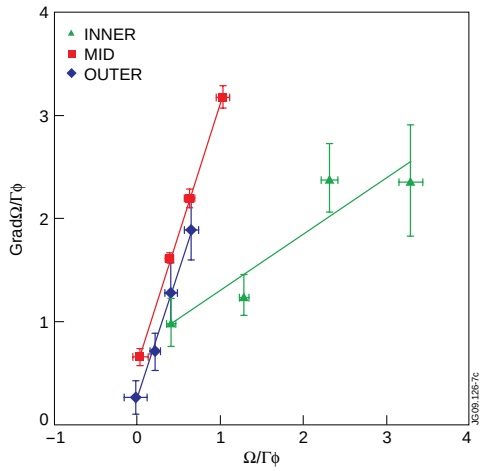

Figure 6. The normalized gradient, $\nabla\Omega/\Gamma_\phi$, for the four discharges in which the TF ripple was varied between $\delta_{B_T} = 0.08$ and 1%, plotted versus the normalized momentum density, Ω/Γ_ϕ. The red squares show the similar analysis as in figure 5, using gradients averaged over the mid-region of the plasma ($\rho = 0.4$–0.8), while the green triangles and blue diamonds are calculated for an inner ($\rho = 0.10$–0.45) and outer ($\rho = 0.65$–0.90) region, respectively.

to the averaged value found for the entire (mid) gradient region, with $RV_p/\chi_\phi \sim 7.5$, while the off-set is lower, indicating a larger diffusivity, of $\chi_\phi = 4 \pm 0.6\,\mathrm{m^2\,s^{-1}}$. The normalized pinch for the inner region is significantly smaller, $RV_p/\chi_\phi \sim 1.6$ with a value for the diffusivity of $\chi_\phi = 1.3 \pm 0.3\,\mathrm{m^2\,s^{-1}}$. Thus, near the outer part of the plasma the momentum pinch velocity is of the order of $V_p = 10\,\mathrm{m\,s^{-1}}$ and this value decreases towards the plasma centre, a profile similar to that found in previous experimental results [11].

A detailed database to study the scaling of rotation and momentum transport in JET discharges has been created [4]. The database contains entries from various operational scenarios, such as type I and III ELMy H-modes or plasmas with internal transport barriers (ITBs) for which the average rotation and momentum source and transport properties are determined in steady-state phases of the discharge. All the entries have a standard TF ripple ($\delta_{B_T} = 0.08\%$) and generally effective Prandtl numbers considerably less than unity. If one considers the observations in the TF ripple experiments and assumes the presence of an inward momentum pinch and that $\chi_\phi \equiv \chi_i^{\mathrm{eff}}$, one can estimate the magnitude of such a pinch by rewriting equations (2), (3) and (4) as

$$\frac{V_p}{\chi_i^{\mathrm{eff}}} \approx (1 - P_r^{\mathrm{eff}})\frac{\nabla\Omega}{\Omega}. \tag{6}$$

Using this equation the normalized momentum pinch, RV_p/χ_ϕ, was calculated for all database entries, averaged over $\rho = 0.3$–0.7, as shown in figure 7. Higher values are found in discharges with more peaked density profiles (i.e. a larger R/L_n). The magnitude and scaling are close to the one predicted by the theory [5]: $RV_p/\chi = 4 + (R/L_n)$. The normalized momentum density gradient ($\nabla\Omega/\Omega$) used in equation (6) was found to be predominantly determined by the gradient in the rotation profile, and the density gradient played only a minor role. Figure 7 gives an idea of the levels of the average momentum pinch in JET plasmas. The values found for the TF ripple experiments match nicely within the other H-mode entries in the database.

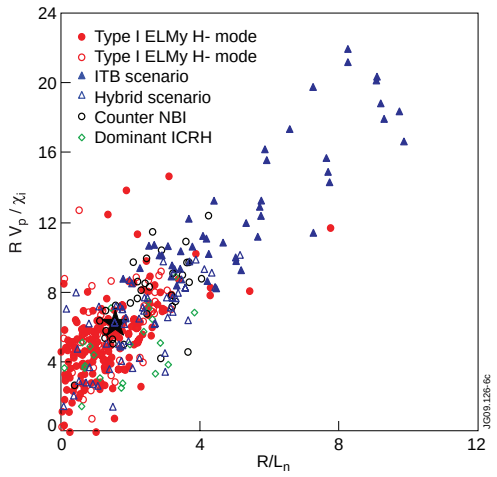

Figure 7. The normalized pinch velocity $RV_{\rm p}/\chi_{\rm i}$ calculated for the entire JET rotation database [4] for various operational scenarios, under the assumption that $\chi_\phi = \chi_{\rm i}$ plotted versus the normalized inverse density gradient length $R/L_{\rm n}$. Note that all parameters in the JET rotation database are determined at $\rho = 0.5$ (averaged from $\rho = 0.2$–0.7). The black star gives the result obtained from the analysis of the TF ripple experiments.

5. Conclusions

Previously the presence of a momentum pinch has been deduced from various experiments [10–13]. It should be said that the power balance analysis presented here does not independently prove the presence of such a pinch. Nevertheless, it was shown that an inward convection component in the momentum transport equation would nicely explain the behaviour of the rotation profiles when the TF ripple was enhanced and the edge rotation was reduced. Moreover, effective Prandtl numbers increased to values close to unity when the inward convection was significantly reduced. This indicates that the small effective Prandtl numbers found in standard JET discharges are caused by the smaller effective momentum transport due to the inward momentum convection. It also explains why in JET the ratio of the energy and momentum confinement scaled with the rotation itself. The experiments clearly showed the significant impact of the momentum pinch on the toroidal rotation profiles in JET H-mode discharges.

The profile average pinch velocity that explained the effects found in these H-mode discharges was $V_{\rm p} = 3.4\,{\rm m\,s^{-1}}$ which is smaller than the maximum found in detailed torque modulation experiments [11]. However, the experimental parameters (e.g. density, heating power and q-profile) differed between these experiments. The density in these H-mode discharges was significantly higher and the heat diffusivity lower than in the modulation experiments. A better comparison would be the normalized pinch velocity, that was found to be $RV_{\rm p}/\chi_\phi \sim 6.6$, which is close to the earlier experiments at JET. Moreover, the magnitude and the observed scaling with the density gradient length match well the theoretical predictions [5].

An estimation of the momentum pinch was made for all entries in the JET rotation database by assuming that $\chi_\phi \approx \chi_{\rm i}$ and the difference between the measured $\chi_\phi^{\rm eff}$ and $\chi_{\rm i}^{\rm eff}$ is due to the momentum pinch. This shows similar values as found from the analysis of the TF

ripple experiments, for H-mode discharges ranging from $0.3\,\mathrm{m\,s^{-1}} < V_\mathrm{p} < 17\,\mathrm{m\,s^{-1}}$, with approximately $2 < RV_\mathrm{p}/\chi < 10$. An increasing trend with the peaking of the density profile was found.

It is interesting to note that for discharges with no or little rotation at the edge the effective diffusivities of heat and momentum were approximately equal in the core, but the momentum confinement time was more than a factor of 2–3 times less than that of the energy. The fact that the transport of energy and momentum in the core is the same, while the global confinement is different, suggests that the edge may have different impacts on the confinement of momentum than on the energy. This could be due to a difference in transport properties, additional drag or losses near the edge of the plasma. These are factors that need to be understood when one would like to accurately predict rotation levels in ITER as the edge rotation may affect the whole profile.

Acknowledgments

This research has been performed under the European Fusion Development Agreement and was partly funded by the Culham Centre for Fusion Energy, the UK Engineering and Physical Sciences Research Council and by the European Communities under contract of association between EURATOM and CCFE. The views and opinions expressed herein do not necessarily reflect those of the European Commission.

References

[1] Scott S D *et al* 1990 *Phys. Rev. Lett.* **64** 531
[2] Mattor N and Diamond P 1988 *Phys. Fluids* **31** 1180
[3] de Vries P C *et al* 2006 *Plasma Phys. Control. Fusion* **48** 1693
[4] de Vries P C *et al* 2008 *Nucl. Fusion* **48** 065006
[5] Peeters A G, Angioni C and Strintzi D 2007 *Phys. Rev. Lett.* **98** 265003
[6] Hahm T S *et al* 2007 *Phys. Plasmas* **14** 072302
[7] Nagashima K *et al* 1994 *Nucl. Fusion* **34** 449
[8] Ida K *et al* 1995 *Phys. Rev. Lett.* **74** 1990
[9] Lee W D *et al* 2003 *Phys. Rev. Lett.* **91** 205003
[10] Yoshida M *et al* 2007 *Nucl. Fusion* **47** 856
[11] Tala T *et al* 2009 *Phys. Rev. Lett.* **102** 075001
[12] Kaye S M *et al* 2009 *Nucl. Fusion* **49** 045010
[13] Solomon W M *et al* 2009 *Nucl. Fusion* **49** 085005
[14] Zastrow K-D *et al* 1998 *Nucl. Fusion* **38** 257
[15] de Vries P C *et al* 2008 *Nucl. Fusion* **48** 035007
[16] Rice J E *et al* 2004 *Nucl. Fusion* **44** 379
[17] Rice J E *et al* 2007 *Nucl. Fusion* **47** 1618
[18] Solomon W M *et al* 2007 *Plasma Phys. Control. Fusion* **49** B313
[19] Oyama N *et al* 2008 *J. Phys. Conf. Ser.* **123** 012015
[20] Saibene G *et al* 2008 *Proc. 22nd Int. Conf. on Fusion Energy 2008 (Geneva, Switzerland, 2008)* (Vienna: IAEA) CD-ROM file EX/2-1 http://www-naweb.iaea.org/napc/physics/ FEC/FEC2008/papers/ex_2-1.pdf
[21] Yoshida M *et al* 2006 *Plasma Phys. Control. Fusion* **48** 1673
[22] Salmi A *et al* 2008 *Contrib. Plasma Phys.* **48** 77
[23] Nave M F F *et al* 2009 *Proc. 36th EPS Conf. on Plasma Physics (Sofia, Bulgaria)* vol 33E (ECA) P-2.168 http://epsppd.epfl.ch/Sofia/ pdf/P2_168.pdf
[24] Cole A J, Hegna C C and Callen J D 2008 *Phys. Plasmas* **15** 056102
[25] Diamond P H *et al* 2009 *Nucl. Fusion* **49** 045002
[26] Camenen Y *et al* 2009 *Phys. Rev. Lett.* **102** 125001
[27] Tala T *et al* 2007 *Plasma Phys. Control. Fusion* **49** B291

PUBLICATION V

NBI torque in the presence of magnetic field ripple: experiments and modelling for JET

In: Plasma Physics and Controlled Fusion 53,
085005 (20 pp), 2011.

http://iopscience.iop.org/0741-3335/53/8/085005/
pdf/0741-3335_53_8_085005.pdf

Plasma Phys. Control. Fusion **53** (2011) 085005 (20pp) doi:10.1088/0741-3335/53/8/085005

NBI torque in the presence of magnetic field ripple: experiments and modelling for JET

A T Salmi[1], T Tala[2], G Corrigan[3], C Giroud[3], J Ferreira[4], J Lönnroth[1], P Mantica[5], V Parail[3], M Tsalas[6], T W Versloot[6], P C de Vries[6], K-D Zastrow[3] and EFDA JET Contributors[7]

JET-EFDA, Culham Science Centre, Abingdon, OX14 3DB, UK
[1] Aalto University, Association Euratom-Tekes, Helsinki, Finland
[2] VTT, Association Euratom-Tekes, Helsinki, Finland
[3] EURATOM/CCFE Fusion Association, Culham Science Centre, Abingdon, UK
[4] Associação EURATOM/IST, Centro de Fusão Nuclear, 1049-001 Lisbon, Portugal
[5] Istituto di Fisica del Plasma, Euratom-ENEA-CNR Association, Milan, Italy
[6] FOM Institute Rijnhuizen, Association EURATOM-FOM, Nieuwegein, the Netherlands

Received 5 January 2011, in final form 30 March 2011
Published 19 May 2011
Online at stacks.iop.org/PPCF/53/085005

Abstract
Accurate and validated tools for calculating toroidal momentum sources are necessary to make reliable predictions of toroidal rotation for current and future experiments. In this work we present the first experimental validation of torque profile calculation from neutral beam injection (NBI) under toroidal field ripple. We use discharges from a dedicated experimental session on JET where neutral beam modulation technique is used together with time-dependent torque calculations from ASCOT code for making the benchmark. Good agreement between simulations and experimental results is found.

(Some figures in this article are in colour only in the electronic version)

1. Introduction

Toroidal momentum transport and rotation have been very active research topics in the last years. Toroidal rotation and rotation shear have been shown to improve confinement [1] and to increase the stability against resistive wall modes [2] of fusion plasmas. Recently it has been shown, both theoretically [3, 4] and experimentally [5–8], that inside the plasma pedestal, momentum transport is not purely diffusive but that a convective (pinch) term also exists. Inward momentum pinch may help to achieve a peaked rotation profile in ITER, even with just small external torque sources or with other seed rotation sources at the plasma edge [9].

[7] See the appendix of Romanelli F *et al* 2010 *Proc. 23rd IAEA Fusion Energy Conf. 2010 (Daejon, Korea)*.

One important ingredient in predicting rotation in ITER is the capability to calculate the torque generated by the neutral beam injection (NBI) under toroidal magnetic field ripple. Even with the ripple compensating ferromagnetic inserts included in the design, the expected ripple magnitude $\delta = (B_{\max} - B_{\min})/(B_{\max} + B_{\min})$ in the full field will be $\delta \sim 0.35\%$, which although shown to be acceptable in terms of fast ion energy losses [10], may still cause a significant counter-current torque contribution via non-ambipolar radial diffusion of fast ions. In recent JET experiments [11] with enhanced ripple ($\delta \sim 1\%$), the plasma edge was found to counter-rotate with co-current NBI while similar plasmas with smaller ripple were co-rotating. It was found that, taking into account the NBI torque modification due to the ripple, the observations could be largely explained. In rippled Ohmic plasmas in JET, counter-current torque contribution due to ripple has also been observed, although the level of rotation has been small compared with NBI heated discharges [12].

Non-axisymmetric magnetic perturbations, such as toroidal field ripple, can lead to non-ambipolar radial transport of not only fast ions but also of thermal ions giving rise to the so-called neoclassical toroidal viscosity (NTV) torque, see, e.g., a recent review [13] and references therein. Plasma breaking, associated with NTV, has indeed been observed experimentally on several tokamaks, e.g. DIII-D and JET using low toroidal harmonic magnetic perturbations. Toroidal field ripple, on the other hand, has a weak radial component, which decays rapidly towards the plasma centre. The associated NTV torque, whether small or large, is expected to be edge localized. It is assumed that in the discharges analysed here NBI is the dominant *core* torque source and other possible torque sources such as the NTV or the residual stress [14] are neglected.

While ripple diffusion and trapping are well understood theoretically and experimentally [15–19], the rigorous validation of fast ion ripple torque calculations against experimental data is still lacking. Numerous earlier studies on ripple losses [20, 21], fast ion neutron yield [22, 23] and prompt momentum balance [24] already indirectly suggest that guiding centre following codes should be capable of this task also with ripple. In previous works from the JET ripple campaign [11, 25], the ripple induced fast ion losses and torque have, indeed, been identified as the likely candidate to explain the observed reduction in rotation. However, without detailed knowledge of the momentum transport in the discharges, only rough estimates of the total torque can be obtained. For validating the torque calculations in the presence of ripple, dedicated experiments are required in which both the diffusive and convective momentum transport (χ_ϕ and v_{pinch}) and the effect of ripple on NBI torque can be resolved simultaneously.

In this work, discharges from the JET enhanced ripple session designed for benchmarking the NBI torque calculations in the presence of toroidal field ripple are analysed. The guiding centre following Monte Carlo code ASCOT [26] is used for the torque calculations. ASCOT has been used for fast ion loss calculations with ripple in, e.g., [27, 28] but has not yet been experimentally validated for the torque.

The rest of the paper is organized as follows. First, the experimental set-up is described and a justification for the assumption of an identical and stationary momentum transport between the discharges is given. This is followed by a description of the plasma response to the applied NBI torque and power modulation. Section 3 is dedicated for code-to-code benchmarking. ASCOT is first briefly described, after which the comparisons against OFMC [19, 29] and NUBEAM (inside the TRANSP transport code) [30] are presented. In Section 4, the time-dependent NBI torque profiles from ASCOT are reviewed, and compared against the experimental rotation data in Fourier space at the modulation frequency. Section 5 describes the optimization scheme used to evaluate the momentum transport coefficients, and presents the comparison between the simulated toroidal rotation, using torque from ASCOT, and the experimental data. Finally, the results are discussed and conclusions of the work are drawn in section 6.

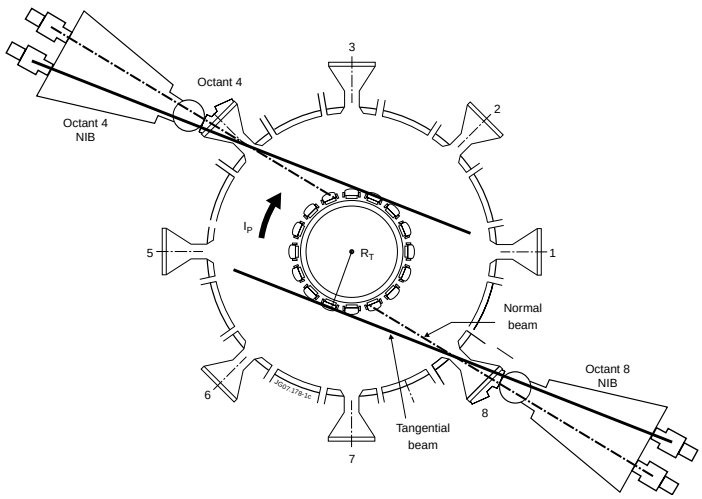

Figure 1. Top view of the JET NBI system. The toroidal field is in the same direction as the current.

2. Experimental set-up

The NBI system at JET [31] consists of a total of 16 units each capable of delivering roughly 1–1.5 MW of power and 1–1.5 Nm of torque depending on the voltage and injection angle used. Half of the units are aligned with a tangency radius of $R_{\mathrm{T}} = 1.31$ m (normal injection) while the rest have a tangency radius of $R_{\mathrm{T}} = 1.85$ m (tangential injection) in the usual co-current direction, see figure 1. The major radius of the JET torus is $R_0 = 2.95$ m. NBI acceleration voltages can be adjusted in the range 60–130 kV as required by the experiment. NBI power can also be turned on and off relatively reliably thus lending itself to transport studies utilizing modulation techniques [32, 33].

A set of discharges was selected for this study (77089, 77090 and 77091), characterized by L-mode confinement and hence a relatively low density ($n_{\mathrm{e0}} \approx 3 \times 10^{19}\,\mathrm{m}^{-3}$) and low temperature ($T_{\mathrm{e0}} \approx T_{\mathrm{i0}} \approx 3$ keV), and all with a plasma current of $I_{\mathrm{p}} = 1.5$ MA and the average central toroidal field $B_0 = 2.2$ T ($q_{95} = 5$). The three discharges did not exhibit MHD activity. In each discharge two 90 keV NBI units (total of 2.5 MW) are injected continuously to collect ion temperature and toroidal rotation data and to keep that plasma relatively stationary during the experimental window. Additionally, two/three modulated 65 keV units (≈4.5 MW) are used with a duty cycle of 50/110 ms (on/off). The modulation cycle is short enough to avoid reaching steady state yet long enough to yield plasma rotation modulation sufficiently large to make the analysis. Discharge 77089 is the reference without ripple and with normal NBI modulation (3 units). 77090 is identical to 77089 but operated with 1.5% toroidal field ripple. 77091 is again a similar discharge with ripple, but with modulation from tangential NBI units (2 units).

Figure 2 shows time traces of a number of important plasma and heating parameters for the reference discharge 77089 with small ripple ($\delta = 0.08\%$). The time interval is the same which is used for transport and torque analysis as well as for the Fourier analysis of the experimental

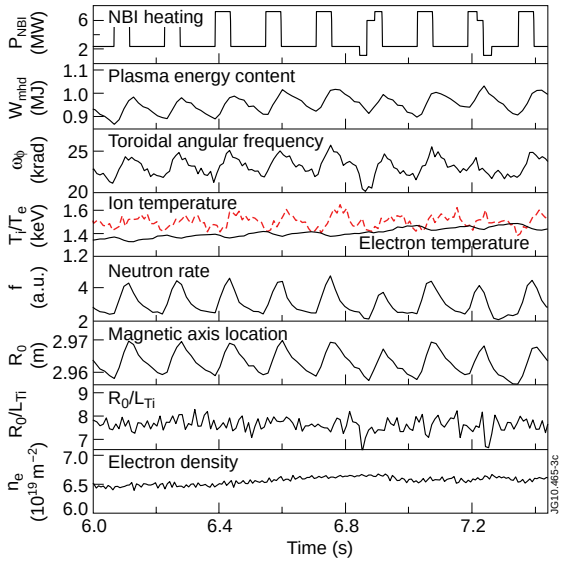

Figure 2. Time traces of plasma and heating parameters over the time interval of interest for 77089. Temperature and rotation values are taken near plasma midradius and magnetic axis from EFIT [35] reconstruction.

profiles. One can observe that all the chosen quantities are modulated with the NBI, except the electron density and the normalized inverse temperature scale length, $R_0/L_{T_\mathrm{i}} = R_0\nabla T_\mathrm{i}/T_\mathrm{i}$. The highest fractional increase is seen in the total neutron rate which is dominated by the beam thermal D–D fusion. Other quantities are dominated by the changes in the bulk plasma and therefore fluctuate significantly less. A more detailed investigation across the radius shows that the ion and electron temperature modulations remain at a moderate 2–5% level, while the toroidal rotation fluctuation can reach levels up to 10%.

In general, the radial momentum transport is proportional to heat transport [34]. In these low performance L-mode plasmas the main driver of the momentum transport is the ITG turbulence. As seen in figure 2, the electron density stays constant and does not modulate with the NBI (negligible fuelling effect). Furthermore, the small ion temperature fluctuation is compensated by the accompanying ∇T_i fluctuation, and the temperature scale length, L_{T_i}, is practically uncorrelated with the modulation. These give a good indication that the local momentum transport stays independent of the NBI modulation throughout the experiment. Therefore, we can simplify the subsequent analysis by assuming constant transport (in time) and keep the momentum transport coefficients fixed during the time interval of interest.

This approximation is also supported by the previous work [33, section IV.A2], where the effect of the fluctuating energy diffusion χ_i due to T_i oscillations was studied. It was found that for small T_i amplitudes the rotation response of the plasma did not change significantly when the fluctuations in χ_i were included in the analysis.

The similarity of the plasmas across the discharges is seen in figure 3, where the experimental steady-state profiles are plotted for the discharges 77089–77091. Ion and electron temperature profiles as well as the q-profiles are practically the same for all the plasmas and the

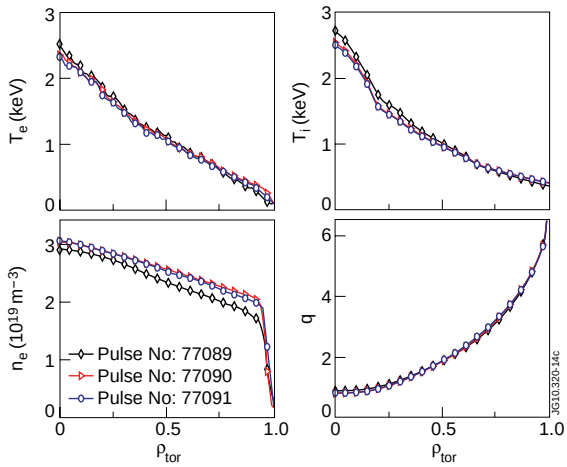

Figure 3. Time averaged plasma and q-profiles over 9 modulation cycles between 46.0–47.44 s for the discharges 77089 (diamond), 77090 (triangle) and between 47.0–48.44 s for 77091 (circle).

difference in electron density between the high ripple discharges and the reference discharge is below 10%. Based on the similar profiles among the three discharges we assume that the transport of momentum is the same between them, and that the difference in the rotation is due to the difference in the torque source. More precisely, we assume that the Prandtl number, $Pr = \chi_\phi/\chi_\mathrm{i}$, and the pinch velocity, v_pinch, are equal between the discharges. This should be a reasonable assumption for the Prandtl number since the variation in electron density should affect the χ_ϕ and χ_i in the same way. To estimate the sensitivity of the v_pinch on the density we can use the experimental scaling, $Rv_\mathrm{pinch}/\chi_\phi \approx 1.2R/L_n + 1.4$ [9]. Dividing the formula by parts and substituting experimental values we find that for $\rho_\mathrm{tor} < 0.8$ the ratio $v_\mathrm{pinch,77089}/v_\mathrm{pinch,77090}$ is between 0.9 and 1.1. The experimental estimate of the pinch velocity sensitivity is less than the error we get in the transport analysis.

In addition to the plasma properties, the location of the magnetic axis is modulated due to the NBI driven change in the plasma pressure. In fact the whole plasma moves almost rigidly. During the high power phase the magnetic axis moves about 1 cm, and the separatrix 8 mm, towards the low-field side. The equilibrium modulation combined with radial gradients in the profiles can generate spurious components in signals which are collected along fixed lines of sight. A simple estimation, using the 5 mm radial modulation and the gradients involved, shows that this could contribute about 5–20% to the modulation amplitudes if not subtracted in an appropriate way. In the following we eliminate this effect by mapping the data into time-independent flux surface coordinates prior to the analyses.

A further complication coming from the equilibrium modulation is the change in the ripple magnitude at a given flux surface (see figure 4). The radial decay length of the ripple magnitude at separatrix is about $\lambda_\mathrm{r} = 25$ cm which for the 8 mm displacement results in a 3% change in the effective ripple magnitude. To quantify how big a difference it makes on the torque, we have run ASCOT at both extremities to find that the counter-current torque is increased by ∼3% when the ripple is larger. Due to the smallness of this effect we neglect it and for simplicity fix the equilibrium for the whole analysis period.

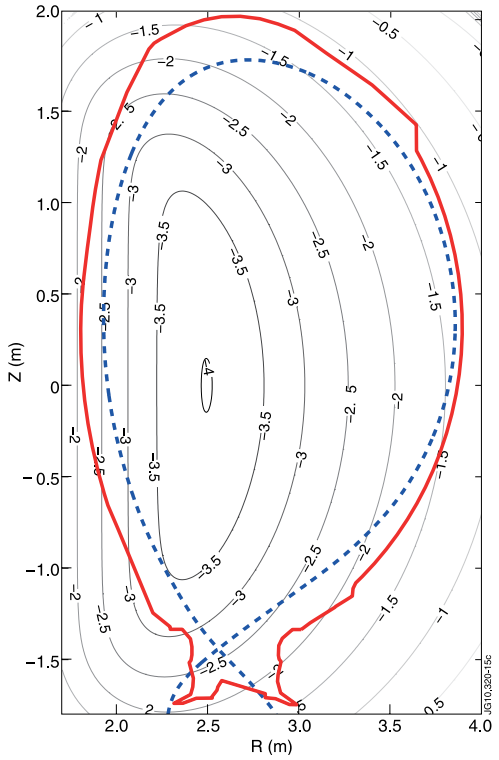

Figure 4. Ripple map for JET 16 coil harmonic together with the cross section of the limiter surface and a separatrix for a typical equilibrium. Numbers on the contours give the $\log_{10}$ of the ripple amplitude.

3. Code-to-code benchmarking

Multiple studies have been conducted regarding the ripple effects, e.g. [15, 16, 36], producing analytical formulae and insights into the physical mechanisms. However, the analytical approach is difficult for realistic simulations when complicating factors arise, e.g. from the geometry of the toroidal field coils, plasma shape, NBI geometry or from the asymmetry of the fast ion distributions. These effects are, however, straightforward to include in the orbit following Monte Carlo codes, as are Coulomb collisions and their synergy with ripple. Nevertheless, it is useful, and helps to interpret the results later on, to see what parameters are involved in ripple banana diffusion [15]

$$\Delta = (N\pi/\sin\theta_t)^{1/2}\left(\frac{q}{\epsilon}\right)^{3/2}\rho\delta\cdot\cos N\phi_t. \tag{1}$$

Here Δ is the radial step size in ripple diffusion at the banana tip, N is the number of toroidal field coils, θ_t and ϕ_t are the poloidal and toroidal angles of the turning point, q is the safety factor, ϵ the inverse of the aspect ratio, ρ the gyro-radius of the ion and δ the ripple

amplitude $\delta = (B_{\max} - B_{\min})/(B_{\min} + B_{\max})$. Even though this formula has been derived for circular plasmas with circular coils it shows that, since the diffusion coefficient $D = \Delta^2\tau^{-1}$ (τ = bounce time), under similar plasma conditions the diffusion is stronger for ions with higher energy and smaller pitch angle (=smaller θ_t) and in areas where the ripple is larger.

3.1. The ripple model in ASCOT

Magnetic field ripple related phenomena from trapping to stochastic ripple diffusion are automatically included in the guiding centre orbit following codes when ions are traced in the full 3D magnetic field. For simulating JET plasmas with ASCOT we superimpose a sinusoidally varying toroidal magnetic field ripple on top of the axi-symmetric equilibrium field, B_0

$$B(r, z, \phi) = B_0(r, z)[1 + \delta_{16}(r, z)\cos 16\phi + \delta_{32}(r, z)\cos 32\phi].$$

Here, the axi-symmetric part is taken from EFIT. The numeric subscripts denote the $N = 16$ and $N = 32$ toroidal harmonic of the Fourier decomposed vacuum ripple map. The original 3D vacuum ripple field, from which the toroidal harmonics are extracted, is simply calculated using the Biot–Savart law by approximating the toroidal field coils with current filaments. In reality, the plasma response to the non-axisymmetric perturbation can generate currents that either screen or enhance the vacuum perturbations. Earlier studies with self-consistent 3D equilibrium codes [37, 38], however, have shown that the vacuum field approximation for the toroidal field ripple is adequate.

During the usual JET operation, all 32 toroidal field coils are driven with an equal amount of current. In this case the level of toroidal field ripple is very low, $\delta_{32} \approx 0.08\%$ at the outboard midplane near the separatrix. In the ripple configuration, the even and odd numbered toroidal field coils can be driven independently giving raise to the $N = 16$ harmonic ripple component. At elevated ripple it is the $N = 16$ harmonic ripple component that gives the dominant effect. This can readily be seen from equation (1). Namely, the diffusion coefficient, $D \propto \Delta^2 \propto N\delta^2$, shows that strongest diffusion comes from δ_{16} as soon as $\delta_{16} \gtrsim 0.12\%$. In these experiments $\delta_{16} \sim 1.5\%$. Figure 4 shows the ripple contours for the pure $N = 16$ harmonic. The toroidal field ripple is largest at the outboard side of the plasma, slightly above the midplane. Although significant near the edge, the ripple field decays rapidly towards the core of the plasma, and it becomes negligible inside the inner half of the plasma.

3.2. ASCOT *benchmark against* OFMC *and* TRANSP

In order to gain general trust in ASCOT calculations we compare it against two other well known codes, OFMC [10, 19, 29] and NUBEAM (inside the TRANSP transport code) [30]. OFMC has been developed and used extensively for JFT-2M and JT-60U and it has been successfully benchmarked against several experimental data [19–21, 39]. More recently OFMC has also been used for JET in preparation and analysis of JET ripple campaign, where good quantitative agreement between the OFMC calculated heat loads due to fast ion losses and experimental values determined by the infra red camera were found [40].

Figure 5 shows an example of ASCOT calculation of the heat load on limiters and on the first wall on the low-field side of the vacuum vessel during high ripple operation. The main heat load from NBI is deposited on the poloidal limiters (grey bars) near the equatorial plane. Heat load on limiters increases with ripple while at the same time localized heat loads below the midplane appear due to ripple trapping. This toroidally periodic heat load pattern, here around poloidal angle, $\theta \sim -70^\circ$, is due to the ripple trapped ions drifting vertically down from the high ripple region. The pattern and localization of these heat loads are well suited for a code-to-code comparison of ripple losses.

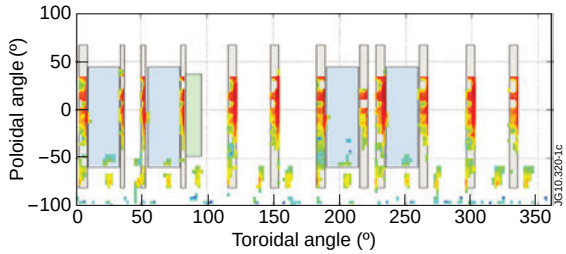

Figure 5. 2D projection of the heat load on the first wall and limiters from NBI in JET under 1.5% ripple as calculated by ASCOT. Blue rectangles show the RF and LH antennas and grey elongated structures the poloidal limiters designed to withstand heat loads up to several MW m^{-2}.

Both ASCOT and OFMC have been used extensively in the preparation and in the analysis of the JET ripple campaigns in 2006–2008 during which they have been cross checked against each other. Here we present one of the comparisons where both codes use a toroidally symmetric 2D limiter surface for clarity and statistics. Both codes use the EFIT equilibrium of the JET discharge 60856 together with the experimental temperature and density profiles. In this example we show data from simulations with artificially high ripple ($\delta \approx 3\%$) with 1 MW of 130 keV NBI. Both codes use their own model for the NBI geometry and for calculating the initial ionization (birth profile).

One can see in the left frame of figure 6 that the codes predict nearly identical heat load patterns with the maximum loads deviating less than 10%. The toroidal angles $\phi = 0^\circ$ and $\phi = 22.5^\circ$ correspond to the location of the high current coils, i.e. ripple minima and the dashed line at $\phi = 11.25^\circ$ correspond to the ripple well. Also, as expected, due to the $1/R$ dependence of the toroidal magnetic field, both codes show a slight shift of the maximum heat load from the ripple minimum in the co-current direction (here ϕ increases in counter-current direction). The right frame shows a comparison of the energy distribution of the ions that cause the heat load on the limiter surface. At higher energies the curves are nearly identical. The deviation at lower energies is due to different lower energy thresholds. Here ASCOT stops ion tracing at higher average energy which yields smaller losses at lower energies.

ASCOT torque calculations and its time-dependent operation without ripple have already been benchmarked against TRANSP in the earlier work [33] with good agreement. Comparisons were made for different discharges, separately for $\boldsymbol{j} \times \boldsymbol{B}$ and collisional torque components and at various beam modulation frequencies. Here, a further comparison between these codes using the reference discharge (77089) is presented. The calculated time-dependent torque profiles from both codes are Fourier transformed at the 6.25 Hz NBI modulation frequency and the resulting torque amplitude, phase and steady-state profiles are shown in figure 7. The reference phase is taken from the injected NBI power, i.e. zero phase corresponds to an instantaneous torque. Note that the phase and amplitude profiles are both related to the dynamics of the torque evaluation. The agreement between the codes is good, both in the magnitude, and in the shape of the profiles.

4. Experimental data analysis

4.1. Torque evaluation

For calculating the NBI torque we use the experimental NBI power waveforms, acceleration voltages and fractions for the E, $E/2$ and $E/3$ energy components. For simplicity, since the

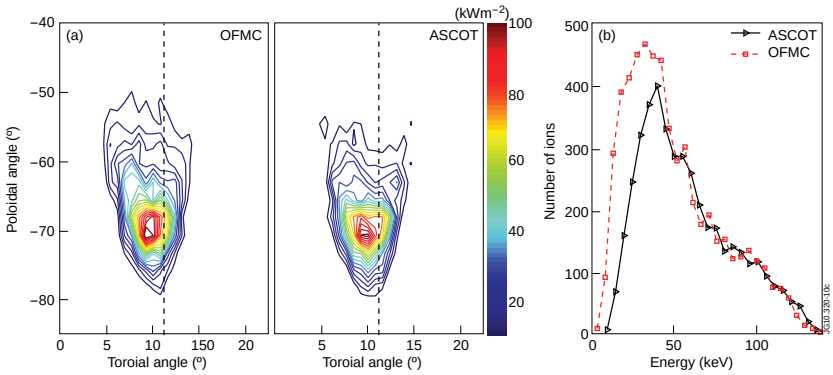

Figure 6. (*a*) Heat load from the ripple trapped ions in the ripple well region as calculated by OFMC and ASCOT. Dashed line shows the toroidal location of ripple minimum. (*b*) Energy spectra of the ripple trapped losses.

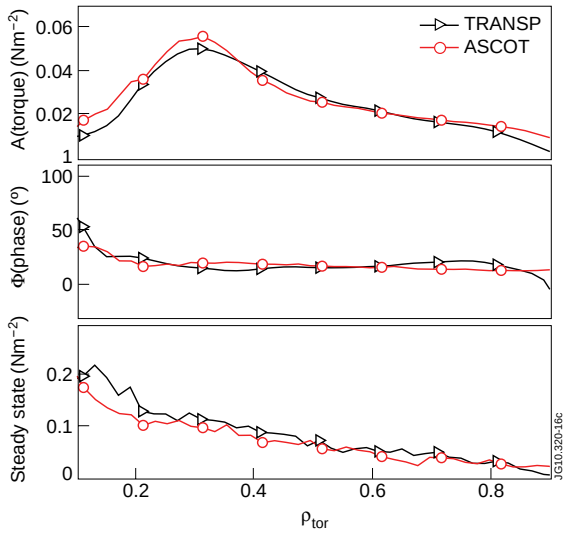

Figure 7. Comparison of ASCOT and TRANSP torque evaluation for the reference discharge (77089). Frames from the top show the Fourier amplitude profile at the 6.25 Hz modulation frequency, the Fourier phase with respect to the NBI power, and the steady-state torque transfer.

plasma profiles are not significantly modulated by the NBI, we time average all the profiles and keep them constant during beam ionization and slowing down calculations. We take the initial NBI ionization profile from PENCIL [41] while the beam slowing down calculation and the ripple effect is accounted for with ASCOT.

Figure 8 summarizes the result of torque evaluation for the three discharges. It shows the time traces of the volume integrated torque components and the time averaged torque

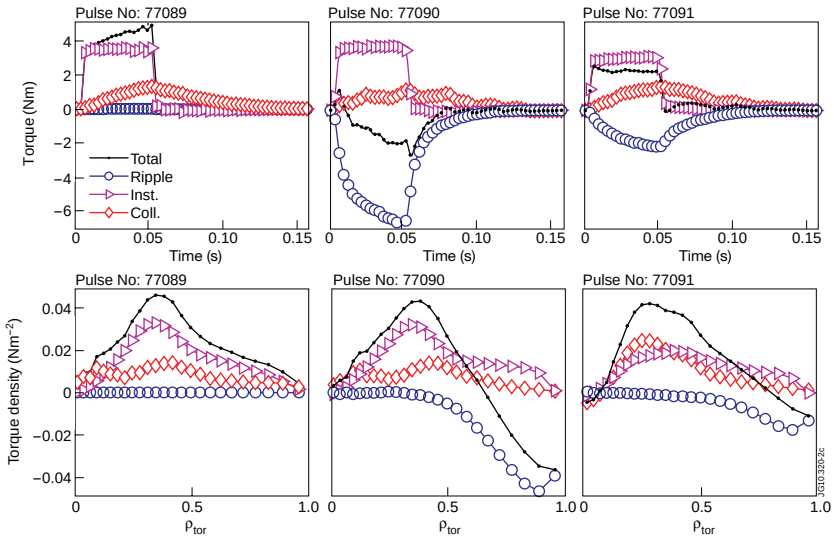

Figure 8. One modulation cycle data for the modulated NBI units only. Top row shows the volume integrated torque separated in ripple, collisional and instantaneous components. Bottom row shows cycle averaged torque densities for each component. 77089 is the reference case with normal NBI, 77090 is with normal NBI and ripple, and 77091 is with tangential NBI and ripple. Note that 77091 uses only two modulated NBI units.

densities for the modulated NBI units only. For better illustration only one NBI modulation cycle is pictured. The total torque is split into three components each with distinct time scale: *collisional* torque due to Coulomb collisions, *instantaneous* torque which is essentially the toroidal component of the $\boldsymbol{j} \times \boldsymbol{B}$ force arising from the difference in the initial and bounce averaged flux surface of the ions. Third, the *ripple* torque is due to the non-ambipolar radial diffusion of the NBI ions in the non-axisymmetric magnetic field. They all have different time scales and must be correctly resolved for simulating the inherently time-dependent NBI modulation experiments.

As shown in figure 8, collisional torque is the slowest of the torque transfer mechanisms and it takes place in fast ion slowing down time ($\sim$150 ms). Instantaneous torque, as the name suggests, is transferred immediately relative to the usual slowing down time. Even in the absence of collisions it will take place in about one bounce time ($\sim$50 μs) during which the initial bounce phases of the injected ions are randomized. Note that due to technical reasons in all the plots in this section, the instantaneous torque includes a small and delayed $\boldsymbol{j} \times \boldsymbol{B}$ torque component, which arises when collisions (or ripple) transform passing ions into trapped ones or vice versa. It is relatively easy to see that the time scale for the ripple torque must be somewhere between the $\boldsymbol{j} \times \boldsymbol{B}$ and collisional torques. This is because ripple diffusion only occurs at the tips of the trapped ion banana orbits, and it necessarily takes several bounce times before any significant effect is accumulated. On the other hand, ripple diffusion scales with the fast ion energy (see equation (1)), making the effect faster than the fast ion slowing down time. The simulations indeed confirm the dynamics.

It is, furthermore, interesting to note that in the case of normal NBI modulation, the generated ripple torque exceeds co-current torque components and therefore makes the total

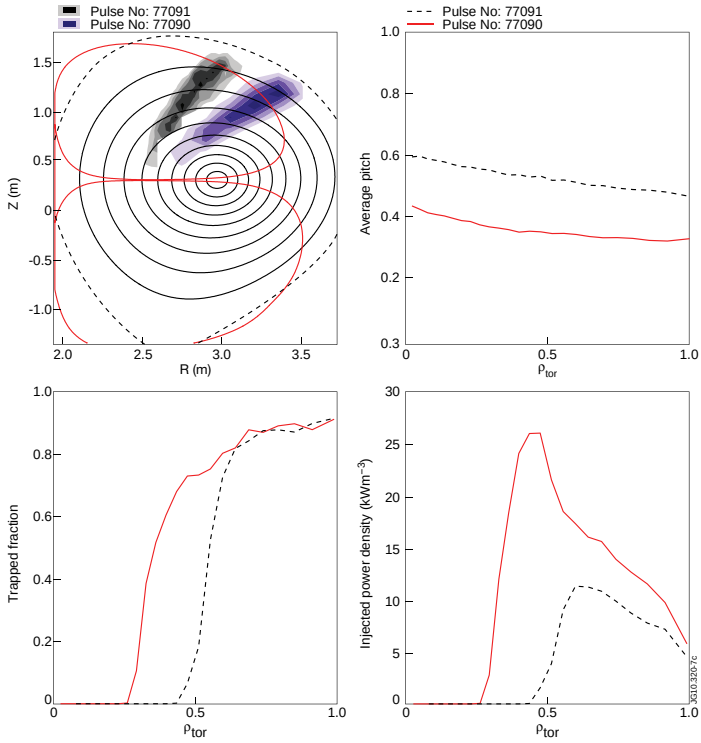

Figure 9. Initial NBI characteristics for trapped ions. (*a*) Turning point density on poloidal cross section for normal (77090) and tangential (77091) injection. The red lines confine a ripple well free region. (*b*) The average initial pitch of all NBI ions, (*c*) the fraction of trapped ions and (*d*) the injected energy density of trapped ions.

modulated torque near the edge negative. Also with the tangential injection, the total deposited torque near the edge becomes counter-current, however, at much smaller margin.

The main differences in the ripple torque generation between the normal and tangential injections can be qualitatively understood from figure 9. The plot on the top left frame shows the initial turning point density and the ripple trapping boundary for the normal (77090) and the tangential (77091) injection. This can be compared with figure 4 to see that with the normal injection the initial turning points locate in a region where the ripple is higher. The average pitch, $\xi = v_{||}/v$, of the newly ionized ions as a function of minor radius is shown on the top right frame. In absolute numbers, the difference between the normal and the tangential injection does not appear to be large, but since the pitch angle scattering becomes more effective at lower energies, the ions from the tangential injection have transferred much of their energy and momentum to the plasma before their average pitch equals that of the normal injection.

The fractions of initially trapped ions are shown in the bottom left frame. While there is a significant difference inside the midradius, the fractions are nearly the same where the ripple is highest, i.e. near the edge. The bottom right figure shows the injected power density of initially

trapped ions. Due to the one less modulated injector, the power density is roughly 30% smaller in the tangential case. This is much too small to account for the factor of 3 difference in the ripple torque between the normal and tangential injection (see figure 8). Also, while not instantly apparent from the figure, the rise time of the generated ripple torque is significantly shorter for the normal injection than it is for the tangential injection. The explanation for these differences can be attributed to the turning point locations. In normal injection, the turning points are instantaneously close to the maximum ripple level of a given flux surface, unlike the ions from the tangential injection. A significant fraction of fast ion slowing down time is spent before the pitch angle scattering has diffused the turning points from tangential NBI into the stronger ripple region. This will both add delay, and reduce the magnitude of the ripple torque in the case of tangential NBI. More details of the torque profiles are shown in the next section, where they are Fourier transformed and plotted side-by-side with the corresponding experimental rotation profiles.

4.2. Rotation measurements

The toroidal rotation of the plasma is measured with a charge exchange recombination spectroscopy (CXRS) diagnostic based on carbon emission lines. The diagnostic has 12 horizontal lines of sight into the plasma which, in this configuration, cover the radius from the centre to the pedestal top, with a time resolution of 10 ms, and $\pm 5\%$ measurement error [42]. Based on earlier experiments on JET [43], and the weak temperature gradients in these discharges, we expect that the bulk plasma (deuterium) rotation is nearly identical to that of the carbon.

Figure 10 shows the toroidal angular frequency of the 3 discharges, as a function of time, for three modulation cycles within the analysis window. The grey areas in the figures indicate the times the modulated NBI is switched on. From this data one can see the spin-up of the plasma when NBI is turned on. However, for discharge 77090 with ripple, near the separatrix (lines at the bottom) the plasma actually accelerates in the opposite direction indicating that, near the edge, the ripple torque exceeds the co-current momentum from the NBI.

For a more quantitative analysis of the experimental rotation profiles we Fourier transform the data for all radial locations. The result at the 6.25 Hz NBI modulation frequency is shown in figure 11 (left column), where the rotation amplitudes, phases and the steady-state profiles are plotted for the three discharges. For comparison the corresponding source terms from ASCOT, i.e. toroidal torque amplitude, phase and steady state, are plotted adjacent on the right column. The similarity of the experimental rotation amplitude and phase profiles and the correspondent calculated torque amplitude and phase profiles is striking. The calculation of the torque is completely independent of the rotation profile, so this clearly indicates the strong influence of the NBI torque on the toroidal rotation. Even before the momentum transport analysis, the topic in the next section, one can see that the rotation profiles and their shapes seem to be consistent with the source profiles.

One of the most obvious differences between the discharges is the higher steady-state rotation of the reference discharge, see bottom left frame of figure 11. It gives a clear indication of the existence of a large counter-current torque in the rippled discharges. In section 4.1 it was found that ions from normal NBI experience stronger ripple effect than those from the tangential NBI. This is also clearly visible in the amplitude and phase plots for both the rotation and torque where the normal NBI with ripple (77090) has larger and deeper penetrating amplitude than the one for the tangential NBI (77091). Note that the injected torque from three normal NBI units is $\sim$15% larger than the torque from two tangential units. The stronger ripple effect on normal NBI is also evident in the steady-state profiles for rotation and torque. It is interesting

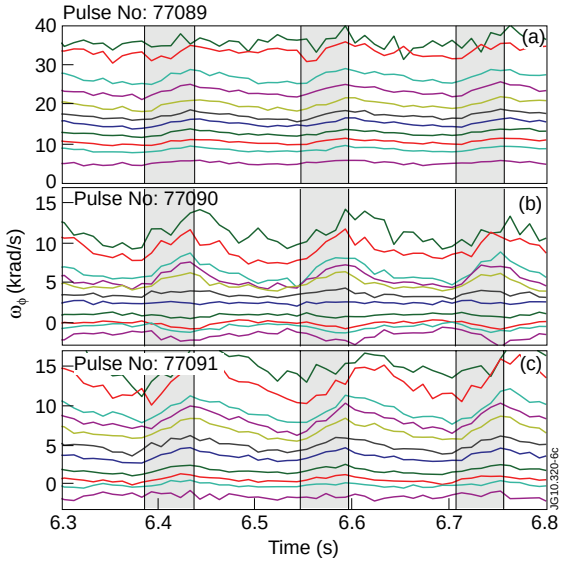

Figure 10. Time traces of CX measurements of toroidal angular frequency at various lines of sight for (*a*) normal NBI without ripple (77089), (*b*) normal NBI with ripple (77090) and (*c*) tangential NBI with ripple (77091). Grey bars indicate the time when modulated NBI is on. Due to the monotonic rotation profile (see figure 3) high values correspond to the centre ($R = 3.05$ m) and low values to the edge of the plasma ($R = 3.78$ m).

to note that the radius of the minimum amplitude for the rotation and the torque for the normal NBI with ripple (77090) coincide at $\rho_{\mathrm{tor}} = 0.6$. This is, in fact, an important feature since it was found to improve the robustness of the torque validation by making the analysis less sensitive to the details of the toroidal momentum transport. Finally, it may first seem odd that inside the midradius, where the ripple amplitude is negligible and where the torque profiles are identical for the normal NBI cases with (77090) and without (77089) ripple, that there is a difference in the rotation phases. This feature, however, is well reproduced in the momentum transport analysis when both the pinch and the diffusion terms are included.

5. Ripple torque validation

As already mentioned, no diagnostic exists that can measure the injected torque directly. CXRS diagnostics can measure the carbon rotation but momentum transport analysis are required to relate the calculated torque source with the rotation. In our transport analysis we assume that for the torque source the reference discharge is calculated accurately with ASCOT, allowing us to use the NBI modulation technique to determine the momentum transport coefficients (Pr, v_{pinch}) without resorting to theoretical models or assumptions other than the momentum transport being independent of the NBI power modulation.

In this work we build on the scheme used in an earlier work [6, 32, 33, 44, 45] to find the optimal profiles for the Prandtl number and the pinch velocity. Here we replace the manual trial and error profile optimization with a non-linear minimizing routine that allows simultaneous

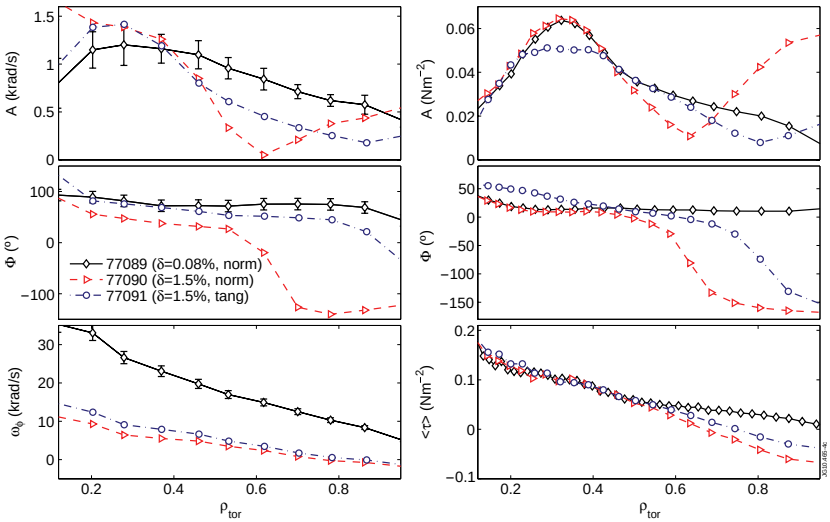

Figure 11. Fourier amplitudes (top), phases (middle) and steady-state values (bottom) of the experimental toroidal rotation profiles (left column) and calculated torque profiles (right column).

fitting of both pinch velocity and Prandtl number profiles. We also make an effort to set suitable optimization criteria *a priori* and let the minimization routine to find the Pr and v_{pinch} profiles that best reproduce the measured rotation profile in an automated way. Note that at this stage we only use data from the reference case since the torque calculations without ripple are already validated. Later we use these results to benchmark the ripple torque calculations.

Similar to the previous work, we use JETTO transport code to calculate the plasma response to the injected torque for the given Pr and v_{pinch} profiles. We take the resulting time-dependent rotation profile and Fourier transform it on all radii to obtain rotation amplitude and phase profiles at the NBI modulation frequency, and to get the steady-state profile. The minimization routine varies the Pr and v_{pinch} profiles until they produce the best possible match between the simulated rotation response and the experimental data for the amplitude, phase and steady-state profiles simultaneously. As a figure of merit for the error in each profile we use the mean squared error against the experimental data which we normalize so that the error for the amplitude, phase and the steady state all yield roughly the same value near the optimum. The individual normalized errors are added together and the resulting error is the target of the minimization.

Typically in one optimization, with 5 radial points each for pinch and Prandtl number profiles, hundreds of transport simulations are needed for converged solution. To ensure the robustness in finding the global optimum in the multi-dimensional parameter space, we launch the above optimization cycle several times, each with a randomly selected initial Pr and v_{pinch} profiles. In this procedure, we usually find that most of the optimized profiles converge to the same solution giving the assurance that the global optimum is found. During the optimization the torque source is taken from ASCOT calculation.

In figure 12 the result of the above optimization cycle is shown for 77089. Black squares are the experimental data and the ensembles of red lines show the amplitude, phase and

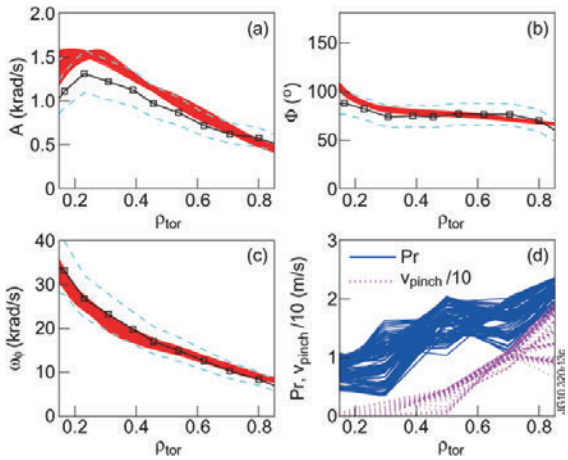

Figure 12. The ensemble of red lines give the rotation (*a*) amplitude (*b*) phase (*c*) steady state of the simulations that yield a target error that is within 10% of the best fit. The corresponding Prandtl number and pinch velocity profiles are plotted in the lower right frame. Black lines with square markers show the experimental data and the dashed lines give the 20% interval around the measurements for rotation and rotation amplitude and 11.25° (5 ms equivalent in time) for phase and help to quantify the quality of the fit.

steady-state profiles from all converged and nearly converged states where the total error is within 10% of the best fit. The dashed lines in the amplitude and steady-state plots show the ±20% variation and are there to help quantify the level of agreement achieved. The dashed line in the phase plot shows the ±11.25° variation corresponding to a 5 ms time resolution. In the simulations we use 3–5 ms resolution for the data, while the time integration period for the rotation measurement is 10 ms, thus making the 5 ms as a reasonable estimate for the phase error. The bottom right frame in figure 12 shows the set of the pinch velocity and Prandtl number profiles that correspond to the described amplitude, phase and steady-state profiles.

We find that roughly 30% variation in transport coefficients around the optimum is allowed while still giving a good fit against the experiment. There are a few reasons why this can be expected. Firstly, small changes in the diffusion coefficient can, to some extent, be compensated by appropriate changes in the pinch velocity without increasing the total error significantly. Secondly, the definition of the total error (mean squared error) is not very sensitive to the profile shapes and can yield similar errors for qualitatively different profiles. Furthermore, as typical for profile optimization, a small change in one profile point can partly be compensated by changes in the neighbouring points. However, even with the scatter in the profiles one can easily recognize the increasing trend towards the edge in both profiles which is consistent with the earlier work [6, 11].

The optimal profiles for the Prandtl number and the pinch velocity are shown in figure 13. We find that, apart from the centre of the plasma, the Prandtl number stays above unity in these L-mode discharges, while slightly smaller values were previously found for the H-mode discharges [33] and in theory [46]. It is noteworthy also that, for the first time on JET L-mode plasmas, we find that a non-zero pinch velocity is required to fit the rotation amplitude, phase and steady-state profiles simultaneously.

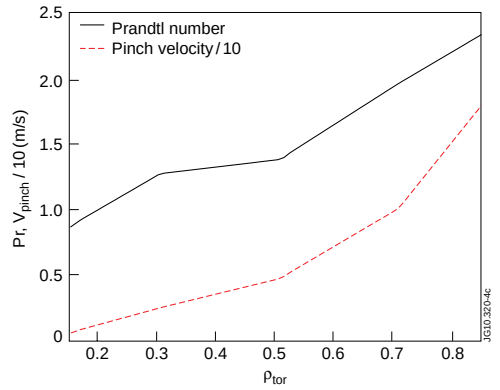

Figure 13. Optimized Prandtl number and pinch velocity profiles for 77089.

The main piece of evidence in the experimental ASCOT NBI torque validation effort is shown in figure 14 where the comparison between the simulated toroidal rotation and the experimental measurements are plotted for each discharge. Note that the momentum transport is assumed to be the same across all discharges as discussed earlier. It is seen that the simulated rotation response to the NBI modulation agrees well with the measurements. For all cases, the time response (phase) is matched within about 11.25° corresponding to about 5 ms time resolution. Also the amplitude and steady-state rotation profiles agree with the experimental data to within 20%. Furthermore, during the analysis it was seen that for the normal injection with ripple (77090) the radius where the phase of simulated rotation changes its sign, $\rho_{\mathrm{tor}} = 0.6$, is almost entirely determined by the torque source profile. Using Prandtl numbers that were smaller than the optimal found made the gradient too steep and, conversely, Prandtl numbers larger than the optimum flattened the gradient. However, the radius where the sign reversal occurs remained largely unaffected. These observations suggest that the NBI torque profiles with large ripple are consistent with measurements, a conclusion which is not very sensitive to the details of the momentum transport.

For completeness we used the optimization scheme also for the discharges with ripple to see if the optimized transport would differ from the one obtained from the reference case (see figure 13). We found that the agreement between the simulated and the measured rotation amplitude, phase and steady-state profiles were only marginally improved compared with using the transport from the reference discharge. This also implies that the momentum transport is indeed similar among the 3 discharges.

6. Conclusions

We have shown for the first time an experimental validation of a NBI torque profile calculation in the presence of large magnetic field ripple. We have used NBI modulation technique to deduce the prevalent momentum transport, and time-dependent torque calculations from ASCOT to make the comparison. We have developed a semi-automated way to analyse the transport in the NBI modulation experiments, based on a least squares optimization scheme, to obtain a more comprehensive picture of the transport sensitivity. We have also validated ASCOT ripple operation numerically against OFMC by comparing the heat load from ripple trapped ions, and

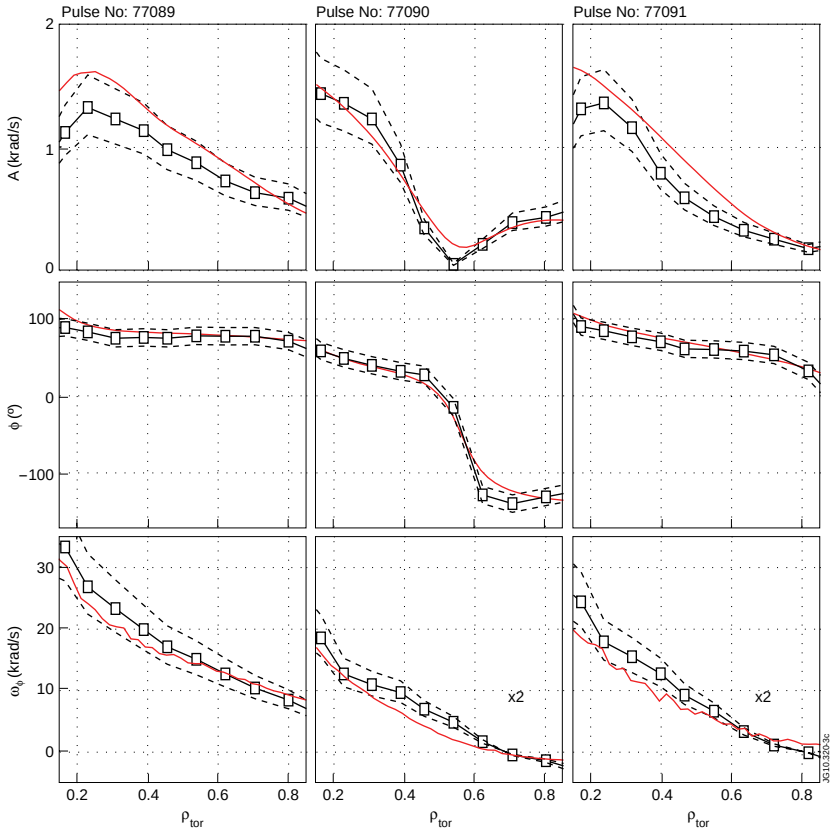

Figure 14. Amplitude, phase and steady-state profiles for the three discharges using the optimized Prandtl number and pinch velocity profiles for 77089 (see figure 13). The first column corresponds to the 77089, the second column to 77090 and the third column to 77091. Dashed lines are a guide to the eye and give rough estimates of the error.

showed good agreement against TRANSP for the time-dependent NBI torque evaluation without ripple. Although only JET L-mode discharges, optimized for the ripple torque validation, were used in this work, the previous work with heat load and torque validation, e.g. [19, 24], suggests that the guiding centre following Monte Carlo approach is accurate more generally and can be used for predicting the NBI torque under conditions where the guiding centre approximation holds.

In this work we only considered NBI for the core torque source. The modulated torque especially should be clearly dominated by the NBI and ripple, since the small induced plasma perturbations ($\delta T_e, \delta T_i, \delta q, \delta n_e$) due to the NBI are not expected to modify the turbulent character of the plasma significantly. However, it is possible that some intrinsic sources were contributing to the steady-state torque. While they are mainly expected to be edge localized [46], experimental evidence for intrinsic core sources have also been reported [47].

During the transport analysis we did observe, similar to some earlier H-mode cases [6, 33], that for the best overall fit (simultaneous fit of the amplitude, phase and steady-state rotation) the simulated rotation amplitudes tended to get slightly overestimated and the steady-state rotation underestimated. While, on the one hand, this could indicate a small error in the NBI torque calculations, it may also point to an intrinsic core torque contribution like residual stress in the co-current direction. It must be noted, however, that because of the good agreement shown here, the intrinsic core torque source in these discharges should be small.

For future work this method will be modified to allow systematic estimation of the magnitude of the intrinsic torque source in the core plasma even in the presence of NBI torque. For edge localized torque source studies this scheme would seem not to be as promising due to less accurate measurements in the pedestal region which makes it more difficult to separate the sources from the boundary contribution.

Acknowledgments

The authors wish to thank Dr N Oyama and Dr K Shinohara for their help in setting up OFMC for JET and Dr D Howell for providing the vacuum ripple map.

This work, supported by the European Communities under the contract of Association between EURATOM and Tekes, was carried out within the framework of the European Fusion Development. The views and opinions expressed herein do not necessarily reflect those of the European Commission.

References

[1] Biglari H, Diamond P H and Terry P W 1990 Influence of sheared poloidal rotation on edge turbulence *Phys. Fluids B: Plasma Phys.* **2** 1–4

[2] Garofalo A M *et al* and DIII-D Team 2001 Resistive wall mode dynamics and active feedback control in DIII-D *Nucl. Fusion* **41** 1171

[3] Peeters A G, Angioni C and Strintzi D 2007 Toroidal momentum pinch velocity due to the Coriolis drift effect on small scale instabilities in a toroidal plasma *Phys. Rev. Lett.* **98** 265003

[4] Hahm T S, Diamond P H, Gurcan O D and Rewoldt G 2007 Nonlinear gyrokinetic theory of toroidal momentum pinch *Phys. Plasmas* **14** 072302

[5] Yoshida M, Koide Y, Takenaga H, Urano H, Oyama N, Kamiya K, Sakamoto Y, Matsunaga G, Kamada Y and the JT-60 Team 2007 Momentum transport and plasma rotation profile in toroidal direction in JT-60U L-mode plasmas *Nucl. Fusion* **47** 856

[6] Tala T *et al* 2009 Evidence of inward toroidal momentum convection in the JET tokamak *Phys. Rev. Lett.* **102** 075001

[7] Solomon W M *et al* and the DIII-D Rotation Physics Task Force 2009 Advances in understanding the generation and evolution of the toroidal rotation profile on DIII-D *Nucl. Fusion* **49** 085005

[8] de Vries P C, Versloot T W, Salmi A, Hua M-D, Howell D H, Giroud C, Parail V, Saibene G, Tala T and JET EFDA Contributors 2010 Momentum transport studies in JET H-mode discharges with an enhanced toroidal field ripple *Plasma Phys. Control. Fusion* **52** 065004

[9] Tala T *et al* 2010 JET rotation experiments towards the capability to predict the toroidal rotation profile *Proc. 23rd Int. Conf. on Fusion Energy, (Daejeon, Korea, 2010)* EXC/3-1

[10] Shinohara K, Oikawa T, Urano H, Oyama N, Lönnroth J, Saibene G, Parail V and Kamada Y 2009 Effects of ferromagnetic components on energetic ion confinement in ITER *Fusion Eng. Des.* **84** 24–32

[11] de Vries P C *et al* and JET EFDA Contributors 2008 Effect of toroidal field ripple on plasma rotation in JET *Nucl. Fusion* **48** 035007

[12] Nave M F F, Johnson T, Eriksson L-G, Crombé K, Giroud C, Mayoral M-L, Ongena J, Salmi A, Tala T and Tsalas M 2010 Influence of magnetic field ripple on the intrinsic rotation of tokamak plasmas *Phys. Rev. Lett.* **105** 105005

[13] Callen J D 2010 Effects of 3D magnetic perturbations on toroidal plasmas *Proc. 23rd Int. Conf. on Fusion Energy (Daejeon, Korea, 2010)* OV/4-3
[14] Diamond P H, McDevitt C J, Gürcan Ö D, Hahm T S, Wang W X, Yoon E S, Holod I, Lin Z, Naulin V and Singh R 2009 Physics of non-diffusive turbulent transport of momentum and the origins of spontaneous rotation in tokamaks. *Nucl. Fusion* **49** 045002
[15] Goldston R J, White R B and Boozer A H 1981 Confinement of high-energy trapped particles in tokamaks *Phys. Rev. Lett.* **47** 647–9
[16] Yushmanov P N 1990 *Rev. Plasma Phys.* **16** 117
[17] Heidbrink W W and Sadler G J 1994 The behaviour of fast ions in tokamak experiments *Nucl. Fusion* **34** 535
[18] Boivin R L, Zweben S J and White R B 1993 Study of stochastic toroidal field ripple losses of charged fusion products at the midplane of TFTR *Nucl. Fusion* **33** 449
[19] Shinohara K *et al*, the JFT-2M Group and Darrow D S 2003 Effects of complex magnetic ripple on fast ions in JFT-2M ferritic insert experiments *Nucl. Fusion* **43** 586
[20] Tobita K, Tani K, Neyatani Y, van Blokland A A E, Miura S, Fujita T, Takeuchi H, Nishitani T, Matsuoka M and Takechi S 1992 Ripple-trapped loss of neutral-beam-injected fast ions in JT-60U *Phys. Rev. Lett.* **69** 3060–3
[21] Ikeda Y, Tobita K, Hamamatsu K, Ushigusa K, Naito O and Kimura H 1996 Ripple enhanced banana drift loss at the outboard wall during ICRF/NBI heating in JT-60U *Nucl. Fusion* **36** 759
[22] Heidbrink W W, Kim J and Groebner R J 1988 Comparison of experimental and theoretical fast ion slowing-down times in DIII-D *Nucl. Fusion* **28** 1897
[23] Ruskov E, Heidbrink W W and Budny R V 1995 Diffusion of beam ions at the tokamak fusion test reactor *Nucl. Fusion* **35** 1099
[24] deGrassie J S, Groebner R J and Burrell K H 2006 Prompt toroidal momentum balance with collisionless neutral beam injected torque in DIII-D *Phys. Plasmas* **13** 112507
[25] de Vries P C *et al* and JET EFDA Contributors 2008 Effect of toroidal field ripple on the formation of internal transport barriers *Plasma Phys. Control. Fusion* **50** 065008
[26] Heikkinen J A and Sipilä S K 1995 Power transfer and current generation of fast ions with large-k_θ waves in tokamak plasmas *Phys. Plasmas* **2** 3724–33
[27] Heikkinen J A, Herrmann W and Kurki-Suonio T K 1998 Fast response in the ripple trapped ion distribution to abrupt changes in a radial electric field in tokamaks *Nucl. Fusion* **38** 419
[28] Salmi A, Johnson T, Parail V, Heikkinen J, Hynönen V, Kiviniemi T P, Kurki-Suonio T and JET EFDA Contributors 2008 Ascot modelling of ripple effects on toroidal torque *Contrib. Plasma Phys.* **48** 77–81
[29] Tani K, Azumi M, Kishimoto H and Tamura S 1981 Effect of toroidal field ripple on fast ion behavior in a tokamak *J. Phys. Soc. Japan* **50** 1726–37
[30] Pankin A, McCune D, Andre R, Bateman G and Kritz A 2004 The tokamak Monte Carlo fast ion module nubeam in the national transport code collaboration library *Comput. Phys. Commun.* **159** 157–84
[31] Duesing G, Altmann H, Falter H, Goede A, Haange R, Hemsworth R S, Kupschus P, Stork D and Thompson E 1987 Neutral beam injection system *Fusion Technol.* **11** 163–202 (cited By (since 1996) 44)
[32] Tala T *et al* and JET-EFDA Contributors 2007 Toroidal and poloidal momentum transport studies in tokamaks *Plasma Phys. Control. Fusion* **49** B291
[33] Mantica P *et al* and JET-EFDA Contributors 2010 Perturbative studies of toroidal momentum transport using neutral beam injection modulation in the joint european torus: Experimental results, analysis methodology, and first principles modeling *Phys. Plasmas* **17** 092505
[34] Mattor N and Diamond P H 1988 Momentum and thermal transport in neutral-beam-heated tokamaks *Phys. Fluids* **31** 1180–9
[35] Lao L 1990 Efit *Nucl. Fusion* **30** 1035
[36] Goloborod'ko V Ya, Kolesnichenko Ya I and Yavorskij V A 1987 Alpha particle transport processes in tokamaks *Phys. Scr.* **T16** 46
[37] Suzuki Y, Nakamura Y and Kondo K 2003 Finite beta effects on the toroidal field ripple in three-dimensional tokamak equilibria *Nucl. Fusion* **43** 406
[38] Strumberger E, Günter S, Merkel P, Schwarz E and Tichmann C 2010 Self-consistent three-dimensional computations of non-axisymmetric ITER equilibria *Nucl. Fusion* **50** 025008
[39] Tobita K, Tani K, Nishitani T, Nagashima K and Kusama Y 1994 Fast ion losses due to toroidal field ripple in JT-60U *Nucl. Fusion* **34** 1097
[40] Johnson T *et al* and JET-EFDA contributors Halekar modelling of fast particle transport and losses with TF ripple in JET *10th IAEA Technical Meeting on Energetic Particles in Magnetic Confinement Systems (Kloster Seeon, Germany)*
[41] Challis C D *et al* 1989 *Nucl. Fusion* **29** 563

[42] Carine Giroud, Meigs A G, Negus C R, Zastrow K-D, Biewer T M, Versloot T W and JET-EFDA Contributors 2008 Impact of calibration technique on measurement accuracy for the JET core charge-exchange system *Rev. Sci. Instrum.* **79** 10F525

[43] Testa D, Giroud C, Fasoli A, Zastrow K-D and EFDA-JET Team 2002 On the measurement of toroidal rotation for the impurity and the main ion species on the Joint European Torus *Phys. Plasmas* **9** 243–50

[44] Mantica P *et al* 2009 Experimental study of the ion critical-gradient length and stiffness level and the impact of rotation in the JET tokamak *Phys. Rev. Lett.* **102** 175002

[45] Tardini G, Ferreira J, Mantica P, Peeters A G, Tala T, Zastrow K D, Brix M, Giroud C, Pereverzev G V and JET-EFDA contributors 2009 Angular momentum studies with NBI modulation in JET *Nucl. Fusion* **49** 085010

[46] Peeters A *et al* 2010 Toroidal momentum transport *Proc. 23rd Int. Conf. on Fusion Energy (Daejeon, Korea, 2010)* OV/5-4

[47] Solomon W M *et al* 2010 Mechanisms for generating toroidal rotation in tokamaks without external momentum input *Phys. Plasmas* **17** 056108

PUBLICATION VI

Parametric dependences of momentum pinch and Prandtl number in JET

In: Nuclear Fusion 51, 123002 (11 pp), 2011.

http://iopscience.iop.org/0029-5515/51/12/123002/pdf/0029-5515_51_12_123002.pdf

IOP Publishing and International Atomic Energy Agency Nuclear Fusion

Nucl. Fusion **51** (2011) 123002 (11pp) doi:10.1088/0029-5515/51/12/123002

Parametric dependences of momentum pinch and Prandtl number in JET

T. Tala[1], A. Salmi[2], C. Angioni[3], F.J. Casson[3], G. Corrigan[4], J. Ferreira[5], C. Giroud[4], P. Mantica[6], V. Naulin[7], A.G. Peeters[8], W.M. Solomon[9], D. Strintzi[8], M. Tsalas[10], T.W. Versloot[10], P.C. de Vries[10], K.-D. Zastrow[4] and JET-EFDA contributors[a]

JET-EFDA, Culham Science Centre, OX14 3DB, Abingdon, UK
[1] Association EURATOM-Tekes, VTT, PO Box 1000, FIN-02044 VTT, Finland
[2] Association EURATOM-Tekes, Aalto University, Department of Applied Physics, Finland
[3] Max-Planck-Iinstitut für Plasmaphysik, EURATOM-Assoziation, Garching, Germany
[4] EURATOM/CCFE Fusion Association, Culham Science Centre, Oxon. OX14 3DB, UK
[5] Associação EURATOM/IST, Instituto de Plasmas e Fusao Nuclear, 1049-001 Lisbon, Portugal
[6] Istituto di Fisica del Plasma CNR-EURATOM, via Cozzi 53, 20125 Milano, Italy
[7] Association Euratom-Risø-DTU, Denmark
[8] Physics Department, University of Bayreuth, 95440 Bayreuth, Germany
[9] Princeton Plasma Physics Laboratory, Princeton University, Princeton, NJ 08543, USA
[10] FOM Institute Rijnhuizen, Association EURATOM-FOM, Nieuwegein, The Netherlands

E-mail: tuomas.tala@vtt.fi

Received 21 June 2011, accepted for publication 7 October 2011
Published 7 November 2011
Online at stacks.iop.org/NF/51/123002

Abstract
Several parametric scans have been performed to study momentum transport on JET. A neutral beam injection modulation technique has been applied to separate the diffusive and convective momentum transport terms. The magnitude of the inward momentum pinch depends strongly on the inverse density gradient length, with an experimental scaling for the pinch number being $-Rv_{\mathrm{pinch}}/\chi_\phi = 1.2R/L_{\mathrm{n}} + 1.4$. There is no dependence of the pinch number on collisionality, whereas the pinch seems to depend weakly on q-profile, the pinch number decreasing with increasing q. The Prandtl number was not found to depend either on R/L_{n}, collisionality or on q. The gyro-kinetic simulations show qualitatively similar dependence of the pinch number on R/L_{n}, but the dependence is weaker in the simulations. Gyro-kinetic simulations do not find any clear parametric dependence in the Prandtl number, in agreement with experiments, but the experimental values are larger than the simulated ones, in particular in L-mode plasmas. The extrapolation of these results to ITER illustrates that at large enough $R/L_{\mathrm{n}} > 2$ the pinch number becomes large enough (>3–4) to make the rotation profile peaked, provided that the edge rotation is non-zero. And this rotation peaking can be achieved with small or even with no core torque source. The absolute value of the core rotation is still very challenging to predict partly due to the lack of the present knowledge of the rotation at the plasma edge, partly due to insufficient understanding of 3D effects like braking and partly due to the uncertainties in the extrapolation of the present momentum transport results to a larger device.

(Some figures may appear in colour only in the online journal)

1. Introduction

Plasma rotation and momentum transport are currently very active areas of research, both experimentally and theoretically. It is well known that sheared plasma rotation can stabilize turbulence [1–4] while the rotation itself has beneficial effects on MHD modes, such as resistive wall modes or neoclassical tearing modes (NTMs) [5, 6]. Although the importance of rotation has been recently recognized, predicting or extrapolating the toroidal rotation profile has turned out to be extremely challenging and several key issues remain. The uncertainties in the predictions can be classified into the following three main categories: core torque sources and sinks, edge rotation and sources/sinks and momentum transport.

The neutral beam injection (NBI) torque source is relatively well established, and a lot of work has been

[a] See the appendix of Romanelli F. *et al* 2011 *Nucl. Fusion* **51** 094008.

performed recently to compare and benchmark different codes [7, 8]. These benchmark activities have been performed to be sure that the torque calculation between different codes agrees well so that no significant error is propagated into the momentum transport analysis when analysing NBI modulation experiments. The NBI torque calculation is believed to be understood even with a large toroidal magnetic field ripple amplitude. The NBI torque calculation in plasmas with large ripple has been recently benchmarked against JET experiments and good agreement has been found [8]. The most important effect of the NBI on rotation in plasmas with a ripple on JET was found to be due to non-ambipolar fast ion losses, causing a counter current torque on the plasma [9].

In addition to NBI, other core torque sources and sinks are less understood. Intrinsic rotation in ICRH, ECRH and ohmic plasmas still requires clarification [10–12]. In JET, in plasmas with the usual ripple of $\delta = 0.08\%$, the angular frequency of the intrinsic rotation is less than $\omega_\phi < \pm 10\,\mathrm{krad\,s^{-1}}$ [13]. The ripple also affects the angular rotation frequency under the conditions of no external momentum input. The ripple amplitude was varied from $\delta = 0.08\%$ to $\delta = 1.5\%$ in ohmic and ICRH heated plasmas. Ripple affects both the edge rotation by lowering it typically close to zero or to small counter-rotation values and also the core rotation where it becomes counter-rotating [14]. In addition to the effect of ripple on fast ions, as rotation in ohmic plasmas was also affected by the magnitude of the ripple, there is evidence that thermal ions are influenced by the ripple, being an indication of an neoclassical toroidal viscosity (NTV) type of process in place with a large enough ripple. This NTV is also present in NBI and ICRH heated plasmas with ripple, but its influence on rotation is masked to a large extent by the effect of fast ions on rotation. Recently, an experiment to study mode conversion flow drive (MCFD) was also performed in L-mode plasmas using a He^3 ICRH scheme [15]. MCFD was found to be sensitive to the He^3 concentration level. Large central counter-rotation up to $\omega_\phi = -10\,\mathrm{krad\,s^{-1}}$ ($v_\phi = -30\,\mathrm{km\,s^{-1}}$) was observed at He^3 concentration levels of 10–17%. The physical mechanism of MCFD is not yet completely understood, but clearly some core torque source exists, as also found in MCFD experiment on C-Mod [16].

Another unknown torque source in the core plasma, probably also being very important in ITER rotation predictions, is seen as a strong toroidal rotation braking in plasmas with application of an $n = 1$ magnetic perturbation field on JET [17]. The maximum value (typically about half of the NBI torque) of the torque is at the plasma central region ($\rho < 0.4$). Moreover, it is not localized at certain magnetic surfaces, indicating that the non-resonant component dominates over the resonant magnetic braking. The NTV calculation shows that in these JET plasmas the calculated NTV torque profile is an order of magnitude smaller than the experimentally observed torque profile T_{EFCC}, indicative of a core torque source that is far from fully understood. NTV type of torque has been observed earlier also for example on DIII-D [18]. In addition to the magnetic perturbation coils, there is evidence from DIII-D that the test blanket modules (TBMs) may have a very large effect on plasma rotation in the plasma core [19].

The second major issue in giving large uncertainties in ITER rotation predictions is the lack of the knowledge of the edge rotation as well as edge torque sources. In principle, there is a similar problem in predicting the rotation profile as predicting the temperature profile—the boundary/pedestal value must be known accurately in order to predict the toroidal rotation profile in the core plasma. Recently, the loss of plasma toroidal angular momentum and thermal energy due to edge localized modes (ELMs) has been studied in JET. The analysis shows a consistently larger drop in momentum in comparison with the energy loss associated with the ELMs under a wide variety of plasma conditions [20]. Another edge uncertainty is the charge-exchange interaction between the plasma ions and the neutral particle background creating a continuous sink of momentum and energy. The magnitude of CX losses increases to approximately 10% of the total input torque with the power losses being smaller with an increasing amount of neutrals [21]. Additional known uncertainties in the edge rotation and torque sources are, for example, due to toroidal magnetic field ripple [9], TBMs [19] and interaction with SOL flows, seen for example between the upper and lower null configurations on C-Mod [22, 23] and a term in the momentum flux called residual stress [24].

While the core and edge torque sources and the edge rotation question are crucial in order to be able to predict the rotation profile in future tokamaks, in this paper we concentrate on core momentum transport studies. The momentum diffusivity χ_ϕ and pinch velocity v_{pinch} (negative sign denotes inwards) are related to the toroidal velocity v_ϕ, its gradient ∇v_ϕ and the momentum flux Γ_ϕ, assuming the absence of a significant particle flux, as follows:

$$\Gamma_\phi \sim -n\chi_\phi \nabla v_\phi + n v_{\mathrm{pinch}} v_\phi = -n\chi_\phi^{\mathrm{eff}} \nabla v_\phi \qquad (1)$$

where n is the ion density. The diffusive and convective part of the momentum flux can be combined into an effective momentum diffusivity χ_ϕ^{eff}, which can be calculated from steady-state rotation profiles once momentum sources are known. This equation is a simplification of the actual momentum flux as it includes only terms proportional to the gradient of the rotation or the rotation itself. There is a term missing in equation (1) called a residual stress [24] that refers to the part of the momentum flux which is not diffusive or pinch. Studies of the residual stress term is beyond the scope of this work, with the exception of a comment on the possible role of a residual stress in this analysis and a term proportional to the $E \times B$ shear [25] based on gyro-kinetic simulations. There is a comprehensive recent overview of toroidal momentum transport with all flux terms described in detail in [26]. The best and most clean way of identifying separately diffusive and convective transport components is by means of perturbative experiments, i.e. exploiting the additional information contained in the dynamic response of the plasma rotation to a time variation of the torque source. Perturbating the rotation has been successfully applied to momentum transport studies using NBI modulation or magnetic perturbations on several tokamaks. In particular, it has been possible to demonstrate the existence of the momentum pinch on JT-60U [27], JET [7, 28–30], DIII-D [31] and NSTX [32, 33]. In all of these studies although the pinch and diffusive components were separated, no systematic studies have been experimentally carried out to study the parametric dependences of the momentum pinch and diffusive

terms. In order to understand how the pinch and diffusive terms extrapolate for example to ITER from the present tokamaks, parametric dependences of those parameters must be known, and this is the main scope of this paper.

From the theoretical point of view, the existence of the momentum pinch is also evident [34, 35]. According to theory, momentum pinch is expected to depend strongly on the inverse density gradient length R/L_n and weakly on q [26, 34]. The dependence of the momentum pinch on collisionality is found to be almost negligible [36]. The dependence of the Prandtl number on any of the parameters is expected to be small, certainly smaller than that of the momentum pinch [26]. As a consequence, the main parametric dependences studied in this work are R/L_n, collisionality ν^* and q-profile. In addition, a comparison between the H-mode and L-mode plasmas is performed.

The content of the paper is organized as follows. The experimental details, such as the NBI modulation technique, the momentum transport analysis and the NBI torque calculation are described in section 2. The results from the experimental scan to study momentum transport are described in detail in section 3. The experiment to study the collisionality dependence is presented in section 3.1. In section 3.2, the results on the R/L_n scan is summarized. Section 3.3 is devoted to the q-profile scan. The difference in momentum transport between L-mode and H-mode plasmas is shown in section 4. The role of the inward momentum pinch and the rotation boundary conditions in ITER extrapolation of the toroidal rotation is illustrated in section 5. Section 6 summarizes the main results of this paper.

2. Experimental set-up to exploit NBI modulation technique for momentum transport studies

The NBI modulation experiments have been carried out in different types of JET plasmas to study the parametric dependences of momentum pinch and Prandtl numbers. Most of the plasmas in these scans are in the following parameter regime: low collisionality JET H-mode plasmas at $B_T = 3$ T, $I_p = 1.5$ MA and $n_{e0} \sim 4 \times 10^{19}$ m^{-3}. This is combined with a minimum level of MHD activity to prevent interference with the perturbation analysis, i.e. at high $q_{95} \sim 7$ to avoid large sawteeth in the centre and with type III ELMs to avoid large periodic edge crashes. Total power levels were up to 15 MW for NBI, including the modulation, and 0–4 MW for ICRH in H minority scheme. Some of the pulses were performed with much less power (∼4–5 MW) so that they stayed in L-mode. Both in L-mode and H-mode plasmas with NBI modulation, ion temperature gradients (ITGs) are the dominant instability on JET. As the Prandtl number is defined as $P_r = \chi_\phi/\chi_i$, i.e. inversely proportional to the ion heat diffusivity, a comparison of the Prandtl number between different plasmas is more unambiguous in ITG dominated plasmas where momentum and ion heat transport are tightly coupled. In TEM dominated plasmas or in plasmas where collisional heat transfer between ions and electrons is significant, momentum and ion heat transport are less coupled, thus making $P_r = \chi_\phi/\chi_i$ a less relevant parameter to characterize momentum transport and compare different discharges and parametric dependences.

The NBI torque source is the only available tool for inducing a significant rotation modulation in JET, although it is not ideal because its deposition profile is very broad, which is a complicating factor in the analysis, unlike in the case of localized RF heat sources. On the other hand, the torque sources from NBI can be calculated more precisely than the radio-frequency power sources. A detailed description of the use of the NBI modulation technique and momentum transfer from the fast NBI ions to the bulk is presented in [7, 29].

In these JET experiments, the NBI power and torque were square wave modulated with a duty cycle of either 50% or 33% at a frequency $f_{mod} = 6.25$ Hz or $f_{mod} = 8.33$ Hz, which is the highest technically possible. This frequency is high enough to make the $\boldsymbol{J} \times \boldsymbol{B}$ torque the dominant source of torque perturbation everywhere outside $r/a > 0.3$. The modulation cycle is, on the other hand, much longer than the 10 ms time resolution of the charge exchange recombination spectroscopy (CXRS) diagnostic used to measuring the toroidal rotation profile ω_ϕ and ion temperature T_i at 12 radial points [37]. The modulated power varies from 2 to 5 MW, the power tuned to create an appropriate size of the rotation modulation amplitude of around 5%. Consequently, it is possible to observe changes in toroidal rotation in the beam on and beam off periods and perform the Fourier analysis of the modulated rotation. The modulation takes place in a stationary phase for 5–6 s. One can therefore choose the most stationary phase of the shot, with respect to density or temperature variation, to carry out the momentum transport analysis because typically some 10–20 modulation cycles (1–2 s) give enough statistics for the standard fast Fourier transformation (FFT) analysis. FFT has been applied to experimental time traces at various radial positions of ω_ϕ, T_i and T_e, to derive spatial profiles of amplitude (A) and phase (φ) of the perturbation.

Due to the absence of a torque source free region where the transport analysis could be performed independent of the details of the source, the calculation of the time-dependent torque profile is an essential step for the derivation of the momentum transport coefficients from the data. The transport analysis will in fact rely on full momentum transport simulations in which the torque source is assumed to be known precisely enough, with the obvious consequence that any error in the source will cause an error on the derived transport coefficients. It is to be noted here that the NBI torque is the only torque source taken into account in this analysis. Thus the following terms are ignored that could affect the results presented in this paper: residual stress, direct ICRH driven torque (only two of the analysed shots have ICRH, with zero phasing it ought to be small) and possible torque sources/sinks due to MHD such as ELMs or NTMs. The analysed plasmas were with type III ELMs and the NTM activity varied from zero to very mild, thus the torque originating from these is negligible as compared with the large NBI torque. The possible role of the residual stress term is discussed later in the paper.

For the calculation of NBI torque, great care has then been dedicated to such calculations and associated uncertainties. Either the TRANSP code [38] or the ASCOT code [39] has been used to calculate NBI power and torque profiles as a function of time, given the time-dependent experimental profiles of all plasma parameters (T_i from CXRS, T_e from the electron cyclotron emission (ECE) radiometer and LIDAR

or high resolution Thomson scattering (HRTS), n_e from interferometer and LIDAR or HRTS, Z_{eff} from CXRS and spectroscopic measurements and q from EFIT constrained with MSE). In order to confirm the consistency of the torque calculations, the time-dependent torque profile calculation between TRANSP and ASCOT has been benchmarked against each other in JET plasmas with NBI modulation both in [7, 8]. The agreement between the two different codes is very good and constitutes a powerful confirmation that we can rely on the torque calculations for our transport analysis.

The modulated NBI torque source is broad. Therefore, a simple determination of the momentum diffusivity and pinch directly from the spatial derivatives of the amplitude and phase of the modulated ω_ϕ is not viable. As a consequence, time-dependent transport modelling of ω_ϕ is required to extract the transport properties from the plasma dynamic response, assuming that torque sources are known with reasonable accuracy from numerical calculations. The transport analysis methodology is in this study to determine the momentum diffusivity and pinch is the same as that described in more detail in [7, 29]. It is based on predictive transport simulations of toroidal rotation using the 1.5D code JETTO [40] and the power and torque sources calculated by TRANSP or ASCOT. The transport equation for ω_ϕ is solved while q-profile, T_i, T_e and n_e are frozen to their experimental values. The boundary conditions for steady-state ω_ϕ, amplitudes $A(\omega_\phi)$ and phases $\varphi(\omega_\phi)$ of the modulated ω_ϕ are chosen to fit the experimental data at $\rho = 0.8$ as the edge momentum plasma transport is beyond the scope of interest in this study. The analysis technique is based on minimizing the error between the experimental and simulated amplitude, phase and steady-state profiles of the rotation where the transport model for the rotation includes a Prandtl number and a pinch term chosen in a way to best reproduce the experimental amplitude, phase and steady-state profiles. As a result, a Prandtl and a pinch profile covering radially the whole region from the centre up to $\rho = 0.8$ is obtained.

3. Experimental scans to study the parametric dependences of momentum transport

3.1. Collisionality scan of the momentum pinch and Prandtl numbers on JET

A 3-point collisionality scan to study momentum transport coefficients has been performed on JET. The standard method to carry out the dimensionless similarity experiment to scan the collisionality, presented in [41], has been exploited in this experiment. The main idea is to vary collisionality while keeping the other dimensionless quantities, such as ρ^*, β_N, q and T_i/T_e, as constant as possible. The collisionality is varied by changing the electron temperature using the NBI power at constant density; ρ^* and β_N are kept constant by changing the magnetic field B_t and finally q kept constant by a relevant correction in the plasma current I_p. The time traces of the most relevant quantities are shown in figure 1. Within the 3-point scan, collisionality changes over almost a factor of 4. The volume-averaged ρ^* and β_N are changing within the scan by about 10% and 20%, respectively. The NBI power modulation and the different power levels between the pulses, required

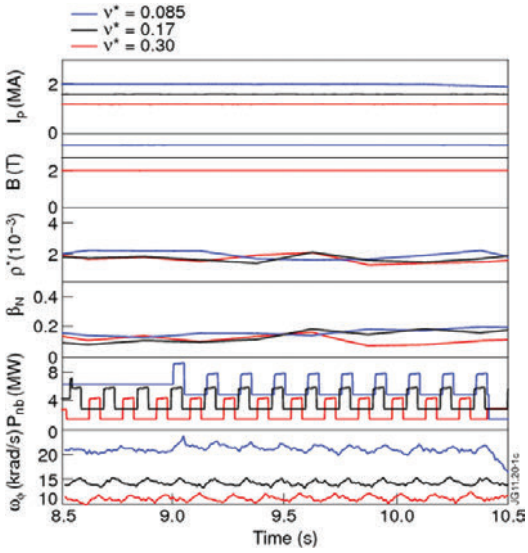

Figure 1. Time traces of plasma current I_p, magnetic field B at magnetic axis, ρ^*, β_N, NBI power P_{nb} and toroidal angular frequency ω_ϕ at $r/a = 0.5$ for 3 JET pulses no 79811 (blue), 79815 (black) and 79814 (red). The volume-averaged collisionality is also shown for each discharge.

to obtain the collisionality variation, are also shown. A clear modulated toroidal rotation ω_ϕ signal is also visible in figure 1.

The two key profiles to be kept constant within the scan in view of momentum transport studies are the density profile and the q-profile. These are both believed to play a major role in determining the magnitude of the momentum pinch in theory [34] and therefore, in order to obtain as clean as possible collisionality scan, any variations in these profiles are to be minimized. The density from the HRTS diagnostics and q-profiles from EFIT+MSE for these three shots are illustrated in figure 2, demonstrating nicely indeed that the scan succeeded well in keeping these profiles nearly identical. Both of the electron temperature profiles from ECE and the ion temperature profiles from CXRS are shown, indicating from where the difference in the collisionality between the shots originates. Also, the temperature ratio T_i/T_e is very well kept nearly constant and close to one.

The resulting Prandtl number and momentum pinch number profiles from the detailed transport analysis are shown in figure 3. It can be easily seen within the error bars from figure 3 that neither the Prandtl nor the momentum pinch number depends on collisionality. This scan was carried out in L-mode in plasmas because the collisionality scan, while simultaneously keeping R/L_n constant, is not viable to carry out in H-mode plasmas due to the density peaking dependence on collisionality [42, 43]. However, according to GS2 [44] linear gyro-kinetic simulations, these NBI heated L-mode plasmas are dominated by the ITG mode in a very similar way as those NBI heated JET plasmas in H-mode.

The magnitude of the momentum pinch numbers, ranging between 3 and 5 in the core region ($0.3 < \rho < 0.8$), in these L-mode plasmas is of the same order as found earlier

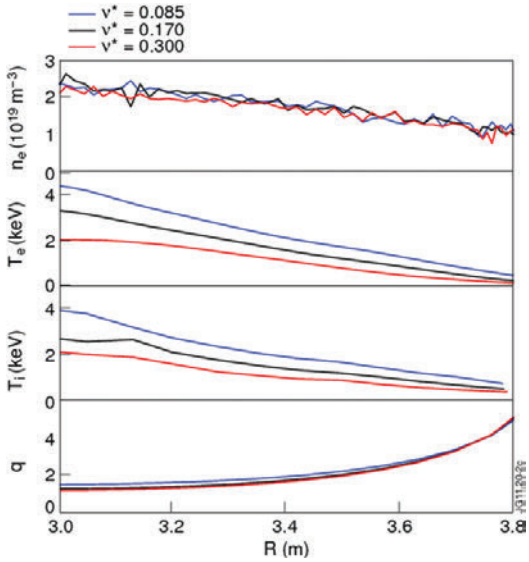

Figure 2. The radial profiles of density n_e, electron temperature T_e, ion temperature T_i and q-profile for the same shots as in figure 1 using the same colour code.

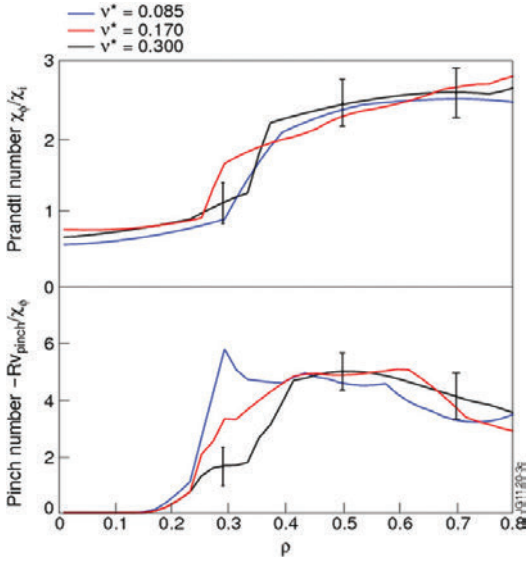

Figure 3. Prandtl number (upper frame) and pinch number (lower frame) profiles for the discharges forming the 3-point collisionality scan as a function of normalized toroidal flux co-ordinate ρ.

for most JET H-mode plasmas [7, 28, 29]. On the other hand, the Prandtl numbers tend to be some 20–40% higher in these L-mode plasmas than those of H-mode plasmas. This is discussed in more detail in section 4. There is a strong radial dependence for the Prandtl numbers, typically an increase of about a factor of 2 occurring when going from $r/a = 0.3$ to $r/a = 0.8$. It is to be noted that in the central region ($\rho < 0.2$),

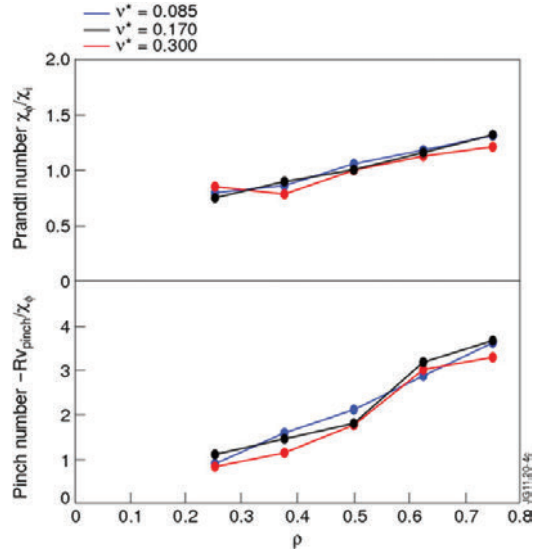

Figure 4. As in figure 3, but the data are from linear GS2 simulations using the actual input data from each shot. The GS2 runs have been performed at five radial locations for each shot.

the ITG turbulence is stable and thus, the pinch vanishes and the Prandtl number becomes close to unity for all JET shots, more or less independent of plasma parameters.

Calculation of the error bars for the Prandtl and pinch numbers using the analysis method described in detail in the references is not straightforward. In this paper, they have been estimated in such a way that first, a total error, resulting from the difference between the experimental amplitude, phase and steady-state and the simulated ones, using the choice of Prandtl and pinch number profiles that minimizes the error, has been calculated. The total error consists of the least square sum between the experimental and simulated amplitude, phase and steady-state profiles. Then, the actual error bars for P_r and $-Rv_{\mathrm{pinch}}/\chi_\phi$ have been estimated by allowing the Prandtl and pinch number profiles vary as far as the total summed error is still within 10% from the minimum total error (coming from the best choice of Prandtl and pinch numbers). The error bars shown in figure 3 and in the rest of the paper are based on this calculation method. By varying the Prandtl and pinch number profiles within the error bar range, typically the amplitude and steady-state vary by about 10–15% and the phase by about 15°, i.e. 5–10 ms. These numbers reflect well the error bars originating from the CXRS diagnostics itself (typically of the order of 5%) [45]. In addition, the experimental error in the amplitude of the modulated rotation is typically about 10%, calculated from the Fourier spectrum by taking any non-harmonic NBI modulation frequency. More details on the error bars and their calculation for the NBI modulation technique can be found in [7, 8].

The dependence of the momentum pinch and Prandtl number on collisionality was also studied in linear gyro-kinetic simulations using the GS2 code [44, 46, 47]. The GS2 runs have been performed using the actual data from each shot. The GS2 calculations were performed on a spectrum 6 modes

ranging from 0.15 to 0.8, with log spacing, and a spectral shape along [48] was used. This choice gives the usual peaking around $k_y\rho_i = 0.25$. The most important conclusion is that neither momentum pinch nor the Prandtl number depends on collisionality as illustrated clearly in figure 4. This result that the pinch and Prandtl numbers do not depend on collisionality is recently found to be valid more generally in momentum transport theory [36]. These simulation results are also fully consistent with the experimental results. The GS2 simulations also find the radially increasing Prandtl number profiles. However, while the simulated collisionality independence and radial dependences are in good agreement with the experimental ones, the simulated values of both $Rv_{\rm pinch}/\chi_\phi$ and P_r are lower than the experimental ones by a factor of 1.2–2. In particular, the Prandtl numbers from GS2 runs are lower by more than a factor of 1.5 than the experimental one throughout the radius, whereas the pinch numbers from GS2 runs actually reach values rather close to the experimental ones at $\rho > 0.6$. The reason for this quantitative difference in the magnitude of the P_r number and partly also in the pinch number between the GS2 runs and the experiments has not yet been identified. In earlier studies of a few JET H-mode pulses with NBI modulation, somewhat better agreement in the magnitude of the pinch and P_r numbers between the experiments and linear gyro-kinetic simulations with the GKW code [49] have been found [7].

3.2. Dependence of momentum pinch and Prandtl number on inverse density gradient length R/L_n

There is no simple way to perform a clean R/L_n scan in a tokamak without changing some other dimensionless parameter simultaneously. In particular, as already discussed in section 3.1, the strong coupling between the collisionality and R/L_n in H-mode plasmas makes the R/L_n scan without changing the collisionality virtually impossible to carry out. However, since no dependence of momentum transport coefficients on collisionality was found in the collisionality scan experiment as discussed in the previous section, it is possible to scan R/L_n by varying collisionality and assign the possible changes in momentum transport to be caused by R/L_n rather than collisionality.

The dependence of the Prandtl number on R/L_n is illustrated in figure 5. The single value of P_r attached to each shot is based on the average value of P_r between $0.4 < \rho < 0.8$. Also, R/L_n reflects the average value from the same radial range. The large range in R/L_n among the shots has been achieved mainly by varying collisionality, density and the amount of the NBI heating power. The magnetic field is 3.0 T and plasma current 1.5 MA for all the shots and the line-averaged density varied from 4.4×10^{19} m^{-2} to 8.4×10^{19} m^{-2}. It is evident in figure 5 that the Prandtl number does not depend on R/L_n as the scatter of the points is uniform. Typical error bars have been added for two of the shots. The variation in the error bar in the calculation of R/L_n is much smaller for the shots (such as the upper point with the error bar in figure 5) that have HRTS diagnostics measurements available than for the discharges with only Lidar Thomson scattering data (such as the lower point with the error bar in figure 5).

The red points in figure 5 are from linear GS2 simulations using the input data from 9 of the 12 experimental shots.

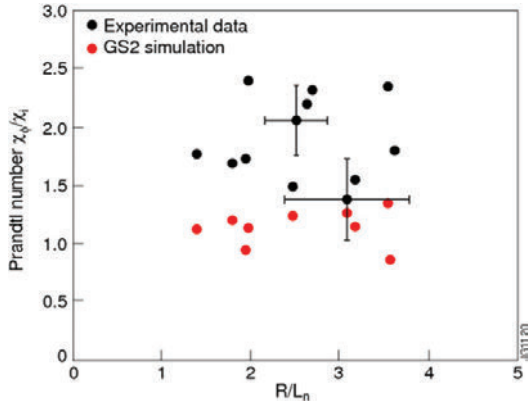

Figure 5. Experimental (black dots) and simulated (red dots) Prandtl numbers $P_r = \chi_\phi/\chi_i$, averaged over the range $0.4 < \rho < 0.8$, as a function of the inverse density gradient length R/L_n.

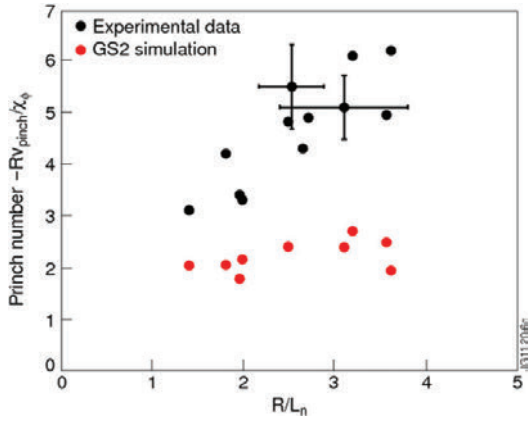

Figure 6. Experimental (black dots) and simulated (red dots) pinch numbers $-Rv_{\rm pinch}/\chi_\phi$, averaged over the range $0.4 < \rho < 0.8$, as a function of the inverse density gradient length R/L_n.

Consistent with experimental results, the Prandtl number is not found to depend on R/L_n by GS2. As already pointed out for the L-mode shots in section 3.1, the Prandtl numbers calculated by GS2 are lower than those of experiments. However, for the H-mode shots, the difference is typically smaller than a factor of 2 typically found for the L-mode shots.

While no dependence of the Prandtl number on R/L_n was found, a clear trend is found for the pinch number. This is illustrated in figure 6 where a strong dependence of the pinch number is plotted against R/L_n by the black points. Typical error bars originating from the analysis are shown for two cases, indicating that the dependence is clearly outside the error bars. For these shots, the NBI power and torque are significantly large (10–18 N m) and therefore, the intrinsic torque component is not believed to modify the conclusions. The present experimental evidence shows that intrinsic rotation is small on JET [13, 50, 51], around 10% or less of the NBI torque for the plasmas used in this density gradient length scan.

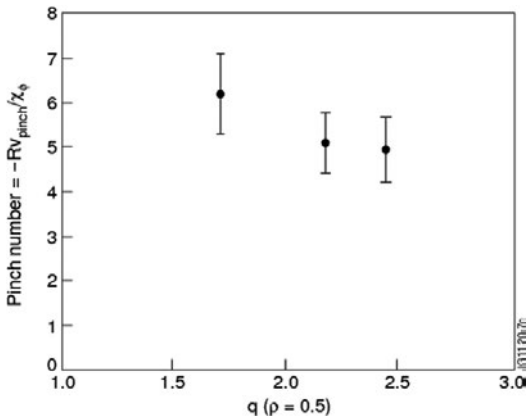

Figure 7. The experimental momentum pinch number $-Rv_{\rm pinch}/\chi_\phi$ with its error bars as a function of q value at mid-radius $\rho = 0.5$ from the 3-point q scan.

Similar to figure 5, the red points correspond to the GS2 simulations based on the experimental shots. GS2 runs also show an increase in $-Rv_{\rm pinch}/\chi_\phi$ with increasing $R/L_{\rm n}$ although the trend is much weaker than in the experimental data. The difference in the $R/L_{\rm n}$ dependence of the pinch number between the experiment and gyro-kinetic simulations is not fully understood. Preliminary simulations with GKW including the $E \times B$ shearing effect [52] have found that this mechanism produces a residual stress which is, however, too small to explain the difference between the predicted and measured pinch velocities. More extended investigations, also considering other residual stress mechanisms like the profile shearing effect [53, 54], are planned for future work.

Fitting a line through the experimental cloud of points, one obtains the following relation:

$$-Rv_{\rm pinch}/\chi_\phi \approx 1.2R/L_{\rm n} + 1.4. \quad (2)$$

The strong dependence of the momentum pinch on $R/L_{\rm n}$ has already been discussed earlier in theory [34]. What is also straightforward to conclude from the dependence above is that without knowing the inverse density gradient length, it will be challenging to estimate the momentum pinch number. When $R/L_{\rm n}$ ranges from 1 to 3 (typical values in present tokamak plasmas), $-Rv_{\rm pinch}/\chi_\phi$ ranges from 2.6 to 5, resulting in a large difference in rotation peaking. This strong dependence also has consequences to ITER predictions, discussed in more detail in section 5.

3.3. q-scan of the momentum pinch and Prandtl numbers

A 3-point q-scan was performed on JET. By keeping the magnetic field at $B = 3.0$ T, the variation in q was obtained firstly by increasing $I_{\rm p}$ from 1.5 MA to 2.5 MA and secondly by adding 3 MW of ICRF heating to delay current diffusion during and after the current ramp-up. The result of the scan is presented in figure 7 as a function of q at mid-radius. The variation of $R/L_{\rm n}$ within this 3-point q-scan in figure 7 was about 0.4, which should result in a change of 0.5 in the pinch number according to scaling (2). Therefore, the observed weak q dependence of the pinch number (larger than 1 unit in $-Rv_{\rm pinch}/\chi_\phi$ in figure 7) seems larger than the one induced by the difference in $R/L_{\rm n}$ between the high and low q shots. However, taking into account of the actual error bars as indicated in the plot, no solid conclusion can be drawn about the momentum pinch number dependence on q although the scan may suggest a possible weak dependence.

One should also note that while q is scanned here, the magnetic shear s is also varied, and the theory suggests in addition to the q dependence that $-Rv_{\rm pinch}/\chi_\phi$ depends also on s [34]. These two effects are challenging to separate from each other in the experiment. The Prandtl numbers for the same three shots are 1.55, 1.39 and 1.81, respectively, in the descending order of q as in figure 7. Therefore, one can conclude that no trend between the Prandtl number and q-profile was found within this scan.

4. Prandtl number in L-mode and H-mode plasmas

As already visible in figure 3, the Prandtl numbers are high in JET L-mode plasmas. They are typically above 2 outside mid-radius and can reach values up to 2.5. This is significantly larger than predicted by the early momentum transport fluid theory which gives Prandtl number to be 1 [55]. It is also somewhat larger than predicted by more recent gyro-kinetic simulations [56]. The gyro-kinetic simulations of the present JET L-mode discharges with GS2 also give Prandtl number profiles typically around unity, as shown in figure 4. There is clearly a quantitative disagreement between the experimental data and gyro-kinetic simulations although qualitatively, for example, the increasing P_r value as a function of the radius is well captured in simulations.

The relation of the Prandtl number between the L-mode and H-mode is studied more systematically here. The discharges chosen for the comparison have the same B, $I_{\rm p}$, $n_{\rm e}$ and NBI heating only. The two extreme cases with respect to P_r as far from each other as possible from this comparison are illustrated in figure 8 (left frame). For this extreme case, the Prandtl number in L-mode is more than 50% higher than in H-mode at all radii where the turbulent transport dominates over the neoclassical contribution. Looking into a larger set of JET NBI modulation shots, the trend that L-mode plasmas have higher Prandtl numbers than the H-mode ones is obvious, as shown in figure 8 (right frame). The Prandtl number of the highest L-mode shot and the one of the lowest H-mode shot are the ones plotted in the left frame. No similar trend for the pinch number is found between the L- and H-mode plasmas.

No obvious reason for the difference in P_r between L- and H-mode has been found so far. One candidate could be, as already discussed in section 3.1, that the L-mode shot could have more TEM driven transport and therefore, P_r, as compared with $\chi_{\rm i}$ would be higher. However, the linear GS2 simulations of these JET L-mode plasmas do find ITG as the dominant instability and by a large margin. This is not a surprise as these L-mode plasmas, heated with NBI only, have $R/L_{T_{\rm i}} \approx R/L_{T_{\rm e}}$ and $T_{\rm i} \approx T_{\rm e}$ and under these conditions, ITG always dominates. Another candidate could be the fact that if there are some non-NBI, intrinsic torque sources, their role could be larger in low NBI torque, low rotation L-mode plasmas. Residual stress has been proposed as a possible

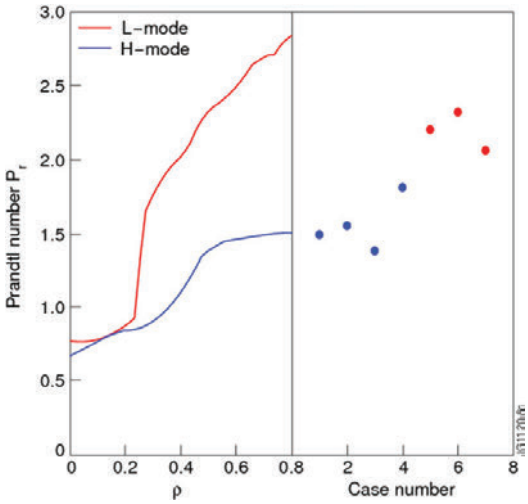

Figure 8. Comparison of the Prandtl number profiles in JET L-mode and H-mode plasmas (left frame) and a set of L-mode (red points) and H-mode (blue points) discharges (right frame) with the Prandtl number averaged over the radius $0.4 < \rho < 0.8$. Each point (case) in the right frame corresponds to a single analysed shot.

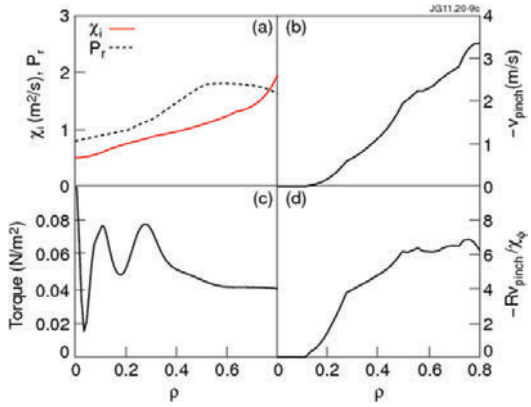

Figure 9. (*a*) The ion heat diffusivity and Prandtl number profile, (*b*) the pinch velocity, (*c*) the torque profile and (*d*) the pinch number profile used in the ITER simulations.

candidate to drive intrinsic rotation although its contribution in the core plasma may not be very large [57, 58]. However, if one assumes that its contribution would be the same in L-mode and H-mode plasmas, its relative importance and its possible effect on increasing spuriously the Prandtl number would be larger in low torque L-mode plasmas. This is because in this analysis method we have assumed NBI torque as the only torque source and its absolute value is typically of the order of 5 N m in L-mode plasmas while it is more like 15 N m in H-mode plasmas. Therefore, adding an extra intrinsic rotation or residual stress torque would modify the Prandtl and pinch numbers L-mode plasmas much more than in the H-mode ones.

5. Discussion of the consequences of these experimental results in view of rotation in ITER

Predicting the toroidal rotation profile in ITER is a challenging task. In recent years, predictive transport simulations of toroidal rotation using first-principles transport models have been performed to tackle this task [59, 60]. However, although serving as a good base for the starting point of the ITER rotation predictions, a number of simplified assumptions for momentum transport and torque sources have often been adopted in these modelling efforts. In particular, the assumptions that $\chi_\phi = \chi_i$, that there is no momentum pinch and that the NBI is the only torque source, may easily lead to qualitatively incorrect rotation predictions.

In this work, we take a different approach and use the Prandtl and pinch number profiles based on the scans of the parametric dependences on JET described in the previous sections. The main emphasis is to clarify the role of strong inward pinch under a variety of torque profiles and a variety of edge rotation values in shaping the toroidal rotation profile in ITER. However, it is to be noted already at this point that these simulations will not be the final ITER predictions for the toroidal rotation profile, but rather to demonstrate the key role of both the inward momentum pinch and the boundary conditions of the rotation in any realistic ITER rotation simulations. Important factors to make the final realistic ITER rotation prediction that we are still neglecting in this study are for example any non-NBI, intrinsic torque sources [10, 11], residual stress type of momentum flux terms [26, 58], braking effects for example due to 3D effects from RMP coils to suppress ELMs [17] and any consideration on what the edge rotation will be in ITER. To demonstrate the crucial role of the edge rotation boundary condition, an edge rotation scan is performed. Another example of a sink term neglected here is the TBM that may have a large influence on both the edge and core rotation in ITER, at least it is suggested by the DIII-D TBM experiments [19].

The rotation modelling philosophy in this study is that the temperature and density profiles are taken from the ITER reference scenario 2 (15 MA baseline scenario) specifications [61]. Only the equation for the toroidal rotation is solved in the JETTO transport code [40, 62] while the rest is taken from ITER reference scenario 2. GLF23 transport model [63] is used to calculate the ion heat diffusion coefficient χ_i from the given temperature and density profiles, shown in figure 9(*a*). The NBI torque profile, assuming the standard ITER specifications (ITER scenario 2 at density of 10^{20} m^{-3}), i.e. 33 MW of input power using 1 MeV negative ion beam source with a realistic ITER magnetic ripple background, has been calculated with the ASCOT code. The real NBI geometry with two injectors, one more on-axis and one more off-axis, have been used. This torque profile with two separate peaks originating from the two injectors is presented in figure 9(*c*).

For momentum transport, we take the Prandtl number and momentum pinch profiles from the high current (I_p = 2.5 MA, B = 3 T), low q, low collisionality (ν^* = 0.04) JET discharge no 73702. This can be considered to be the closest discharge, among those shots where the NBI modulation technique has been exploited, to ITER with respect to dimensionless parameters, but is by no means representing a perfect match with ITER numbers. Note that one of the

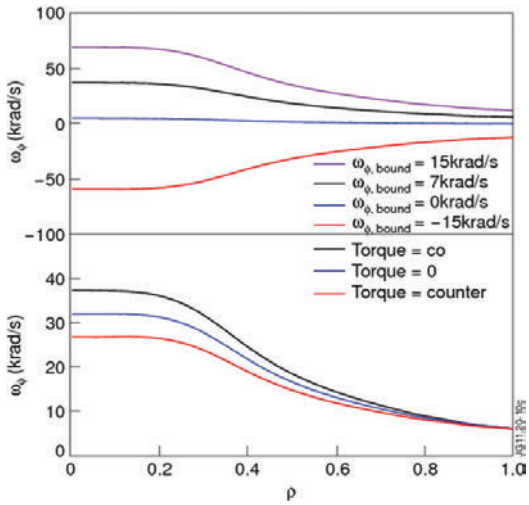

Figure 10. (*a*) The predictive toroidal rotation simulations for the ITER baseline scenario using various boundary conditions for the edge rotation. (*b*) As in (*a*) at $\omega_{\phi,\text{bound}} = 7\,\text{krad}\,\text{s}^{-1}$, but for co-, counter- and balanced (zero) NBI torque options.

dimensionless parameters most different in ITER than on JET is collisionality, however, based on the results presented in section 3.1, there is a good reason to believe that the momentum pinch and Prandtl numbers are independent of collisionality also in ITER. The Prandtl number profile used in the predictive simulations is shown in figure 9(*a*) and the pinch number profile in figure 9(*d*). This pinch number profile corresponds to the JET plasma with the inverse density gradient lengths of around $R/L_\text{n} \approx 3$–3.5 as illustrated in figure 6. For a comparison, the ITER standard scenario can be expected to have density peaking at mid-radius of $R/L_\text{n} = 2$–2.5 [43] as predicted consistently by both empirical scalings [64–66] as well as by theory-based transport simulations [67]. The actual pinch velocity in this ITER plasma can be calculated from the pinch number profile in figure 9(*d*), and is presented in figure 9(*b*).

Based on the modelling assumptions presented above, two scans of predictive simulations of toroidal rotation were performed. In the first scan, the boundary condition for the toroidal rotation was varied between $\omega_{\phi,\text{bound}} = -15\,\text{krad}\,\text{s}^{-1}$ and $15\,\text{krad}\,\text{s}^{-1}$. This boundary rotation of $15\,\text{krad}\,\text{s}^{-1}$ in ITER corresponds to normalized Mach Alfvén velocity $M_\text{A} = 0.0077$ on top of the H-mode pedestal $\rho = 0.95$ when using the profiles from the ITER reference scenario 2. This range of uncertainties in the edge rotation ($\omega_{\phi,\text{bound}} = -15$–$15\,\text{krad}\,\text{s}^{-1}$) can be easily caused for example by ripple [9], TBMs [19], ELMs [20], neutrals [21], interaction with SOL flows, for example seen between the upper and lower null configurations [22, 23] or other unknown edge torque sources.

The predicted toroidal rotation profile for each of the four boundary conditions is presented in figure 10(*a*). There are several interesting points worth commenting on. Firstly, the rotation with the zero-slip boundary condition (blue curve) is very close to zero throughout the whole radius. This suggests that the NBI torque deposited in the core region alone, at least with the present assumption for the Prandtl and pinch number profiles, is not able to create a significant toroidal rotation in ITER. On the other hand, when the boundary condition is increased to $\omega_{\phi,\text{bound}} = 7\,\text{krad}\,\text{s}^{-1}$ (black curve) or $\omega_{\phi,\text{bound}} = 15\,\text{krad}\,\text{s}^{-1}$ (magenta curve), significant toroidal rotation is predicted in the plasma core region, corresponding to $M_\text{A} = 0.03$ in the plasma centre with $\omega_{\phi,\text{bound}} = 15\,\text{krad}\,\text{s}^{-1}$. Concerning the NBI torque in ITER, it is, however, well possible that the NBI torque will affect the rotation value at the edge, either by a direct edge torque source or by the momentum flux created in the core. Studying the influence of the NBI torque, or any other edge torque source, on edge rotation is beyond the scope of this paper and thus left for future work. Therefore, no solid conclusion can yet be drawn on the overall role of the NBI torque in ITER. Another interesting point in figure 10 is that when the boundary condition is set to counter-rotation at the same magnitude of $\omega_{\phi,\text{bound}} = -15\,\text{krad}\,\text{s}^{-1}$ (red curve), the rotation becomes almost as much counter as it was co with $\omega_{\phi,\text{bound}} = 15\,\text{krad}\,\text{s}^{-1}$ boundary condition. This shows again that the core NBI torque has a minor role in directly determining the core toroidal rotation profile provided that the pinch number is large enough—note here the possibly important role of the NBI torque in determining the magnitude of the edge rotation which is not taken into account. The minor effect of the core NBI torque is illustrated further in figure 10(*b*), as the rotation profile does not change very much whether the NBI torque is co, balanced or counter (to note that counter-I_p or balanced NBI is not an option considered currently for ITER). Also note here that in these simulations, the boundary value of the rotation has been kept fixed independent of the direction of the NBI torque, and surely the direction of the NBI torque would have some impact on edge rotation. To sum up these ITER simulations, it is evident that the knowledge of the boundary condition, of course in addition to the knowledge of the magnitude of the pinch, is vital when the rotation profile is predicted to ITER plasmas. This is most obvious when the inward pinch is large. If the pinch number is small in ITER, for example as low as 2 or below around the mid-radius, then the core torque sources, such as NBI or RF driven or intrinsic ones, still play a major role in determining the shape of the core rotation profile.

6. Summary and conclusions

The NBI modulation technique has been exploited on JET to study parametric dependences of both the momentum pinch and the Prandtl number. This method is a powerful experimental tool to separate the diffusive and convective components of the momentum flux. The plasmas studied in all of the scans are dominated by ITG modes, therefore making the concept of Prandtl number, unambiguous. The torque calculations have been performed either with TRANSP or ASCOT and the results have been benchmarked against each other. In the experimental planning and transport analysis, great care has been taken in getting rid of MHD modes, such as sawtooth and ELMs, and equilibrium remapping due to plasma oscillations caused by the NBI modulation.

A dedicated collisionality scan was performed by keeping the other dimensionless quantities (β_N, ρ^*, q, T_e/T_i) constant. No change in the pinch number was observed when the

collisionality was varied by a factor of 4 within the scan. In addition, no dependence of the Prandtl number on collisionality was found. The pinch number was found to decrease weakly with increasing q, but this dependence is just within the error bars so that no solid conclusions can be drawn. The Prandtl number did not depend on q.

Within the R/L_n scan, a strong dependence for the pinch number on the inverse density gradient length was observed, $-Rv_{pinch}/\chi_\phi \approx 1.2R/L_n + 1.4$. This dependence is consistent with the JET rotation database study where a similar dependence of the pinch number on R/L_n is reported in [68]. Also, a statistical approach applied to the JET rotation database yields a similar trend [69]. Within the same R/L_n scan, the Prandtl number was not found to be sensitive to R/L_n in these JET experiments.

GS2 simulations are in good qualitative agreement with JET experimental results, i.e. the pinch and Prandtl numbers are found to be independent of collisionality and an increase in the pinch number with increasing R/L_n is reproduced. In some cases, such as the magnitude of the pinch number in the collisionality scan, a quantitative agreement is obtained. However, in many cases, such as the magnitude of the pinch number in the R/L_n scan or the Prandtl number in both the collisionality and R/L_n scans were significantly smaller in GS2 simulations than in the experiments. Concerning the pinch number in the R/L_n scan, one can note that the same simulations with the GKW code result consistently in about 10% higher pinch numbers than those calculated with GS2, making thus the discrepancy between the experiment than simulations somewhat smaller. Qualitatively, however, the trend of the pinch number with R/L_n remains similar between the two codes, i.e. still quantitatively smaller than found in the experiments.

In order to try to pin down possible reasons for the discrepancy between the experimentally found strong trend of the pinch number on R/L_n and the weaker one found in the GS2 simulations, one can first look for possible additional torque source terms or terms in the momentum flux. Based on the experimental intrinsic rotation data in JET, it is relatively easy to conclude that the intrinsic rotation is always quite small, less than $\pm 30\,\mathrm{km\,s^{-1}}$, and in fact, usually it is much smaller than that [13, 14]. This is to be compared with the NBI modulation H-mode discharges in these scans that have typically central rotation values of about 150–200 $\mathrm{km\,s^{-1}}$. As a consequence, the intrinsic rotation drive term seems to be an order of magnitude smaller at least in JET H-mode shots. However, it cannot be completely excluded experimentally that the residual stress term, for example due to a stronger H-mode pedestal in the higher power NBI modulation shots, could affect more the rotation than in the lower power intrinsic rotation studies (ICRH heated plasmas on JET cannot have the typical 12–14 MW of heating power that we have in NBI modulated shots). In order to test this effect, however, we have added an extra arbitrary torque term in addition to the pinch and Prandtl number in the transport analysis with JETTO for several JET shots. The result clearly shows that the fit between the experimental and JETTO simulated amplitude, phase and steady-state rotation is not or only marginally improving by adding such a term describing the residual stress. While the experimental evidence suggests that the effect of the residual stress term in the plasma core is relatively small, it may still have an important contribution to the rotation profile outside $r/a > 0.8$ which has not been analysed at all in this study where the boundary conditions are matched at $r/a = 0.8$.

In L-mode plasmas, there is certainly more room for the residual stress or other non-NBI torque terms to modify the deduced pinch and Prandtl numbers as the typical value of rotation is around $100\,\mathrm{km\,s^{-1}}$ with 5–6 MW of NBI power including the modulation. Therefore, if the residual stress drive stays the same as in H-mode, its impact can be significantly larger in L-mode plasmas. On the other hand, experimental evidence from DIII-D shows that it is just at the pedestal where the intrinsic torque drive is strongest [58]. In any case, adding co-torque in the pedestal and counter torque in the core, as found on DIII-D, would indeed decrease the deduced Prandtl number in the core (in the region of $0.3 < \rho < 0.8$) in the L-mode plasmas and thereby making it more similar to the ones in H-mode (see figure 8). However again, in the experimental JETTO transport analysis adding an extra torque term does not significantly improve the simulated amplitude, phase and steady-state with respect to the experimental ones, indicating that the residual stress may not be the key to resolve the discrepancy in the Prandtl number between the L- and H-mode. It is possible that the disagreement between the high experimental Prandtl numbers and the simulated GS2/GKW ones become closer to each other when taking into account the neoclassical $E \times B$ shear effect on the GS2/GKW Prandtl number calculation. Preliminary GKW simulations with the neoclassical $E \times B$ shear effect suggest at least an increase of Prandtl number for a few cases, but a more detailed analysis of the role of the residual stress term as a whole in JET H- and L-mode plasmas is left for future work.

Another possibility making the Prandtl number to be different in JET L- and H-mode plasmas is that L-mode plasmas are always in a different parameter regime as already discussed in section 3.1. In particular, the electron temperature and R/L_{T_e} tend to be higher with respect to the ion temperature and R/L_{T_i} in L-mode plasmas. This fact points towards a possible larger drive from TEM with respect to ITG and consequently, the concept of the Prandtl number being a ratio of momentum diffusivity to ion heat diffusivity could be less unambiguous. However, although a larger TEM drive is indeed found in GS2 simulations in JET L-mode versus H-mode pulses, the difference is so small that at least based on these simulations, this does not look like a possible explanation to resolve the Prandtl number discrepancy.

Based on the results from these parametric scans of the pinch and Prandtl numbers, one can conclude that the inward pinch will have a significant impact on rotation profile in ITER provided that some rotation sources are available at the edge of the plasma. The edge rotation has to be finite such that the inward pinch can be effective to make the plasma rotation peaked. With a finite edge rotation and a large enough inward pinch, core rotation sources may not in the end play such an important role in ITER than in present tokamaks. However, in predicting the rotation profile and magnitude for ITER, large uncertainties certainly remain, not just due to uncertainties in edge rotation and scaling of the pinch, but also due to uncertainties in core and edge sink terms. In particular, braking effects from resonant magnetic perturbation or other 3D effects

like TBMs may give large uncertainties in any extrapolation of the rotation profile for future tokamaks. Moreover, some MHD modes, such as Alfvén eigenmodes or NTMs, not discussed in this paper, can influence the rotation profile in ITER and furthermore, also fusion born fast alpha particles may have an effect on rotation to be taken into account [70]. In conclusion, while it seems plausible that the rotation profile will be peaked in ITER, the absolute magnitude of the toroidal rotation still remains challenging to predict with the present uncertainties in the edge rotation, in sources/sinks and in the exact extrapolation of the inward momentum pinch.

Acknowledgments

This work was supported by EURATOM and carried out within the framework of the European Fusion Development Agreement. The views and opinions expressed herein do not necessarily reflect those of the European Commission.

References

[1] Biglari H., Diamond P.H. and Terry P. 1990 *Phys. Fluids* B **2** 1
[2] Miller R.L. *et al* 1994 *Phys. Plasmas* **1** 2835
[3] Burrell K.H. 1997 *Phys. Plasmas* **4** 1499
[4] Mantica P. *et al* 2009 *Phys. Rev. Lett.* **102** 175002
[5] Garofalo A.M. *et al* 2001 *Nucl. Fusion* **41** 1171
[6] Buttery R.J. *et al* 2011 Cross-machine scaling of neoclassical tearing modes thresholds with rotation *Nucl. Fusion* submitted
[7] Mantica P. *et al* 2010 *Phys. Plasmas* **17** 092505
[8] Salmi A.T. *et al* 2011 *Plasma Phys. Control. Fusion* **53** 085005
[9] de Vries P.C. *et al* 2008 *Nucl. Fusion* **48** 035007
[10] Rice J.E. *et al* 2007 *Nucl. Fusion* **47** 1618
[11] deGrassie J.S. 2009 *Plasma Phys. Control. Fusion* **51** 124047
[12] McDermott R.M. *et al* 2011 *Plasma Phys. Control. Fusion* **53** 035007
[13] Eriksson L.-G. *et al* 2009 *Plasma Phys. Control. Fusion* **51** 044008
[14] Nave M.F.F. *et al* 2010 *Phys. Rev. Lett.* **105** 105005
[15] Lin Y. *et al* 2011 ICRF mode conversion flow drive in D(3He) plasmas on JET *Plasma Phys. Control. Fusion* submitted
[16] Lin Y. *et al* 2008 *Phys. Rev. Lett.* **101** 235002
[17] Sun Y. *et al* 2010 *Plasma Phys. Control. Fusion* **52** 105007
[18] Garofalo A.M. *et al* 2008 *Phys. Rev. Lett.* **101** 195005
[19] Schaffer M.J. *et al* 2011 *Nucl. Fusion* **51** 103028
[20] Versloot T. *et al* 2010 *Plasma Phys. Control. Fusion* **52** 045014
[21] Versloot T. *et al* 2011 *Plasma Phys. Control. Fusion* **53** 065017
[22] Rice J. *et al* 2005 *Nucl. Fusion* **45** 251
[23] LaBombard B. *et al* 2004 *Nucl. Fusion* **44** 1047
[24] Diamond P.H. *et al* 2008 *Phys. Plasmas* **15** 012303
[25] Dominguez R.R. *et al* 1993 *Phys. Fluids* B **5** 3876
[26] Peeters A.G. *et al* 2011 *Nucl. Fusion* **51** 094027
[27] Yoshida M. *et al* 2007 *Nucl. Fusion* **47** 856
[28] Tala T. *et al* 2007 *Plasma Phys. Control. Fusion* **49** B291
[29] Tala T. *et al* 2009 *Phys. Rev. Lett.* **102** 075001
[30] Tardini G. *et al* 2009 *Nucl. Fusion* **49** 085010
[31] Solomon W.M. *et al* 2009 *Nucl. Fusion* **49** 085005
[32] Solomon W.M. *et al* 2008 *Phys. Rev. Lett.* **101** 065004
[33] Kaye S.M. *et al* 2009 *Nucl. Fusion* **49** 045010
[34] Peeters A.G. *et al* 2007 *Phys. Rev. Lett.* **98** 265003
[35] Hahm T.S. *et al* 2007 *Phys. Plasmas* **14** 072302
[36] Peeters A.G. *et al* 2009 *Phys. Plasmas* **16** 062311
[37] Negus C.R. *et al* 2006 *Rev. Sci. Instrum.* **77** 10F102
[38] Goldston R.J. *et al* 1981 *Comput. Phys.* **43** 61
[39] Heikkinen J.A. *et al* 2001 *J. Comput. Phys.* **173** 527
[40] Genacchi G. *et al* 1988 JETTO: a free boundary plasma transport code (basic version) *Rapporto ENEA RT/TIB* 1988(5)
[41] Luce T.C. *et al* 2008 *Plasma Phys. and Control. Fusion* **50** 043001
[42] Weisen H. *et al* 2005 *Nucl. Fusion* **45** L1
[43] Angioni C. *et al* 2009 *Plasma Phys. Control. Fusion* **51** 124017
[44] Kotschenreuther M. *et al* 1995 *Comput. Phys. Commun.* **88** 128
[45] Giroud C. *et al* 2008 *Rev. Sci. Instrum.* **79** 525
[46] Dorland W. *et al* 2000 *Phys. Rev. Lett.* **85** 5579
[47] Kluy N. *et al* 2009 *Phys. Plasmas* **16** 122302
[48] Bourdelle C. *et al* 2007 *Phys. Plasmas* **14** 112501
[49] Peeters A.G. *et al* 2009 *Comput. Phys. Comm.* **180** 2650
[50] Nave M.F.F. *et al* 2010 *Phys. Rev. Lett.* **105** 015005
[51] Nave M.F.F. *et al* 2011 JET intrinsic rotation studies and predictions for ITER *Plasma Phys. Control. Fusion* submitted
[52] Casson F.J. *et al* 2009 *Phys. Plasmas* **16** 092303
[53] Waltz R.E. *et al* 2011 *Phys. Plasmas* **18** 042504
[54] Camenen Y. *et al* 2011 *Nucl. Fusion* **51** 073039
[55] Mattor N. *et al* 1988 *Phys. Fluids* **31** 1180
[56] Peeters A.G. *et al* 2005 *Phys. Plasmas* **12** 072515
[57] Diamond P.H. *et al* 2009 *Nucl. Fusion* **49** 045002
[58] Solomon W. *et al* 2011 *Nucl. Fusion* **51** 073010
[59] Budny R.V. *et al* 2008 *Nucl. Fusion* **48** 075005
[60] Halpern F.D. *et al* 2008 *Phys. Plasmas* **15** 062505
[61] Ikeda K. *et al* 2007 *Nucl. Fusion* **47** S18
[62] Tala T.J.J. *et al* 2000 *Nucl. Fusion* **40** 1635
[63] Waltz R.E., *et al* 1997 *Phys. Plasmas* **4** 2482
[64] Weisen H. *et al* 2006 *Plasma Phys. Control. Fusion* **48** A457
[65] Angioni C. *et al* 2007 *Nucl. Fusion* **47** 1326
[66] Greenwald M. *et al* 2007 *Nucl. Fusion* **47** L26
[67] Pereverzev G.V. *et al* 2005 *Nucl. Fusion* **45** 221
[68] de Vries P.C. *et al* 2010 *Plasma Phys. Control. Fusion* **52** 065004
[69] Weisen H. *et al* Probable identification of the Coriolis momentum pinch in JET *38th EPS Conf. (Strasbourg, France, 27 June–1 July 2011)* paper O4.120
[70] Honda M. *et al* 2011 *Nucl. Fusion* **51** 073018

VTT Publications
VTT Science 10

Title	**Fast ions and momentum transport in JET tokamak plasmas**
Author	Antti Salmi
Abstract	Fast ions are an inseparable part of fusion plasmas. They can be generated using electromagnetic waves or injected into plasmas as neutrals to heat the bulk plasma and to drive toroidal rotation and current. In future power plants fusion born fast ions deliver the main heating into the plasma. Understanding and controlling the fast ions is of crucial importance for the operation of a power plant. Furthermore, fast ions provide ways to probe the properties of the thermal plasma and get insight of its confinement properties. In this thesis, numerical code packages are used and developed to simulate JET experiments for a range of physics issues related to fast ions. Namely, the clamping fast ion distribution at high energies with RF heating, fast ion ripple torque generation and the toroidal momentum transport properties using NBI modulation technique are investigated. Through a comparison of numerical simulations and the JET experimental data it is shown that the finite Larmor radius effects in ion cyclotron resonance heating are important and that they can prevent fast ion tail formation beyond certain energy. The identified mechanism could be used for tailoring the fast ion distribution in future experiments. Secondly, ASCOT simulations of NBI ions in a ripple field showed that most of the reduction of the toroidal rotation that has been observed in the JET enhanced ripple experiments could be attributed to fast ion ripple torque. Finally, fast ion torque calculations together with momentum transport analysis have led to the conclusion that momentum transport in not purely diffusive but that a convective component, which increases monotonically in radius, exists in a wide range of JET plasmas. Using parameter scans, the convective transport has been shown to be insensitive to collisionality and q-profile but to increase strongly against density gradient.
ISBN, ISSN	ISBN 978-951-38-7467-4 (soft back edition) ISSN 2242-119X (soft back edition) ISBN 978-951-38-7468-1 (http://www.vtt.fi/publications/index.jsp) ISSN 2242-1203 (http://www.vtt.fi/publications/index.jsp)
Date	October 2012
Language	English, Finnish abstract
Pages	71 p. + app 75 p.
Keywords	JET, tokamak, fusion, energy, plasma, toroidal rotation, momentum transport, fast ions, neutral beam injection, NBI
Publisher	VTT Technical Research Centre of Finland P.O. Box 1000, FI-02044 VTT, Finland, Tel. 020 722 111

VTT Publications
VTT Science 10

Nimike	**Nopeat ionit ja liikemäärän kulkeutuminen JET-tokamakin plasmoissa**
Tekijä	Antti Salmi
Tiivistelmä	Nopeat ionit ovat erottamaton osa fuusioplasmoja. Niitä voidaan tuottaa sähkömagneettisten aaltojen avulla tai suihkuttamalla ne plasmaan energisinä neutraaleina. Nopeita ioneja käytetään kuumentamaan ja pyörittämään plasmaa, virranajossa sekä plasman ominaisuuksien ja koossapidon tutkimiseen. Tulevaisuuden voimalaitoksissa fuusioreaktioissa syntyvät nopeat ionit toimivat plasman pääasiallisena lämmönlähteenä. Nopeiden ionien ilmiöiden ymmärtäminen ja niiden hallinta ovat tärkeitä fuusiovoimaloiden operoinnin kannalta. Tässä väitöstyössä käytetään ja kehitetään numeerisia laskentaohjelmia selittämään nopeisiin ioneihin liittyviä koetuloksia Englannissa sijaitsevassa fuusiokoelaitoksessa (JET). Tutkimuksen kohteina ovat nopeiden ionien äkillinen väheneminen korkeilla energioilla radiotaajuuskuumennuksen yhteydessä, nopeiden ionien aiheuttama toroidaalinen vääntö magneettikentän ryppyisyyden vaikutuksesta ja liikemäärän kulkeutumisen ominaisuudet moduloituja neutraalisuihkuja käyttäen. Työssä todennettiin simuloinneilla, että ionien äärellinen pyörimissäde selittää kokeellisesti havaitun nopeiden ionien pienen lukumäärän korkeilla energioilla käytettäessä radiotaajuuskuumennusta. JET:n magneettikentän rypytyskokeissa havaitut plasman pyörimisen muutokset voitiin hiukkassimulointien avulla päätellä johtuvan pääasiassa nopeiden ionien synnyttämän väännön takia. Lopulta analyysit liikemäärän kulkeutumisesta useissa erilaisissa plasmoissa osoittivat, että liikemäärän kulkeutuminen ei ole pelkästään diffuusia ja että merkittäväksi osoittautunut koossapitoa parantava ajautumisnopeus kasvaa plasman ulkoreunaa lähestyttäessä. Plasman tiheysgradientin kasvattamisen havaittiin nopeasti kasvattavan ajautumisnopeutta, kun taas törmäyksellisyyden tai q-profiilin muutosten vaikutukset olivat pieniä. Työn tuloksia voidaan hyödyntää ITERin ja tulevien laitosten suunnittelussa ja plasman pyörimisen ennustuksissa.
ISBN, ISSN	ISBN 978-951-38-7467-4 (nid.) ISSN 2242-119X (nid.) ISBN 978-951-38-7468-1 (http://www.vtt.fi/publications/index.jsp) ISSN 2242-1203 (http://www.vtt.fi/publications/index.jsp)
Julkaisuaika	Lokakuu 2012
Kieli	Englanti, suomenkielinen tiivistelmä
Sivumäärä	71 s. + liit. 75 s.
Avainsanat	JET, tokamak, fusion, energy, plasma, toroidal rotation, momentum transport, fast ions, neutral beam injection, NBI
Julkaisija	VTT Technical Research Centre of Finland PL 1000, FI-02044 VTT, Finland, Puh. 020 722 111

Fast ions and momentum transport in JET tokamak plasmas

Energy production and consumption are strongly linked with critical environmental issues such as global warming. Today more than 80 % of our primary energy is obtained by burning fossil fuels. It is widely recognised that cleaner and more sustainable forms of energy are needed. Nuclear fusion between heavy hydrogen isotopes has the potential to provide an abundant and environmentally friendly form of energy for the future.

Currently, the most advanced concept for a fusion power plant is a tokamak. Inside its torus shaped chamber, the fuel, in a form of plasma, must be confined and heated to over 100 million degrees and kept clear from the surrounding walls to initiate the fusion reactions. The economic viability of fusion power is largely determined by the degree of plasma confinement that can be achieved. Experiments have shown that by spinning the plasma in toroidal direction its confinement is improved and that certain instabilities can be mitigated thus improving the fusion performance.

Fast ions are responsible for most of the plasma rotation in present day tokamaks. This research is focused on fast ions as a rotation source and as a tool for studying the toroidal rotation and momentum transport properties of the JET tokamak plasmas. Numerical code packages are developed and validated against the experimental data paving the way for predictive modelling capabilities.

ISBN 978-951-38-7467-4 (soft back ed.)
ISBN 978-951-38-7468-1 (URL: http://www.vtt.fi/publications/index.jsp)
ISSN 2242-119X (soft back ed.)
ISSN 2242-1203 (URL: http://www.vtt.fi/publications/index.jsp)